Experimental Response of Gas Hybrid Bearings for High Speed Oil-Free Turbomachinery

by

Deborah A. Wilde

May 2002

TRC-B&C-2-02, May 2002

EXECUTIVE SUMMARY

Gas film bearings offer unique advantages enabling successful deployment of high-speed micro-turbomachinery. Current applications encompass micro power generators, air cycle machines and turbo expanders. Mechanically complex gas foil bearings are in use; however, their excessive cost and lack of calibrated predictive tools deter their application to mass-produced oil-free turbochargers, for example. The present investigation advances the analysis and experimental validation of simple gas bearing configurations with static and dynamic force characteristics desirable in high-speed turbomachinery. These characteristics are adequate load support, good stiffness and damping coefficients, low friction and wear during rotor startup and shutdown, and most importantly, enhanced rotordynamic stability at the operating speed.

Comprehensive experiments and analysis are conducted on a small rotor supported on three lobed hybrid (hydrostatic/hydrodynamic) rigid gas bearings. The rigid bearings comprise preloaded 120° lobes with minute feed holes for external pressurization, bleed off from a turbocharger compressor outlet, for example. The bearing nominal clearance and dimensionless preload are 66 microns and 0.33, respectively. The test rotor, weighing 827 grams, integrates a DC motor and can achieve speeds as large as 100,000 rpm. Without rotor spinning, external pressurization lifts the test rotor at 1.36 bar (5 psig). For various imbalance conditions, coast down tests from 60,000 rpm characterize the rotor response on its bearings. As the supply pressure rises, the rotor response shows an increase in critical speed and a noticeable reduction in damping ratio. Threshold speeds of instability also increase with increasing supply pressures, and whirl frequency ratios range from nearly 50% of rotor speed for a purely hydrodynamic condition to 25 % for a pressure supply five times ambient conditions. Bearing transmitted loads closely follow the rotor imbalance responses with large peak values while traversing the critical speeds.

A linear rotordynamics model accounts for the rotor and gas hybrid bearings. The structural rotor model reproduces measured free-free natural frequencies and mode shapes. A FE laminar flow model for hybrid gas bearing analysis predicts frequency

dependent stiffness and damping force coefficients at the operating speeds and levels of feed pressure tested. The eigenvalue analysis forwards natural frequencies in agreement with the measurements, and null damping ratios evidence the threshold speeds of rotordynamic instability. Estimated whirl frequency ratios are typically 50% of rotor speed, thus predicting sub synchronous instabilities at lower rotor speeds than found experimentally when increasing the magnitude of feed pressurization.

Similar imbalance response measurements were conducted with the test rotor supported on hybrid pressure dam gas bearings and on HyPad® tilting pad gas bearings. Severe pneumatic hammer instability initially exhibited by the pressure dam bearings was eliminated by feed orifice repositioning into the film lands. The rotor supported on the pressure dam bearings shows adequate damping and a much lower threshold speed of instability than the rotor supported on the three-lobe bearings. The HyPad® bearings show good damping coefficients without rotordynamic instability for rotor speeds as large as 90,000 rpm. At high speeds, feed pressure can be removed to the HyPad® bearings since the rotor rides safely on the hydrodynamic gas film.

Experiments to determine break away friction and rotor lift off speed are conducted on a coated and uncoated rotor starting from rest. The coating is a commercial solid lubricant applied at room temperature. The transient response measurements vividly reveal rotor lift off and reduced friction with the coated rotor.

Principal Investigator: Luis San Andrés.

TABLE OF CONTENTS

NOMENCLATURE

a	Orifice restrictor diameter [m]
A	Effective orifice area [m^2]. (πa^2) or ($\pi d C$)
C	Nominal pad clearance [m]
$C_{\alpha\beta}$	Damping coefficients; $\alpha, \beta = X, Y$ [N/m]
C_L	Clearance at land [m]
C_{max}	Maximum bearing clearance [m]
C_{min}	Minimum bearing clearance [m]
C_r	Radial bearing clearance [m]
d	Orifice discharge diameter [m]
D	Journal (rotor) diameter [m]
$disp_{max}$	Maximum displacement amplitude at N_n [mm]
e	Journal eccentricity vector [m]. $(e_X^2 + e_Y^2)^{0.5}$
e_X, e_Y	Journal eccentricity components [m]
F_X, F_Y	Fluid film forces [N]
H_D	Clearance at pressure dam [m]
K	Clearance ratio. H_D/C_L
$K_{\alpha\beta}$	Stiffness coefficients; $\alpha, \beta = X, Y$ [N/m]
K_{eq}, C_{eq}	$K_{xx} + \omega C_{xy}$; $C_{xx} - K_{xy}/\omega$. Equivalent system stiffness
L	Bearing axial length [m]
L_D	Pressure dam axial length [m]
m	Calibrated imbalance mass [kg]
M	Rotor mass per bearing [kg]
n	Spectral line sample number
N_N	Natural frequency [rpm]
N_1, N_2	Speeds corresponding to 0.707*displacement at N_N [rpm]
O_b, O_j	Location of axial centerline
P	Gas absolute pressure [Pa]. $p = P / P_a$. (P_{ratio}); $\overline{P} = P / P_s$
r	Lobe preload [m]
$\bar{r}$	Nondimensional preload. r/C
R	Journal radius, [m]. $(D/2)$
R'	Radial location of imbalance mass [m]
u	Imbalance displacement [m]
$x = R \cdot \theta$, y	Coordinate system on plane of bearing
X, Y	Inertial coordinate system
θ	Circumferential coordinate [rad]
Λ	Bearing speed (compressibility) number. $\frac{6\mu\Omega}{P_a}\left(\frac{R}{C}\right)^2$
μ	Gas viscosity [Pa · s]
ρ	Gas density [kg/m^3]

ϕ	Journal attitude angle [rad]
Ω, ω	Journal rotational speed and excitation frequency [rad/s].
ξ	Damping ratio

Subscripts

a, s	Ambient and supply conditions
b, j	Bearing and journal (rotor)
p, D	Pivot offset, pressure dam
OR	Orifice

LIST OF TABLES

LIST OF FIGURES

INTRODUCTION

Environmental concerns and extreme operating conditions drive the needs for oil-free bearing support elements in small to moderate size turbomachinery (< 1 MW). While oil-lubricated fluid film bearings provide adequate stiffness and damping characteristics, these support systems are limited by speed and temperature, and require considerable ancillary pumping, sealing, and plumbing. The use of process gas lubricated bearings allows for less complex, lighter weight systems with lower emissions and improved efficiencies. Gas bearings for high-performance turbomachinery should be simple and reliable, load tolerant, and allow for operation at high rotor speeds with good dynamic force properties.

Gas bearings are in use in industrial applications such as auxiliary power units, air-cycle units in airplanes, short-life systems i.e. cruise missiles and space applications, microturbines and small turbocompressors, and dental hand piece drills. Yet, there are several areas of concern which must be addressed and well understood by industry before gas-lubricated bearings become an acceptable and preferred alternative to oil-lubricated bearings [1-3]. The low viscosity of the gas film demands minute clearances to generate adequate load capacity. Damping, necessary to traverse critical speeds and to attenuate sudden imbalance and thrust loads, becomes crucial. Gas bearings also experience excessive drag and damaging wear at start-up and shut down, are known to exhibit rotordynamic instability in rigid surface configurations, and even induce pneumatic hammer for externally pressurized configurations.

Multiple rigid lobes or pad configurations, modifying a plain cylindrical bearing, can improve the dynamic performance by creating a preload (the dimensional difference in clearance between the lobe and the bearing), thereby providing direct stiffness at the bearing centered operating condition. For higher speeds and light loads, multiple-lobe bearings are known to offer a slightly more stable behavior than plain cylindrical journal bearings [4, 5]. The reduction of load capacity and the issue of transient rubbing can be overcome by introducing external (hydrostatic) pressurization

to the lubricating film by way of orifice feed holes [6] and by adequate solid-lubricant films to reduce friction and wear.

The background research in gas-lubricated bearings flourished in the 1960's. Recently, advances concerning gas-lubricated hybrid (hydrostatic / hydrodynamic) configurations at high speeds (upwards of 100,000 rpm) have mostly been on the micro scale, with application to MicroElectroMechanical systems (MEMs) and/or microturbomachines. Such systems have millimeter scale geometries and require operating speeds greater than a million rpm. Piekos [7, 8] presents a simulation model and design charts for the development of silicon wafer gas-lubricated journal bearings for microfabricated MEMs. Fréchette reports the successful implementation of gas-lubricated journal bearings supporting an electrostatic induction micromotor to speeds of 15,000 rpm[1] [9].

Theoretical predictions and experimental verification are required to more thoroughly understand the static and dynamic performance and the limitations of gas hybrid bearings for current and envisioned applications in oil-free turbomachinery. The objectives of the research are to demonstrate their rotordynamic performance, reliability and durability in an experimental facility, to advance a theoretical analysis for the dynamic forced performance of hybrid gas film bearings, and to provide feedback for further technological developments.

---

[1] The difficulties with obtaining the appropriate terminal voltage is the speed limiting factor in this application, not the performance of the gas-lubricated journal bearings.

Literature Review

Gas-lubricated bearings, as opposed to oil-lubricated bearings, clearly have many advantages, as well as several disadvantages, for application to high-speed turbomachinery. Using process gas as the lubricant offers more cleanliness and the elimination of process contamination by buffer lubricants. Under extreme temperature and speed conditions, gases offer more stability without lubricant vaporization, cavitation, solidification, or decomposition. Gas-lubricated bearings also exhibit lower friction and power usage. In addition, gas bearings do not require the costly, weighty, and complex sealing and lubricant circulation systems required for oil-lubricated systems.

The main disadvantages of gas-lubricated bearings are the lack of damping and low load capacity due to the low viscosity of the gas film. This restriction demands ever smaller clearances than required by oil films, increasing the need to closely monitor tight manufacturing tolerances and surface finishes, thermal and elastic distortions, mounting, and alignments. In addition, gas bearing force coefficients describing the dynamic forced performance are highly dependent on frequency [10], adding an additional degree of complexity when attempting to quantify bearing performance.

Fuller [5] reviews the major advances in gas bearing design and modeling reported through the 1960's. Elrod and Malanoski [11] studied the plain cylindrical bearing with a continuous gas film, providing computer-generated solutions. Plain cylindrical bearings offer the best load capacity but compromise damping characteristics and often experience dangerous self-excited dynamic instability. Yet, these bearings offer the most affordable design when considering manufacturability and cost. Efficient numerical solutions of the Reynolds equation (predicting the pressure profile within the continuous film) and analyses addressing the major issue of rotor-bearing stability are readily available [12-20].

Modifications of the plain cylindrical bearing, such as the addition of lobes and Rayleigh steps (axial grooves), may help to reduce instability by interrupting the film

continuity and pressure profile thereby preventing the propagation of pressure disturbances. Multiple lobes improve the bearing dynamic performance, offering more stable behavior, by providing direct stiffness derived from a geometric preload; that is, the lobes create a converging and diverging film clearance. By examining the effective stiffness, effective damping, and critical mass as functions of the compressibility number, Lund [21] determines that a gas-lubricated three-lobe bearing is not inherently unstable, as is the case of a plain cylindrical journal bearing. Unfortunately, the increase in stability is offset by lower load capacity.

Archibald [22], with discussion by Malanoski [23], and Hamrock [24], provide the analysis of the step bearing configuration for optimized load capacity, and report improved damping and stability due to the contained volume inherent to the design modification. In the cases of low numbers of axial grooves and of a bearing operating at high compressibility numbers, the axial groove bearing has been shown to supply increased load capacity over the plain cylindrical bearing [24]. Castelli [25] and Hamrock [24] give graphical results of the load and attitude angle for axial groove bearings. Constantinescu [26] includes inertial effects by deriving the relationship between the pressure change at the Rayleigh step and the ratio of film clearances before and after the step. For example, the reverse flow effect for the flow entering the land region can cause the flow to decelerate at the converging step, producing a pressure rise instead of drop at the step. This limiting condition occurs when the film ratio is large, particularly when the land clearance is small. Another problem to be considered is the capacity to provide sufficient lubricant in cases of large Reynolds numbers and/or large film thicknesses. Pressure dams with additional circumferential lands help to reduce lubricant side-leakage and have been used extensively with incompressible lubricants to suppress oil whirl [27]. It should also be recognized that the step bearing is rather difficult to manufacture and requires the bearing to operate in the eccentric position in order to support an external load.

While the lobed and Rayleigh step bearings saw an improvement in stability and in some instances load capacity, tilting pad bearings (or pivot-pad bearings) have

proven to be a viable bearing option due to the absence of self-excited whirl, self-aligning capabilities, and the ability to compensate for thermal growth. Each pad pivots and promotes the formation of the load carrying convergent film wedge. However, due to the geometry of this type of bearing, the degrees of freedom in the form of pad motion increase from that of regular journal bearings, and the theoretical solution becomes rather complicated. Gunter [28] forwards numerical and graphical solutions for the load-carrying capacity of a tilting pad bearing and the results compare well with limited experimental results. Castelli [29] extends these solutions to include steady-state characteristics giving load carrying capacity and pad film thickness as functions of pivot location. Gunter [30] includes additional graphical solutions for pad friction and optimum clearance. The dynamic stiffness and damping coefficients and stability characteristics of the gas-lubricated tilting pad bearing are extended by Lund [21].

Several of the issues of concern with gas bearings, such as excessive drag during the transient rubbing at start-up and shut down, can be resolved by increasing the load capacity, especially at low speeds. This is done by hydrostatically supplementing the hydrodynamically self-generated load capacity with pressurized gas fed directly to the bearing clearance, thereby creating a hybrid bearing[2]. Utilizing hybrid bearings reduces wear from solid contact at startup and shutdown, can substantially raise the threshold of instability, and permits larger spans of stable response over the rotor/bearing system operating range. Shapiro [31] indicates that a substantial increase in load capacity is achieved with a small expenditure of supply gas with the proper hybrid design. Gross [1] categorizes gas bearings by geometry and by type of compensation, i.e. the method by which resistance to lubricant flow is introduced between the pressurized source and the lubricating film. The types of compensation are divided into inherently compensated (compensation at the entrance

---

[2] Hybrid bearings are often termed orifice compensated due to the feeding holes from the external pressurization to the film lands. Note that in hydrostatic gas bearings, deep recesses or pockets are not recommended to avoid pneumatic hammer instability.

of the flow to the film clearance), orifice, capillary, and plug-type. Several other practical configurations include hybrid pressure dam bearings and porous bearings.

Lund [32-33] advances the first approximate analysis and results for hybrid (hydrostatic / hydrodynamic) gas bearings. Zhang [34] optimizes the pocket geometry present in a hybrid journal bearing with annular and shallow pocket restriction to attain the largest critical mass. Jing [35] finds that surface-restriction through multiple axial saw tooth grooves offers more stable performance at the nearly centered journal position. Theoretical predictions and experimental results for the static and dynamic characteristics are included. Greenhill [36] reports experimental results showing the stable performance of prototype hybrid tilting pad gas bearings for speeds to 3 million DN. While offering more stable performance, these bearing configurations are considerably more complex, making low cost mass production difficult.

Fixed geometry gas bearings are prone to show a (self-excited) hydrodynamic instability at sufficiently large operating speeds. Hydrostatic (external) pressurization, on the other hand, brings forward a characteristic pneumatic hammer that more severely limits the safe range of rotor speeds, feed pressures and excitation frequencies where gas bearings remain stable [37, 33]. Pneumatic hammer, characterized by a sudden loss of damping even at low frequency excitations, is controlled by the flow-versus-pressure time lag in the gas supply restrictors and often has a whirl frequency ratio that diverges from 0.5 (the characteristic hydrodynamic whirl instability frequency ratio). Sun [38] provides a linear theory as a combination of whirl and pneumatic instabilities for porous externally pressurized journal bearings, and finds them to be considerably more stable at the nearly centered position than plain journal bearings. So far, literature has not presented any general rules or patterns characterizing the onset of pneumatic hammer instability, shown to occur even when the rotor is not spinning [11]. Stowell [39] conducts an experimental study of the effect of orifice compensation on pneumatic hammer in an externally pressurized thrust bearing. For different orifice diameters, only one diameter showed significant pneumatic instability [12]. Inherent type orifices, i.e. a feed condition with no trapped

gas volumes, alleviate the problem of pneumatic instability at the expense of decreasing the bearing load capacity. In an externally pressurized porous bearing, the occurrence of pneumatic instability is improved by increasing the L/D ratio and by decreasing the supply pressure [13]. Even considering the high susceptibility for pneumatic instability, Mehta reports very stable performance of orthogonally displaced pressure dam bearings with two pads, having large regions of infinite stability and very high minimum threshold speeds [40]. Along with stabilizing advantages, Hamrock confirms that for relatively high compressibility numbers, the load carrying capacity of Raleigh step bearings is higher than for plain cylindrical bearings [15].

To the author's knowledge, little information has been published about the performance of high-speed (up to 100,000 rpm) gas-lubricated hybrid bearings. The objective of the present work here is to experimentally establish the stability and dynamic forced performance of a hybrid three-lobe journal bearing design. A qualitative assessment of the system coast down response to calibrated imbalance masses and at various supply pressures is conducted by addressing critical speeds and damping ratios. In addition, the 'lift-off' characteristics, the identification of the threshold speeds of instability, and whirl frequency ratios demonstrate the stable performance of the bearing.

EXPERIMENTAL FACILITY

All experiments were conducted on an existing test rig, shown in Fig. 1, located in the Turbomachinery Laboratory at Texas A&M University. The test facility was recently built specifically for this project with funding from the Turbomachinery Laboratory and the Texas Energy Resources Program.

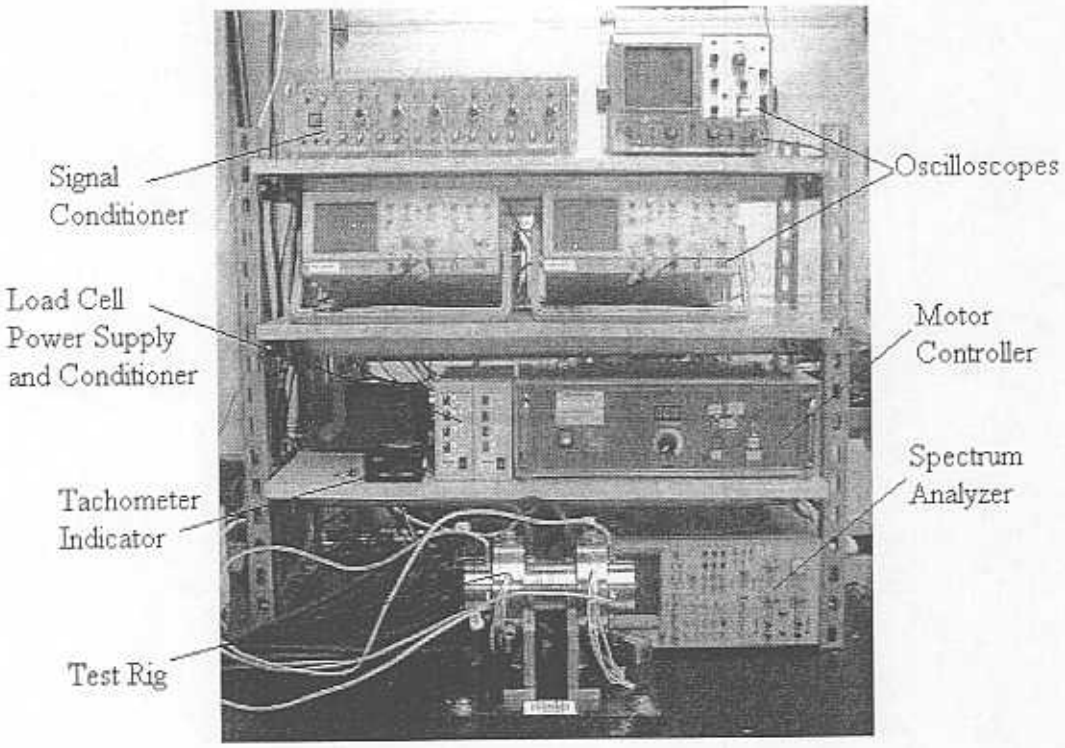

Fig. 1 Gas bearing test rig and instrumentation

Test Rig

An integral motor (capable of a maximum speed of 99,000 rpm) drives a rotor (Fig. 2) supported on two test bearings. The rotor has a mass of 827 grams (1.82 lb) and consists of a solid steel shaft, 15 mm diameter and 190 mm long, onto which an integral brushless DC motor and two solid steel sleeves (28.48 mm [1.12 inch] outer diameter) are press-fit. Eight 1 mm diameter holes equally spaced at the rotor ends allow for the placement of imbalance masses to force the rotor/bearing dynamic imbalance response.

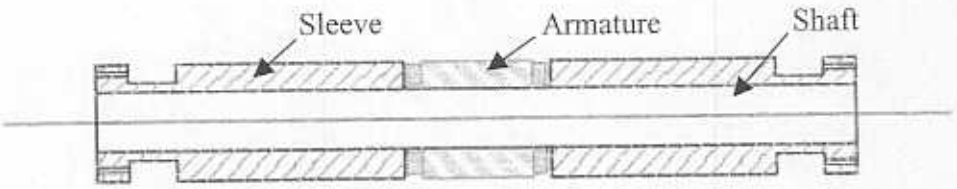

Fig. 2 Schematic of rotor assembly displaying a solid shaft, integral motor, and sleeves

The motor controller offers 0.9 kW continuous power and is protected by 1.0 amp fuses. A K-type thermocouple attached to the integral motor inside the test chamber monitors the temperature of the motor armature. A rapid rise in motor temperature is a good indicator of sustained solid contact between the rotor and the test bearings.

Fig. 3 shows the design of the stainless steel test chamber allowing for various types of test bearings to be installed. Each bearing housing has two O-rings that effectively seal the bearing section and allow that section to be pressurized. The test chamber therefore has six sections with supply air inlet and outlet fittings in each section. The supply air inlet and outlet are controlled by a set of on/off valves, needle valves, and pressure gages that are connected to a main pressure gage, regulator, dryer/filter, and then to the shop air line (8.6 bar [125 psi]). Mass flow meters, with flow ranges to 2.16E-3 kg/s (100 stL/min) for the left bearing plenum, 1.08E-3 kg/s (50 stL/min) for the right bearing plenum, and accuracy of 3.23E-5 kg/s (1.5 stL/min) and 1.62E-5 kg/s (0.75 stL/min), respectively, are connected inline to each test bearing plenum.

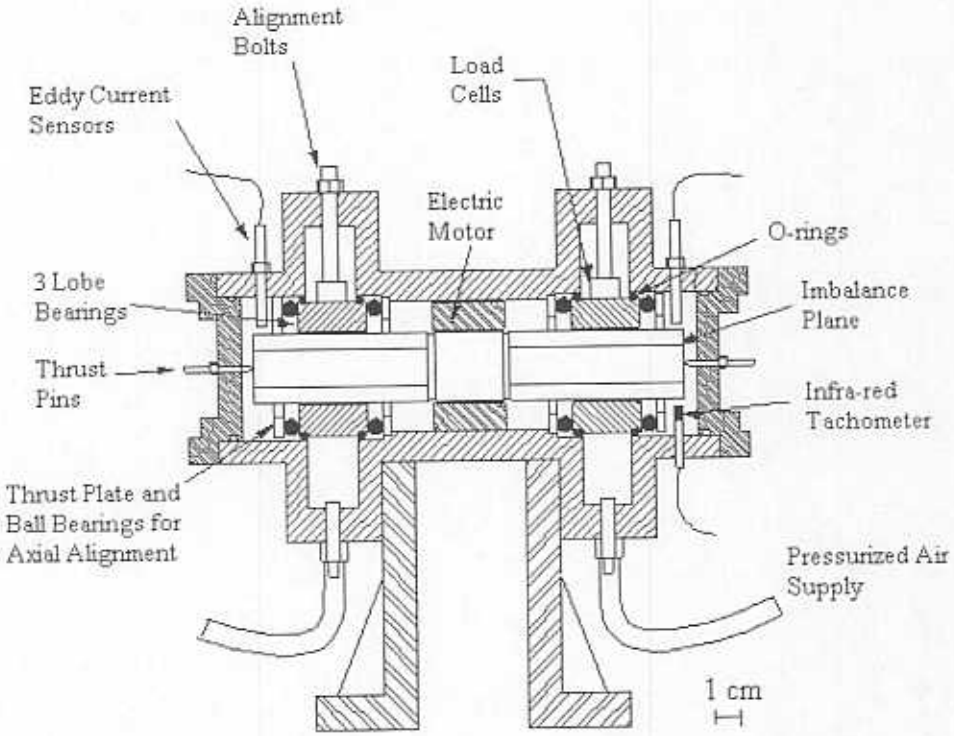

Fig. 3 Cross section view of test chamber showing rotor supported on three-lobe test bearings

Fig. 4 shows the end view of the test rig displaying two orthogonal positioned highly sensitive, eddy-current (3300 REBAM) sensors that measure the displacement of the shaft at each end[3]. The displacement sensors have a sensitivity of 39.37 mV/μm (1V/mil) with a linear range of 400 μm. The sensor recorded voltages are conditioned to remove the large DC bias offset before connection to two separate oscilloscopes and/or the LabView data acquisition system (DAQ). Each oscilloscope displays the shaft orbit at the end monitored. Unconditioned signals from the eddy current sensors are connected to an ADRE data acquisition system.

---

[3] Experimental results refer to the left (L) and right (R) bearings with respect to the view in Fig. 4, having vertical (V) and horizontal (H) sensors at each bearing, i.e. LH refers to the rotor response recorded with the left horizontal displacement sensor.

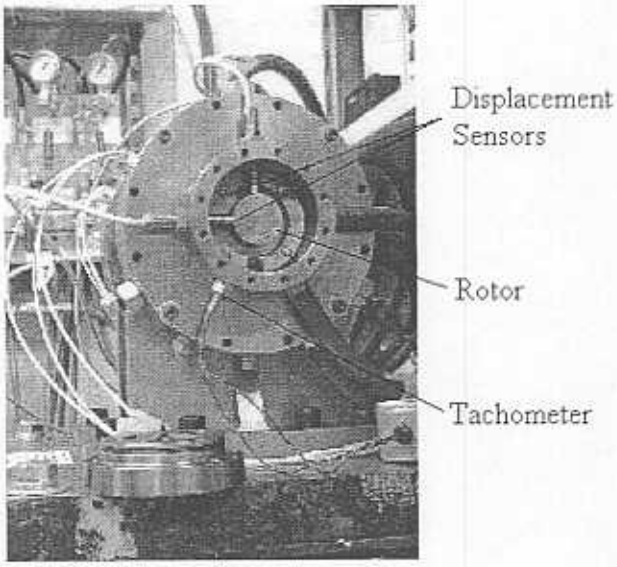

Fig. 4 Test rotor supported on three-lobe test bearings showing eddy current sensors and infrared tachometer

Force piezoelectric sensors mounted between the bearing housing and the test chamber alignment bolts measure the load transmitted through the bearings (as seen in Fig. 3). The dynamic force sensors for the left bearing have a sensitivity of 118.8 mV/N (528.5 mV/lbf) and dynamic range of 44.48 N (10 lbf), while the sensors for the right bearing have a sensitivity of 12.0 mV/N (53.2 mV/lbf) and dynamic range of 444.8 N (100 lbf). The load cell signals are conditioned with unit gain for the left bearing and 10X gain for the right bearing before connection to the data acquisition system. A high-speed (up to 999,990 rpm) infrared tachometer sensor is rigidly mounted inside the test chamber to indicate the shaft speed and to provide a keyphasor signal for data acquisition. Thrust pins mounted rigidly to the test chamber prevent the axial movement of the shaft. Díaz and San Andrés [41] describe the test rig design considerations and features in further detail.

Data Acquisition

A *Bentley Nevada ADRE for Windows* DAIU system collects and records the experimental data from rotor coastdown response tests. The system has eight input channels so that all four eddy current sensor signals and a maximum of four of the six force transducer signals can be recorded. The software includes real time slow-roll subtraction, order tracking, and synchronous response filtering. The software offers a wide variety of data output options including tabular data lists, Bode diagrams, cascade plots, shaft average centerline, and spectrum plots.

Coastdown responses captured with the ADRE and the LabView data acquisition systems (DAQ) determine much of the rotordynamic performance of the test bearings. In the case of high-speed gas bearings, the ADRE maximum speed of 60,000 rpm often limits the use of the ADRE DAQ for rotordynamic analysis, thus making the LabView DAQ more appealing for recording coastdown responses from higher rotor speeds.

Observing the rotor response with an Agilent digital signal frequency spectrum analyzer (DSA) helps to identify subsynchronous and supersynchronous vibration components. The frequency at which such vibrations first occur indicates the onset (threshold) speed of instability. The spectrum analyzer also records waterfall plots of the rotor coastdown response (showing threshold speeds of instability). In addition to the Agilent DSA, a LabView DAQ board and virtual instrument captures the waterfall plots and frequency spectrums. An ad-hoc LabView virtual instrument developed by Dr. Sergio Díaz records the transient response at start up to determine rotor lift-off behavior and speeds. Measured data is easily exported from both DAQ systems for additional processing and analysis.

Observing changes in the display of the position of the shaft centerline on an oscilloscope, while gradually increasing the supply pressure, determines the feed pressure for rotor lift off. The pressure gauges indicate the supply pressure at which lifting motion occurs, and is therefore limited by the resolution of the gauge, which is

especially limited at low pressures. The mass flow rate through the feed orifices is recorded while incrementally increasing the supply pressure.

Test Bearings

Hybrid Three-lobe Bearing

The test bearings are two identical aluminum three-lobed hybrid bearings having an operating nominal radial clearance (C_r) of 66 μm, 50% offset and preload of 23 μm (Table 1 summarizes the bearing geometry).

Table 1 Characteristics of the three lobe bearing geometry[4]

Parameter	*Value*
Length (mm)	30
Diameter (mm)	29.5
Nominal Clearance (μm)	66 ± 1.27
Nondimensional Preload	0.33
Orifice Diameter (mm)	1.0
Number of Orifices	6
Orifice Location	At apex of pads (C_{max})

As shown in Fig. 5, the bearings have a length of 30 mm and diameter of 28.5 mm (L/D = 1.05, C_r/R = 4.6E-3). Three pairs of 1 mm air feed holes, spaced 120 degrees apart, are located at the apex of the lobes and provide the hydrostatic lubrication. The cylindrical bearings are held in place with axial ball bearings positioned at the sides of the bearing housing, allowing for precise axial positioning without angular misalignment via the alignment bolts.

[4] Appendix A describes the clearance measurements. Appendix B details the preload calculations.

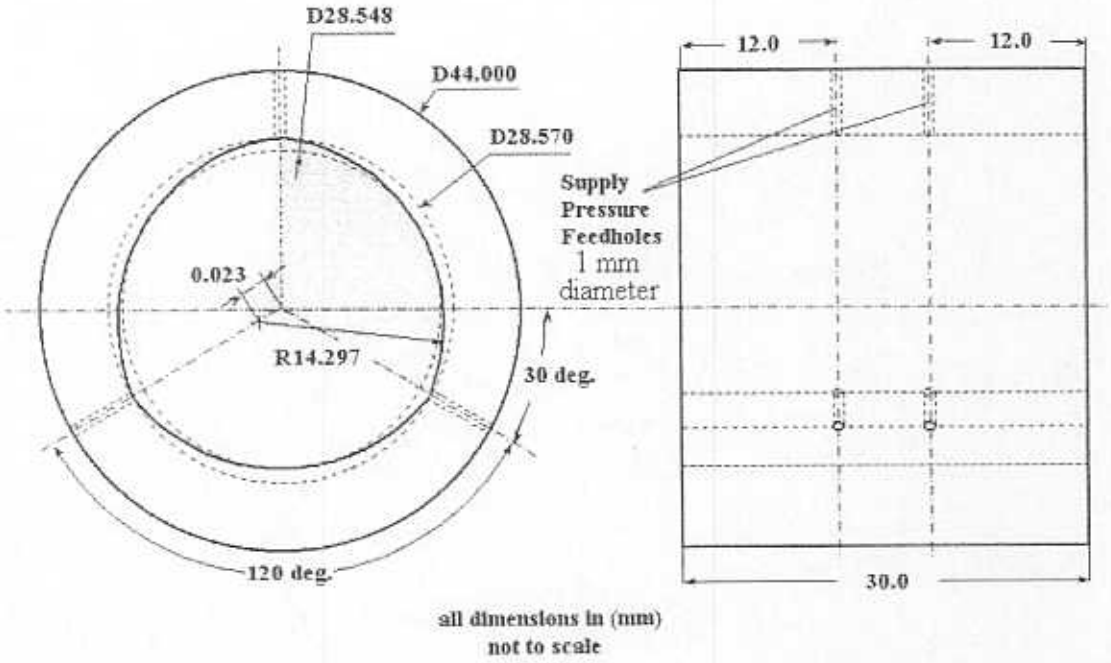

Fig. 5 Geometry of the three-lobe test bearing showing preload and orifice compensation

Fig. 6 indicates the rotor installed within the bearing and the nomenclature associated with the journal eccentricity. The bearings are installed in the load on pad position so that one pair of orifice feed holes is located in the vertical direction above the rotor, and a pair of orifice feed holes is located 120 degrees in either direction from the vertical position. Fig. 7 shows an unwrapped schematic view of the bearing geometry.

The performance of the three-lobe bearings will be compared to the dynamic performance of three-lobe pressure dam hybrid bearings and HyPad® tilting pad hybrid bearings. Appendix C gives the geometries of the three-lobe pressure dam hybrid bearings and the hybrid tilting pad hybrid bearings.

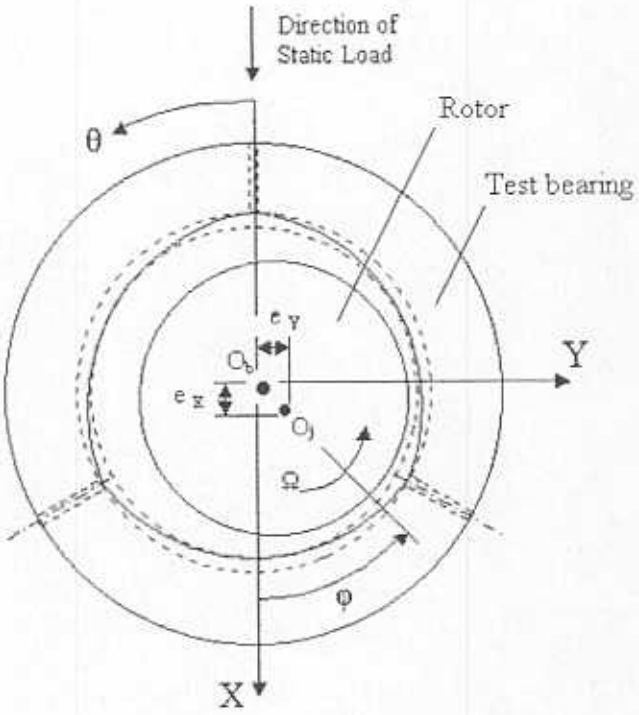

Fig. 6 Schematic view of test three lobe bearing as installed in test rig (e_X and e_Y denote instantaneous journal coordinates or eccentricities)

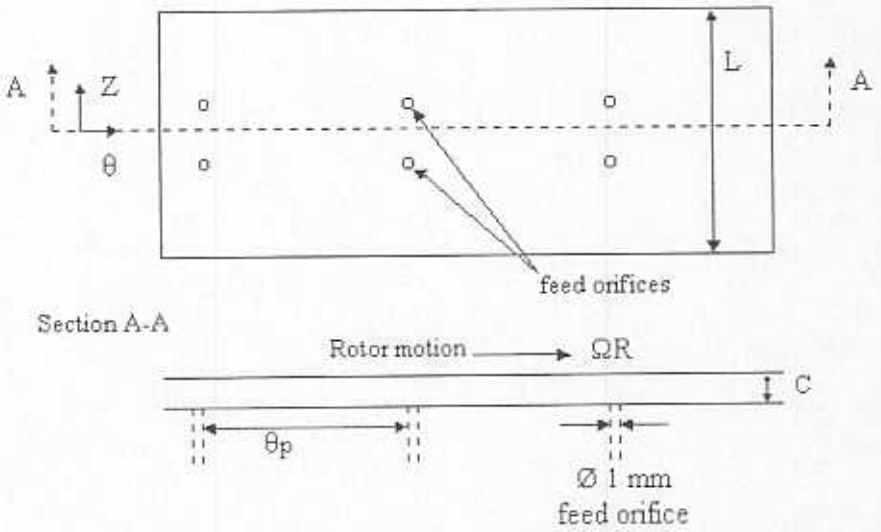

Fig. 7 Unwrapped schematic view of three lobe test bearing

EXPERIMENTAL RESPONSE OF ROTOR SUPPORTED ON THREE-LOBE BEARINGS

The static and dynamic response of the rotor supported on the three lobe bearings characterizes the overall performance of the rotor/bearing system. The feed pressure required to lift the rotor characterizes the static performance. Analysis of the rotor coast down response to calibrated imbalance masses, for increasing supply pressures, determines several performance characteristics. The imbalance response at the critical speed gives an overall damping ratio using the bandwidth or Q factor methods. Waterfall plots of the coastdown response may show the characteristic vibration patterns identifying the presence of whirl (or whip) instability and indicate threshold speeds of instability. The transient response at startup indicates rotor lift-off characteristics and speeds.

Static Performance: Feed Pressure for Rotor Lift Off

One of the great advantages of gas-lubricated bearings is significantly lowered operating friction. This advantage is not recognized until a full lubricant film develops between the rotor and the bearing(s). Therefore, the startup and touchdown stages of a rotor supported on gas bearings are critical due to the great opportunity for wear, and/or more extensive damage, caused by high friction (hard contact) before the film develops between the rotor and the bearing. Ideally, the hybrid configuration provides hydrostatic feed pressure at start and stop conditions, therefore ensuring the presence of a gas film and preventing the rotor from contacting the bearings.

A certain feed pressure, counteracting the downward force due to the weight of the rotor, lifts the rotor off the bearing and allows a complete gas film to be formed. By observing the position of the shaft indicated by the oscilloscopes, upward motion of the rotor from its static position indicates the feed pressure for rotor lift-off. Opening the supply pressure line to a pressure ratio[5] of 1.27 – 1.37 (± 0.07) lifts the rotor off the

---

[5] The supply pressure ratio is the ratio of the supply pressure to ambient pressure (both absolute values).

bearing. Upward motion of the centerline position of the shaft and rotation of the shaft from the supply pressure alone verifies that the rotor lifts due to the hydrostatic feed. The shaft normally reaches a steady rotating speed (due to the supply pressure alone) around 2000-4000 rpm, depending on the magnitude of the supply pressure. Table 2 summarizes the measured flow rate and feed pressures for rotor lift-off[6].

Table 2 Feed pressure for rotor lift-off attributes

Attributes	*Left Bearing*	*Right Bearing*
Feed pressure ratio for rotor lift-off	1.27 ± 0.07	1.34 ± 0.07
Total mass flow rate at lift-off feed pressure (kg/s)	1.10E-4 ± 3.22E-5	1.42E-4 ± 1.62E-5
Approximate mass flow rate *per orifice* (kg/s)	1.83E-5	2.37E-5

Rotor/Bearing System Dynamic Performance

Coastdown Response to Calibrated Imbalance Masses for Various Supply Pressures

The coastdown response to calibrated imbalance masses gives useful information about the rotordynamic performance of the system. Such information includes the critical speed (the speed at which the response to imbalance is the largest), the overall rotor imbalance (the magnitude of response at high speeds), the overall damping capability, and the threshold speed of instability (should the system become unstable). Measured free-free mode shapes indicate that the rotor is "nearly" rigid over the entire operable speed range of the test rig[7]. The coastdown response for increasing feed

---

[6]Appendix D contains the measured mass flow rates (with and without the rotor installed) defining the flow resistance through the feed orifices.

[7] Refer to the section entitled "Rotor Model: Free-Free Mode Natural Frequencies and Shapes" for a complete description of the measured free-free mode shapes.

pressures will also indicate the effects of hydrostatic feed pressure on the overall performance, the damping ratios, and the critical and threshold speeds.

Both the ADRE and the LabView DAQ systems are capable of capturing the displacement responses and bearing transmitted loads during the coastdown. The procedure for running a coastdown test using either DAQ is given below.

- Place the imbalance masses in the pre-determined location(s) [skip this step if the experiment is a baseline recording the remnant imbalance of the rotor]
- Insert the rotor into the test chamber and attach the chamber end plate(s)
- Verify proper connections, conditioning, and gains from eddy current sensors, load cells, and keyphasor input to the data acquisition system
- Prepare the DAQ configuration for data acquisition and start recording the response
- Turn on the supply pressure to the pre-determined value, and record the mass flow rate to the bearing chambers
- Turn motor controller power on and press the 'go' button
- Verify proper functioning of the tachometer with an indicated reading of 10.4 krpm (the minimum speed of the motor controller) at the tachometer indicator and in the DAQ
- Manually increase the rotor speed at a slow rate until the critical speed and onset speed of instability have been passed or until vibration becomes too excessive to continue increasing the speed
- Turn power to motor controller off allowing the rotor to coast down
- Stop data acquisition when coast down reaches ~4000 rpm or rotor reaches steady state rotation due to the supply pressure
- Save data file
- Record test, initial conditions, and comments on data sheet
- Verify that the imbalance masses are still in place once the rotor has stopped and the air supply is turned off [skip this step if test is a baseline]

Baseline Response

Fig. 8 and Fig. 9 display the amplitudes of the direct and the synchronous coast down displacement responses (peak to peak) from the remnant imbalance of the rotor (baseline response) for a supply pressure ratio equal to 5.08. Eddy current sensor designations indicate: LH = left horizontal sensor, LV=left vertical sensor, RH = right horizontal sensor, RV = right vertical sensor.

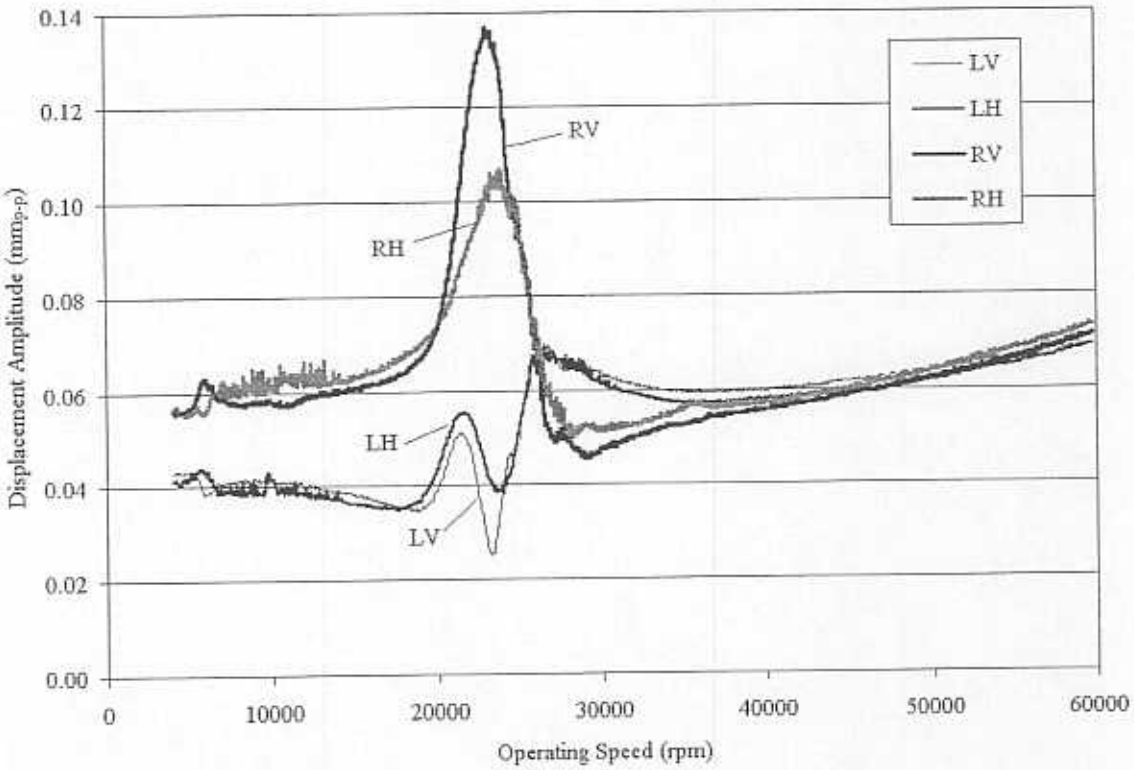

Fig. 8 Direct displacement responses from remnant imbalance of the rotor supported on three lobe bearings for supply pressure ratio equal to 5.08

There are two main differences between the direct and synchronous responses. The direct response indicates the overall response of the rotor supported on the test bearings and is a complex signal consisting of various frequencies of vibration. With the synchronous response, the frequency components corresponding to the operating

speed are kept to give the response to the remnant imbalance of the rotor alone. Therefore, the difference in magnitude of the direct and uncompensated synchronous responses indicate that the response may also contain non-synchronous vibration components, possibly caused by misalignment, excessive clearance, and rotor/bearing rubbing.

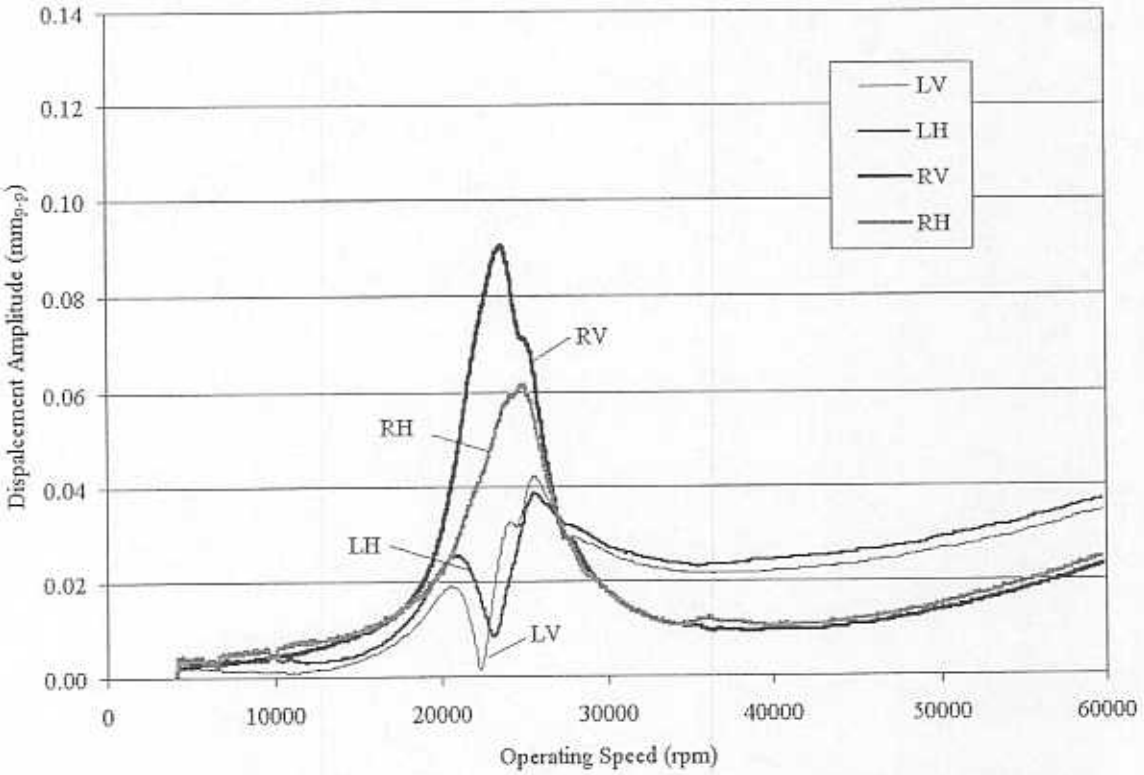

Fig. 9 Synchronous displacement responses from remnant imbalance of the rotor supported on three lobe bearings for supply pressure ratio equal to 5.08, compensated for slow roll at 4100 rpm

The second main difference is the option of slow roll compensation applied to the synchronous response. The response vector at low speed (or the slow roll vector) is essentially due to imperfections on the surface that the sensor is monitoring, also known as shaft run out, and remnant magnetism in the shaft. Applying slow roll

compensation consists of identifying the slow roll vector at low speeds (where the response vector is nearly constant), and then subtracting the slow roll vector from all other vector samples in the set, effectively forcing the response to zero at low speeds. The synchronous response in Fig. 9 is compensated for slow roll at 4100 rpm. Table 3 summarizes the speeds of the slow roll vectors for all coastdown response experiments.

Table 3 Speed (rpm) of slow roll compensation vectors

Pressure Ratio	*Remnant Imbalance*	*U1 Imbalance*	*U2 Imbalance*
2.36	5700	6000	6000
3.72	4500	5000	5000
5.08	4100	4100	5000

The direct and synchronous coastdown responses shown in Fig. 8 and Fig. 9 reveal several other general performance characteristics. It is evident that the right end of the rotor exhibits larger remnant imbalance than the left end of the rotor due to larger vibration levels through the critical speed. Viewing the inversion in vibration amplitudes at the left eddy current sensors near the critical speed, the remnant imbalance apparently excites a combination of the conical and cylindrical modes of vibration[8]. From the response at the right sensors, there is more damping in the horizontal direction than in the vertical direction indicated by the smaller and broader peak (or bandwidth) at the critical speed. Note that the compensated synchronous maximum vibration amplitude (peak to peak) at the right vertical sensor, 90 μm, exceeds the measured minimum diametral bearing clearance (C_{min}), 88 μm. This indicates that either the rotor is rubbing the bearings while traversing the critical speed, or the clearance measurements are actually too conservative.

[8] Appendix E addresses the critical speed response inversion in more detail.

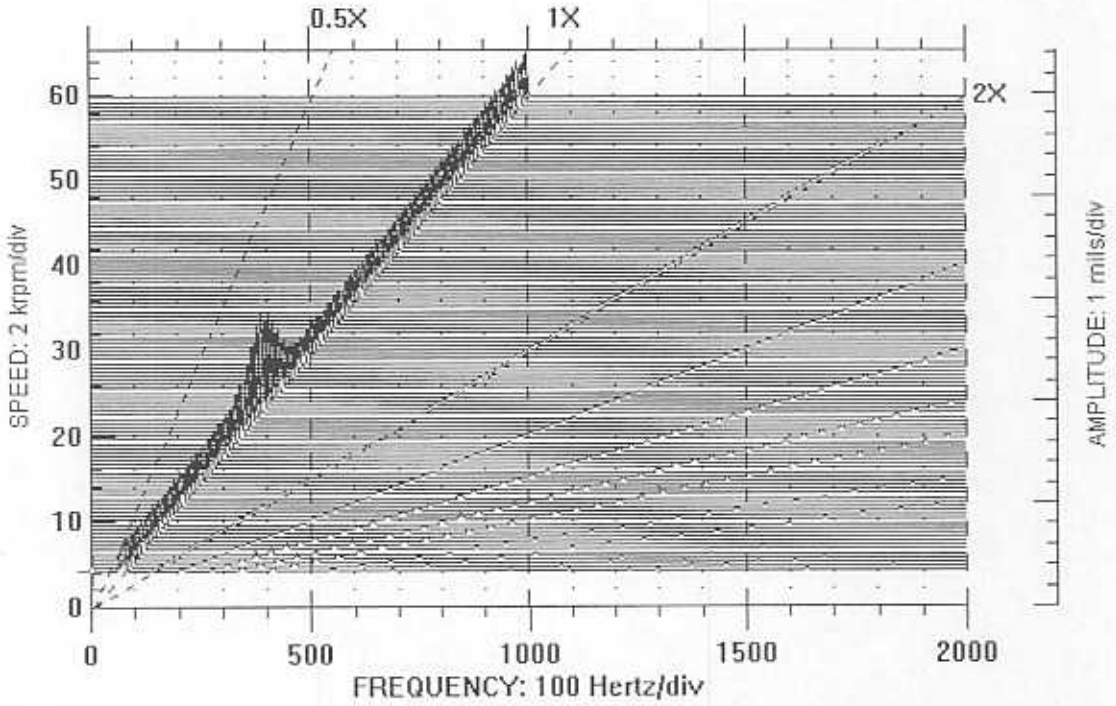

Fig. 10 Waterfall plot of coastdown response at the right vertical eddy current sensor to remnant imbalance of rotor supported on three lobe bearings for supply pressure ratio equal to 5.08

Fig. 10 shows a waterfall plot for the baseline response in Fig. 9. A waterfall plot consists of the spectral lines of vibration versus speed, giving a three dimensional chart of the coastdown response. The figure confirms that the rotor is not rubbing, since no 0.5X subsynchronous vibration components, no sideband frequencies, and only low levels of 2X supersynchronous vibration component occur through the critical speed (these are frequency components indicative of rotor/bearing rub). In fact, no subsynchronous vibration appears, indicating that the system is stable (free from subsynchronous whirl), and that mainly shaft runout and small levels of supersynchronous frequency components contribute to the differences between the direct and the synchronous responses.

Fig. 11 shows the coastdown response to the remnant imbalance of the rotor for increasing supply pressure ratios. The figure shows the influence of the supply

pressure in the several ways. First, larger supply pressure provides more stiffness as indicated by an increase in the critical speed (from 15,750 rpm to 23,500 rpm for feed pressure ratios equal to 2.36 to 5.08, respectively). Secondly, the damping ratio decreases as supply pressure increases since the magnitude of response at the critical speed is lower for lower supply pressure ratios. As the damping ratio decreases, a smaller and broader peak response becomes larger and narrower. Lastly, the responses show similar values of remnant imbalance (the peak to peak response at 39,000 rpm is approximately 9.4 μm) for all supply pressures, since the supply pressure cannot physically change the remnant imbalance of the rotor. The response begins to increase at larger speeds (upwards of 60,000 rpm) as the system approaches the second critical speed (which should occur around 115,000 rpm).

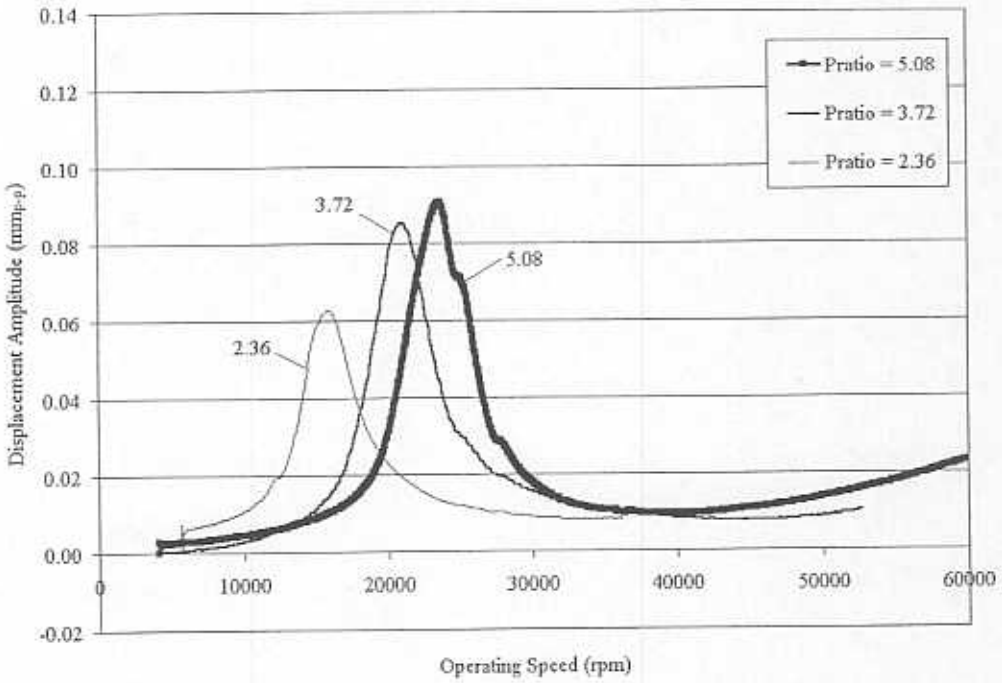

Fig. 11 Synchronous displacement remnant imbalance response of the rotor supported on three lobe bearings. Measurements at the right vertical eddy current sensor for increasing supply pressure ratios (with slow roll compensation according to Table 3).

Fig. 12 shows influences of the supply pressure on the bearing transmitted loads. The figure displays the coastdown transmitted bearing forces recorded by the transducer located 120 degrees clockwise from vertical at the right bearing. The location and magnitude of the peak to peak responses indicate an increase in stiffness and a decrease in damping ratio (similar results as with the displacement response). Although not shown here, the bearing transmitted forces are of similar magnitude (for a given supply pressure) at all three load transducers. Values of transmitted forces are as large as 34 N (peak-to-peak) at the critical speeds, and nominally 4.3 N (peak-to-peak) at higher speeds.

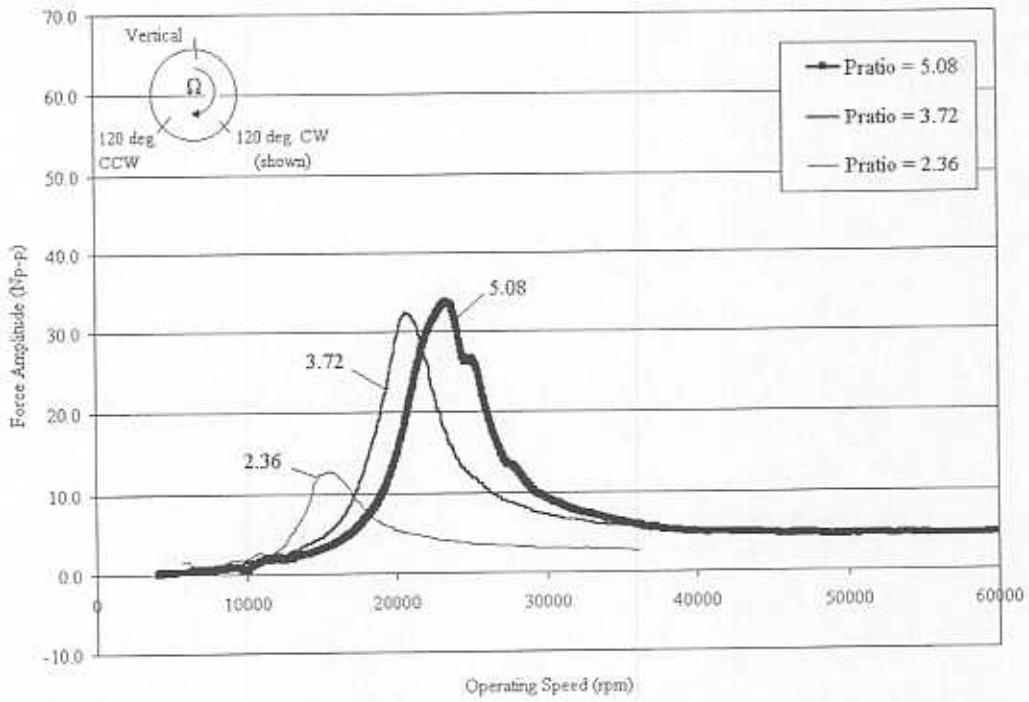

Fig. 12 Force response from remnant imbalance of rotor supported on three lobe bearings. Measurements with load transducer at 120 degree clockwise (from vertical) load transducer for increasing supply pressure ratios. Insert shows location of load cells.

For increasing feed pressures, Table 4 gives the peak-to-peak amplitudes of synchronous displacement at the critical speed and with reference to the amplitudes for

supply pressure ratio equal to 5.08, and with reference to the nominal clearance. Comparing the response at the left vertical sensor to the response at the right vertical sensor shows a 1:2 relationship of amplitudes at each supply pressure. This large variance between the responses at the left and right bearings is presumably due to inherent imbalance in the rotor[9]. The amplitudes of vibration at both sensors increase for increasing supply pressures and are not larger than the nominal clearance at the left bearings for any feed pressure.

Table 4 Remnant imbalance response amplitude ratios determined from the synchronous coastdown response of rotor supported on three lobe bearings (nominal diametral clearance = 132 μm)

Sensor Location	*Supply Pressure Ratio*	*Critical Speed (rpm)*	*Peak to Peak Amplitude at Critical Speed (mm)*	*Ratio of Amplitudes = Amp at PR / Amp at PR 5.08*	*Ratio of Amplitudes = Amp/Nominal Clearance*
Left Vertical	5.08	254,50	0.042	1.000	0.318
	3.72	21,500	0.041	0.976	0.311
	2.36	16,400	0.030	0.714	0.227
Right Vertical	5.08	23,500	0.090	1.000	0.682
	3.72	20,900	0.085	0.940	0.644
	2.36	15,750	0.063	0.700	0.477

Imbalance Response

Equation [1] determines the imbalance displacement (u), where (m) is the calibrated imbalance mass, (R') is the radial location at which the imbalance mass is placed, and (M) is the rotor mass per bearing. For this testing series, m = 0.088 g or 0.066 g (± 0.002 g), R' = 12 mm (± 0.05 mm), and M = 413.5 g (± 0.5 g). The

[9] The 'Free-Free Mode Natural Frequencies and Shapes' section addresses this inherent imbalance in further detail.

imbalance mass can also be placed in several different imbalance holes which are labeled according to the scheme shown in Fig. 13. The hole numbers correspond to the same axial line at both rotor ends. The test imbalance masses are placed in hole 2 for all coastdown experiments since this hole is available at both ends (some holes contain prior balancing masses). This imbalance mass setup excites the cylindrical mode of vibration rather than the conical mode.

$$u = \frac{m\,R'}{M+m} \qquad [1]$$

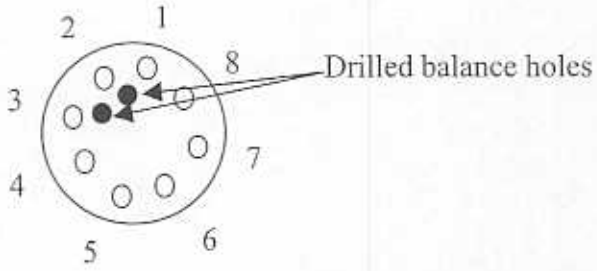

Fig. 13 Right end view of test rotor showing numbered imbalance holes

Table 5 gives the imbalance mass setup for coast down experiments. Note that imbalance *U1* is larger than imbalance *U2*, and are both larger than the remnant imbalance of the rotor. Therefore, if the system responds linearly one expects the response due to imbalance *U1* to be larger than the response due to imbalance *U2*, and both responses to be larger than the remnant imbalance response.

Table 5 Imbalance setup for imbalance response testing of rotor supported on three lobe bearings

Imbalance Name	Imbalance Displacement (u)			
	Left End	*Right End*	*Imbalance Mass*	*Mode Excited*
Remnant	None	None	None	None
U1	u = 2.57 μm ± 0.08	u = 2.57 μm ± 0.08	0.088 g ± 0.002 g	Cylindrical
U2	u = 1.93 μm ± 0.08	u = 1.93 μm ± 0.08	0.066 g ± 0.002 g	Cylindrical

As shown in Fig. 14, the displacement amplitudes with imbalance *U1* are in fact larger than the displacement amplitudes with imbalance *U2*, but the response to imbalance *U2* is actually smaller than the remnant imbalance response. The imbalance mass *U2* configuration provides additional balancing to the remnant imbalance of the rotor, while the imbalance mass configuration *U1* is large enough to start unbalancing the rotor.

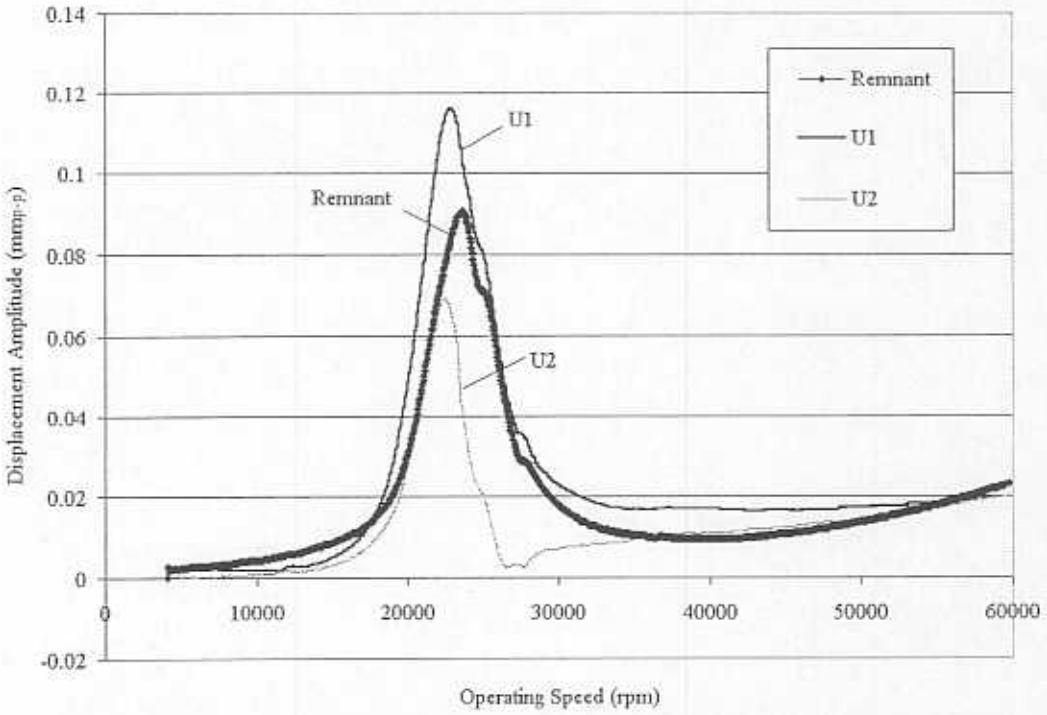

Fig. 14 Imbalance displacement responses at the right vertical eddy current sensor with rotor supported on three lobe bearings for supply pressure ratio equal to 5.08 (with slow roll compensation)

Even though vibration levels while traversing the critical speed with imbalance *U1* are larger than the nominal clearance, Fig. 15 shows no evidence of rotor/bearing rub indicating clearance measurements are even more conservative than discussed with the remnant imbalance response.

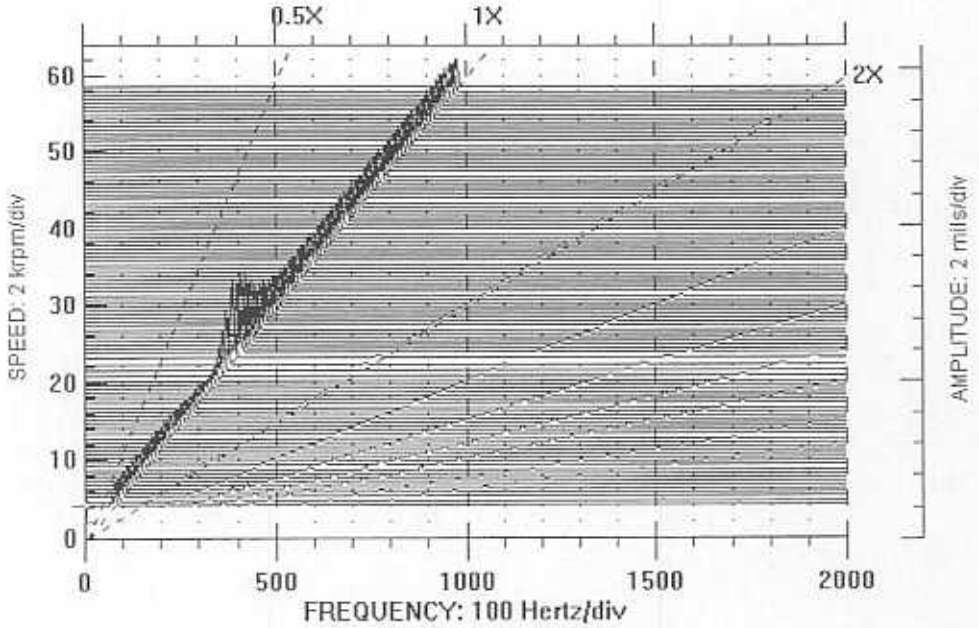

Fig. 15 Waterfall plot of *U1* coastdown response for rotor supported on three lobe bearings at pressure ratio equal to 5.08

Interestingly, Fig. 16 shows larger magnitudes of bearing transmitted forces for both imbalance configurations than for the remnant imbalance response. Transmitted forces at the critical speed are as large as 62 N peak-to-peak (peak amplitudes for *U1* are roughly two times the amplitudes for *U2*) and 4.8 to 7.8 N peak-to-peak at high speeds.

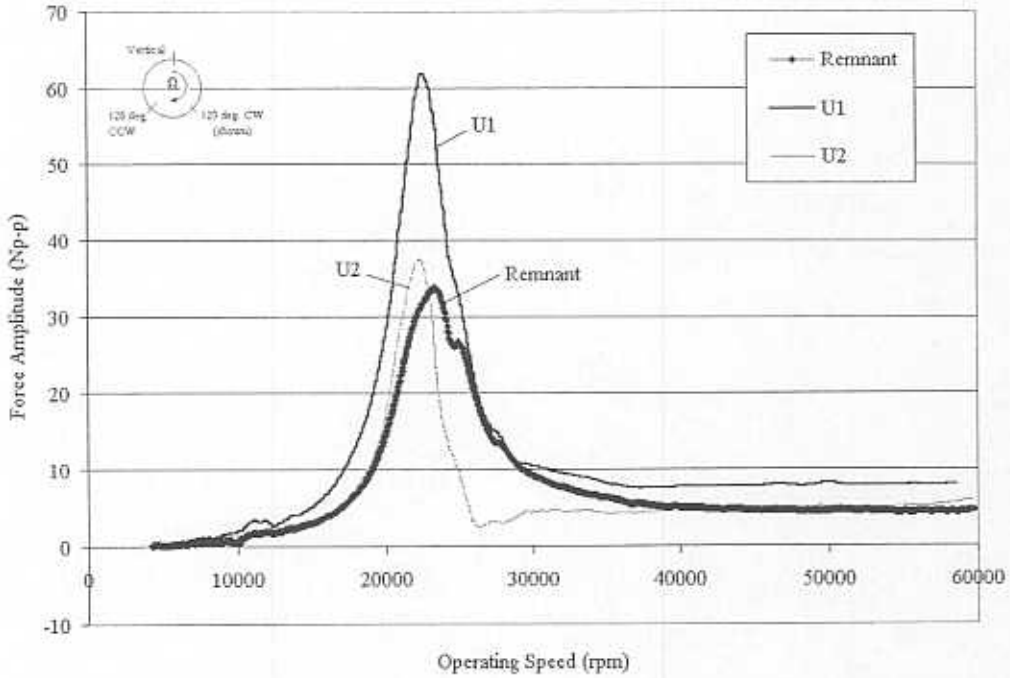

Fig. 16 Transmitted forces due to imbalance *U1* and *U2* responses of rotor supported on three lobe bearings at load transducer 120 degrees clockwise with supply pressure ratio equal to 5.08

Damping Ratios

The bandwidth and Q factor methods allow estimation of the viscous damping ratio (ξ), a measure of modal damping, by using the response peak at the critical speed (or bandwidth) from the coastdown synchronous response. For each method, Equations [2] and [3] show the formulae applied along with the variables of interest. Fig. 17 defines the notation used in both methods. It should be noted that these methods are only valid for systems with relatively small damping, since the natural frequency (N_n), is equal to the critical speed only for systems with little damping (less than 10 percent).

$$\xi = \frac{N_2 - N_1}{N_2 + N_1} \qquad [2]$$

$$for \quad \xi \leq 0.1$$

$$Q = \frac{1}{2\xi}$$

$$Q = \frac{N_n}{N_2 - N_1} \qquad [3]$$

$$for \quad \xi \le 0.1$$

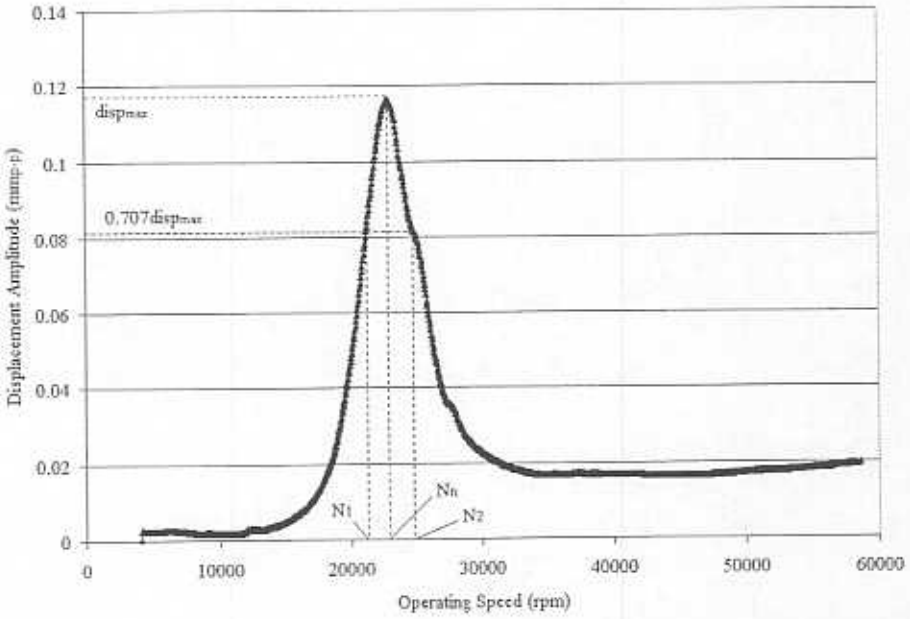

Fig. 17 Notation for estimating the viscous damping ratio using the bandwidth or Q factor methods

Table 6 summarizes the damping ratios determined from the synchronous (remnant imbalance and calibrated imbalance) responses at all sensor locations using the bandwidth and the Q factor methods for supply pressure ratios equal to 5.08, 3.72, and 2.36[10].

[10] Appendix F lists all amplitudes of displacement and speeds for the damping ratio estimation.

Table 6 Damping ratios determined from the experimental synchronous coastdown of the rotor supported on three lobe bearings[11]

Sensor	*Imbalance Condition*	*Supply Pressure Ratio*	*Critical Speed (rpm)*	*Damping Ratio (Bandwidth Method)*	*Damping Ratio (Q factor Method)*
RV	Remnant	5.08	23,500	0.094	0.095
		3.72	20,900	0.093	0.093
		2.36	15,750	0.124	0.126
	U1	5.08	22,790	0.076	0.077
	U2	5.08	22,240	0.056	0.056
RH	Remnant	5.08	24,950	0.075	0.073
		3.72	20,400	0.094	0.098
		2.36	15,350	0.086	0.088
	U1	5.08	22,540	0.079	0.081
	U2	5.08	22,390	0.060	0.059
LV	Remnant	5.08	25,490	0.077	0.077
		3.72	21,500	0.071	0.072
		2.36	16,340	0.113	0.121
LH	Remnant	2.36	16,100	0.075	0.077
	U1	5.08	22,490	0.144	0.151
	U2	5.08	22,050	0.192	0.206

There is good agreement between the two methods, but damping ratio values approach and, at pressure ratio equal to 2.36, exceed the criterion that the damping should be less than 10 percent. Although Fig. 18 shows no definite pattern linking

[11] Note that the responses at pressure ratios equal to 5.08 and 3.72 at the left vertical sensor and the imbalance responses at the left horizontal sensor are not included. Responses for these conditions are discussed in Appendix E.

damping ratio with supply pressure, damping ratios appear to decrease with increasing supply pressure.

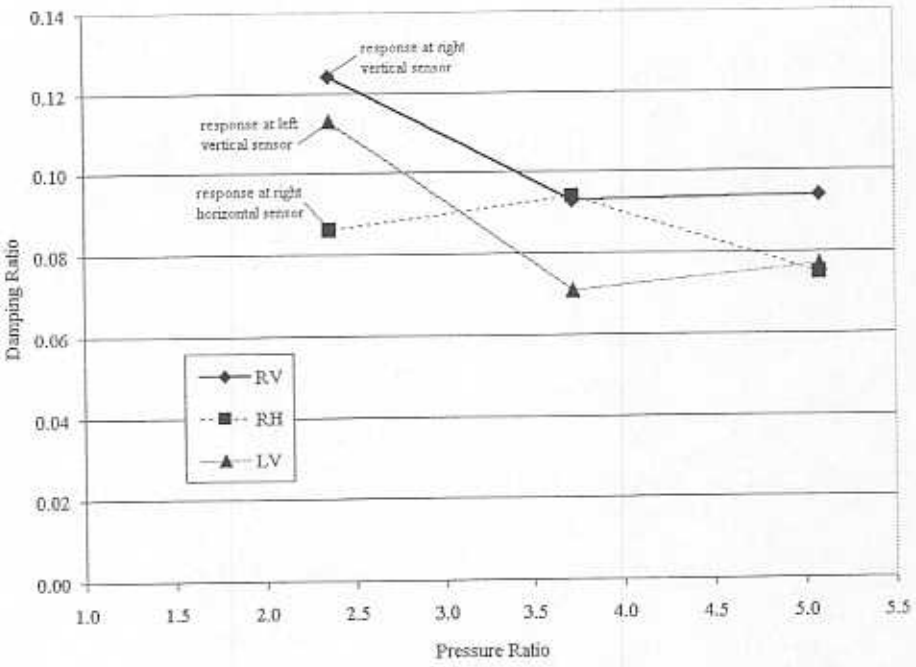

Fig. 18 Damping ratios for increasing supply pressure at three eddy current sensor locations

Threshold Speeds of Instability

The LabView DAQ records waterfall plots of the coast down response for determining threshold speeds of instability. Table 7 details the setup configuration used with the Waterfall.VI [42]. The instrument collects spectral data every 2000 rpm. The LabView DAQ allows data collection for eight channels at a time while observing one channel on the acquisition interface. A MathCAD program [43], processing the output data files allows further analysis of the onset of instability, whirl frequency ratios, and response amplitudes. While the ADRE DAQ also generates waterfall plots, the DAQ speed limit of 60,000 rpm sometimes limits the capability of capturing the

threshold speed at higher supply pressures, often making the Waterfall.VI a more viable acquisition system.

Table 7 LabView Waterfall.VI DAQ configuration

Parameter	*Value*
Trigger Level	3.3 Volts
Trigger Type	Software Analog
Sample Size	1024
Sampling Frequency	12,000 Hz
Start rpm	67,000 rpm
Rpm Step	2000 rpm
End rpm	2000 rpm
Window	None (uniform)
Spectrum Type	Vrms

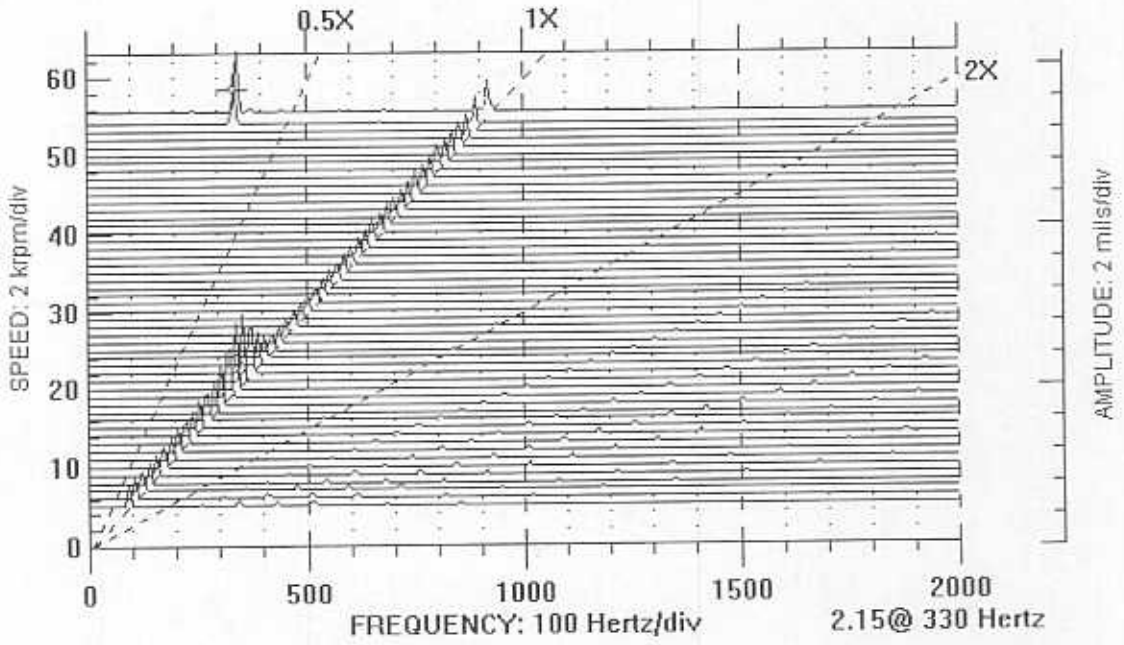

Fig. 19 Waterfall plot of rotor response to remnant imbalance at right vertical eddy current sensor with pressure ratio equal to 3.72

Fig. 19 shows an example of the threshold speed captured with the waterfall plot collected by the ADRE DAQ (rotor coastdown response to the remnant imbalance

for supply pressure ratio equal to 3.42). The rotor traverses the critical speed and continues in a stable condition until reaching the threshold speed of instability where a subsynchronous frequency just below the natural frequency (critical speed) becomes excited sending the rotor into whirl instability. For this example, the ratio of the whirl frequency (330 Hz) to the threshold speed (890 Hz), known as the whirl frequency ratio (*WFR*) is 0.37. The whirl frequency increases (although not seen in the plot) until reaching the natural frequency (348 Hz), incurring whip instability where the whirl frequency remains locked at the natural frequency value as the operating speed continues to increase. Once unstable, rotor vibration levels often become violently large making operation above the threshold speed of instability quite dangerous. Therefore, the threshold speed is a good measure of system performance, i.e. designers usually want to operate to the highest speed possible while maintaining safe vibration levels. The three lobe bearings operate free from any other subsynchronous vibration, until reaching the threshold speed of instability, for all supply pressure ratios.

As mentioned earlier, the hydrostatic feed tends to stiffen the rotor/bearing system and increases the critical speed for increasing supply pressures. Likewise, the threshold speeds of instability also increase with increasing supply pressures. Fig. 20 clearly shows a linear relationship, rendering much higher threshold speeds at higher feed pressures. It is important to note that the threshold speeds in Fig. 20 are obtained as the rotor is run up in speed, as opposed to coast down. Threshold speeds bringing the rotor to stable performance, as determined from a coastdown, tend to be slightly lower due to the very low damping of the system.

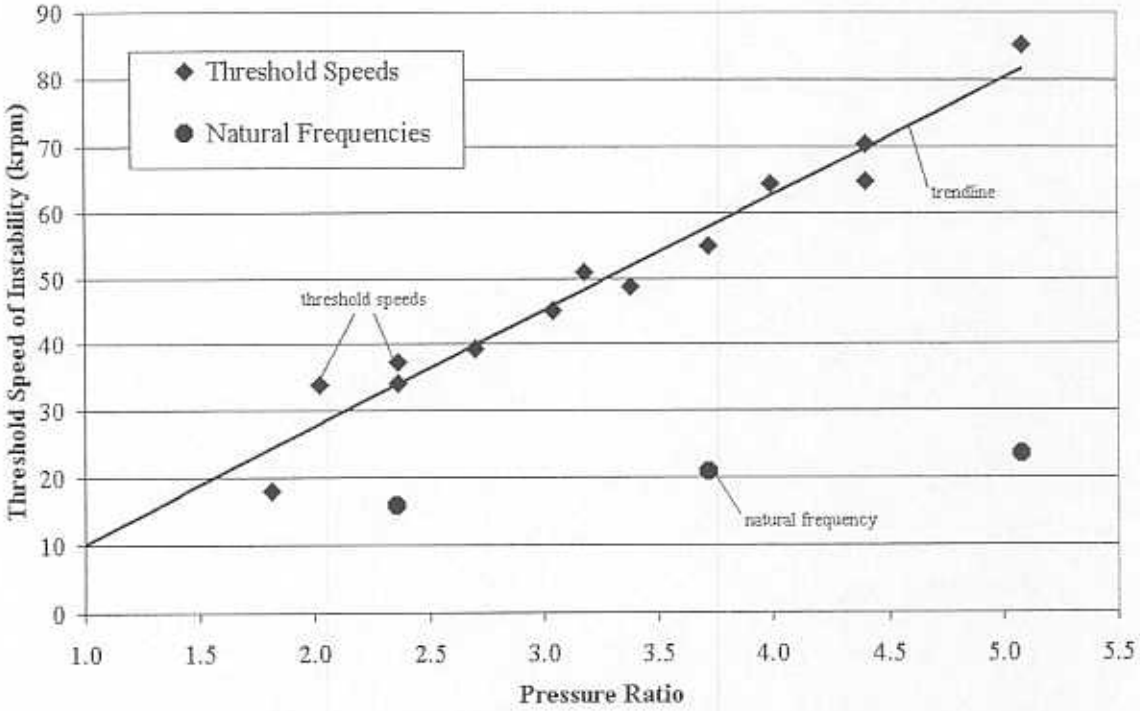

Fig. 20 Threshold speeds of instability and natural frequencies determined on speed run up for rotor supported by three lobe bearings

Fig. 21 indicates that the whirl frequency ratio decreases with increasing supply pressure and shows that the purely hydrodynamic configuration (supply pressure ratio 1.0) should exhibit a WFR of 0.49, which is nearly the characteristic half-whirl associated with oil-lubricated bearings[12]. Threshold speeds were not attained for supply pressure ratios below 1.82 due to rotor bearing rub at low supply pressures. Fig. 20 and Fig. 21 demonstrate another major advantage of hybrid gas-lubricated bearings: hydrostatic feed (with a pressure ratio equal to 5.08) increases the threshold by a factor of eight over the purely hydrodynamic case before whirl instability sets in. Threshold frequencies are four times the natural frequency, rather than two times for the hydrodynamic case.

---

[12] Appendix G lists the threshold frequency, whirl frequency, and whirl frequency ratio values.

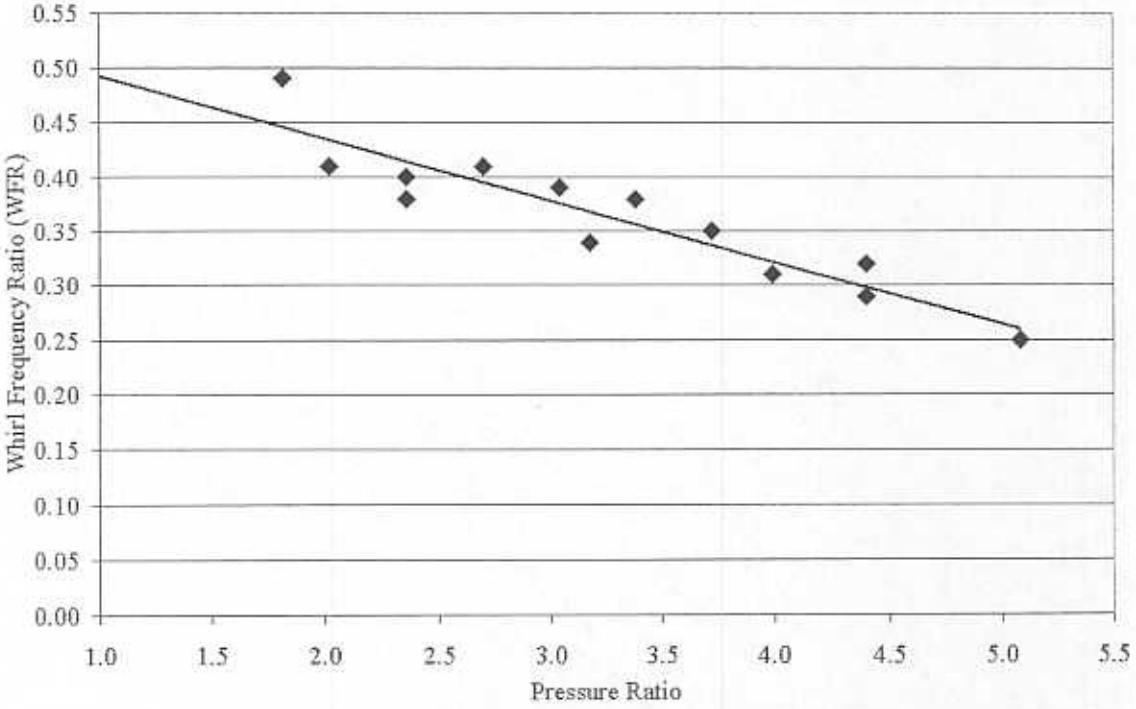

Fig. 21 Whirl frequency ratio determined on speed run up for rotor supported by three lobe bearings

Transient Response

Since the start up behavior is crucial to the reliable and sustained performance of gas-lubricated bearings, where contact friction can cause damaging wear, the transient response gives useful information about start up speeds, time until the rotor fully lifts-off from the bearing, and lift-off characteristics. The transient response determines the minimum feed pressure for operation and the effect of feed pressure on such performance characteristics[13].

An existing LabView virtual instrument [44] was modified to capture the transient response at rotor start up. The instrument triggers when the 'Go' button on the motor controller is depressed and records approximately four seconds of data at all

---

[13] All results presented in this section are with respect to the uncoated rotor. Refer to the "Surface Condition and Low-Friction Coating" section for lift-off results with the coated rotor.

four eddy current sensors and at the load cell transducers located 120 degrees from vertical at the left and right bearings (total of six data signals). The procedure for recording a transient response is as follows:

- With the rotor installed in the test bearings, turn the supply pressure to the predetermined test value.
- Allow the system to reach steady state (rotor may rotate due to the supply pressure).
- Prepare DAQ setup to record the baseline response.
- Turn the motor controller power on. This forces the motor to a stationary position presumably at the center of the motor armature. Furthermore, the center of the motor armature is not necessarily the center of the bearing(s) due to any misalignment)[14].
- Record and save the baseline response.
- Prepare the DAQ setup to record the transient response.
- Start data acquisition; press the 'Go' button to initialize the motor to rotate (from 0 rpm to the motor controller minimum speed of 10,400 rpm).
- Save the transient response and stop the data acquisition.
- Allow the rotor to coast down by turning power to the motor controller off.

---

[14] The action of centering the rotor within the motor armature effectually distinguishes the aforementioned feed pressure for rotor 'lift-off' from the lift-off supply pressure in the following discussion.

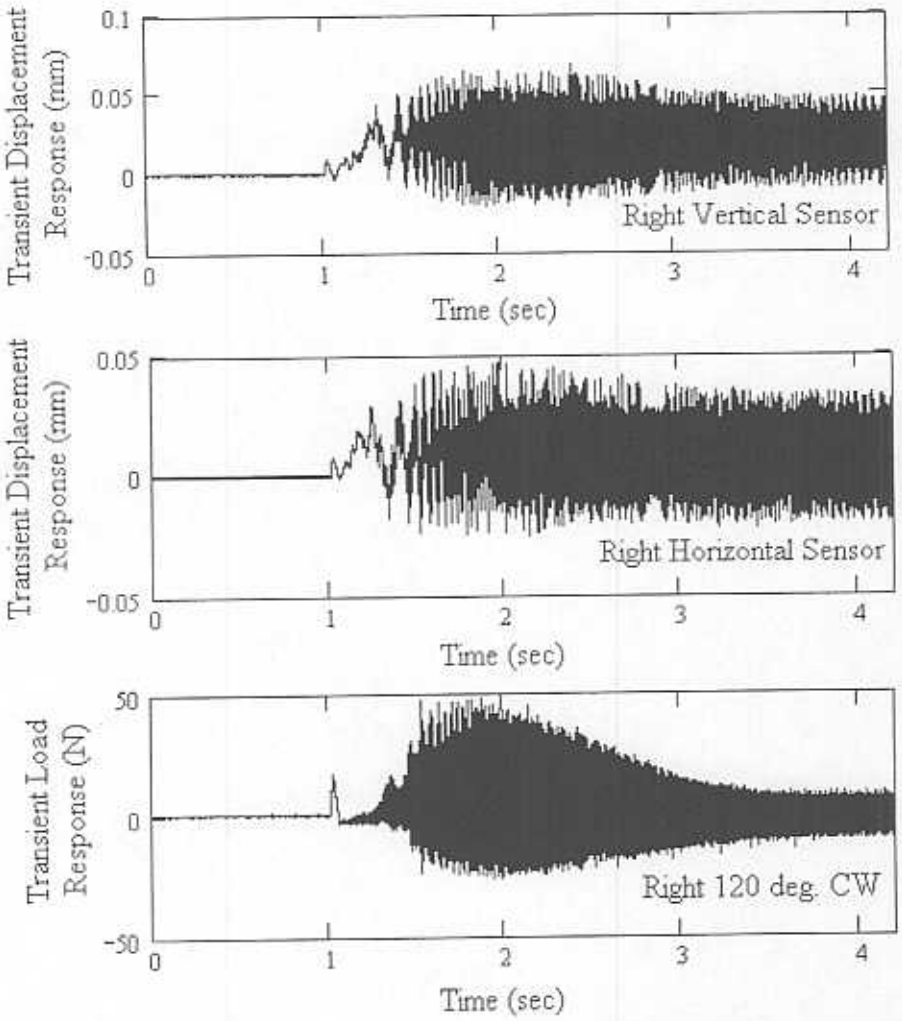

Fig. 22 Transient time response (displacements and transmitted load) of uncoated rotor supported on three lobe bearings with pressure ratio equal to 5.08

Fig. 22 displays the transient response from the three sensors at the right bearing with a supply pressure ratio equal to 5.08. A considerable delay occurs from the start of the data acquisition to when the rotor actually begins to roll or rotate (approximately 1.0 seconds in Fig. 22). Vibration levels at the horizontal and vertical sensors are of nearly equal magnitude. In the force response, an initial spike occurs as the rotor first begins to rotate, the response drops (for about 0.4 seconds) while displacement vibration levels are very small, and then begins to pick up the same

pattern as the displacement as the rotor speed increases. The force response becomes significantly smaller towards the end of the transient sample as the rotor reaches the minimum speed of the motor controller (displacement vibration levels also become more constant as this speed is reached).

During a transient test, the rotor begins from a semi-rigid contact, i.e. the motor holds the rotor stationary and is therefore sometimes resting on the bearings. As the rotor increases in speed, the rotor transitions to a floating position when the rotor lifts off the bearings by the supporting gas film. At this point, the rotor/bearing system is considered flexible with some amount of stiffness and damping, and therefore develops a natural frequency vibration component. Rotor liftoff occurs when the locked 340 Hz (to 350 Hz) frequency component appears. Fig. 23 displays a contour plot of the transient response in waterfall format, i.e. the horizontal axis displays frequency while the vertical axis shows the sample spectral lines at increasing time. Three spectral lines are displayed to the left of the contour plot at spectral lines 20 (1.3 seconds), 33 (2.2 seconds), and 60 (4.0 seconds). The contour plot assigns an amplitude threshold so that high levels of vibration appear as green-red, medium levels of vibration appear as blue, and low levels of vibration appear as purple.

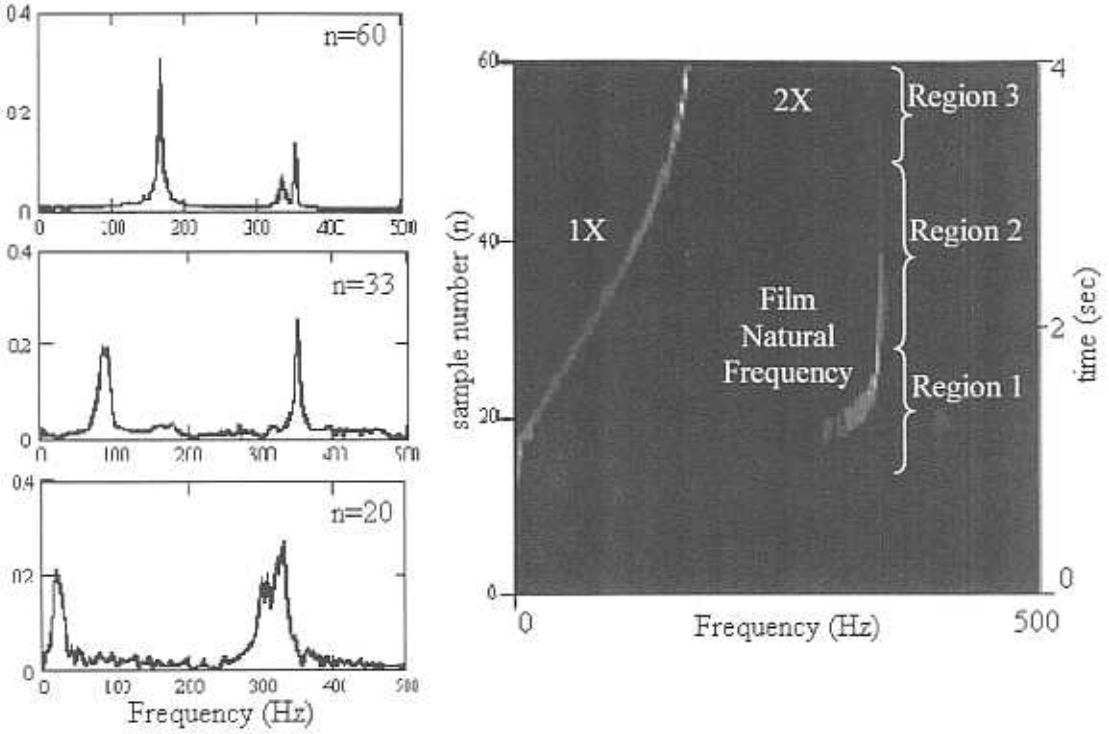

Fig. 23 Waterfall contour plot of displacement transient time response of uncoated rotor with pressure ratio equal to 3.72[15]. At sample 60: 1X = 168 Hz, 2X = 332 Hz, and natural frequency of the rotor/film system= 351.6 Hz.

Three separate regions are observed in the waterfall (contour) plot shown in Fig. 23. Within the regions, the synchronous vibration component and the natural frequency of the rotor/gas bearing system are observed as separate bright-green lines (indicating high vibration levels). Region 1 occurs when the rotor is in semi-rigid contact with the bearings and transitioning to rotation (approximately samples 16-30). Within this region, the rotor is rolling to lift-off from the bearing. The system natural frequency line begins to develop. Region 2 begins when the rotor has lifted and the system natural frequency (352 Hz) is observed (approximately samples 33-48). The rotor continues to increase in speed during region 2 and the (constant) natural frequency exists. Region 3 mainly shows the synchronous imbalance response and

[15] Refer to the "Surface Condition" section for responses with the PTFE coated rotor.

small levels of 2X synchronous speed where the rotor is still slightly increasing in speed. In this region, the vibration with constant natural frequency exists but overall vibration levels are smaller.

Observing the synchronous vibration component of the spectral line at which the rotor/gas film natural frequency fully develops determines the lift-off speed. Similarly, the time elapsed from the start of the sample set to the identified spectral line gives the lift-off time. Table 8 details the lift-off speed and time for increasing supply pressures. The lift-off speed increases with increasing supply pressure, but then decreases slightly for supply pressure ratio equal to 5.08. Aside from supply pressure ratio equal to 2.09, lift-off time also increases with increasing pressure. The feed pressure inflicts a certain amount of viscous drag at start up so that for higher supply pressures a higher lift-off speed with a longer startup results.

Table 8 Lift off characteristics with (uncoated) rotor supported on three lobe bearings

Supply Pressure Ratio	*Lift-off Speed (rpm)*	*Lift-off Time (sec)*
2.22	1170	1.536
2.36	2109	1.470
3.72	2578	1.536
5.08	2344	1.664

Gradually decreasing the starting supply pressure supporting the rotor, until the rotor is unable to rotate during the transient, determines the minimum feed pressure for operation. The lubricant film must overcome several other factors when considering startup at low supply pressures. The three-phase bi-polar configuration of the motor raises questions about how constantly the start-up torque is delivered. And if not delivered in a constant manner, the rotor may move considerable distances within the bearing due to the magnetic pull of the electric motor. This magnetic pull, with the help of gravity, can cause the rotor to be caught between the magnetic poles of the motor, thereby grabbing the rotor in a stationary position. A fragile balance between these factors and the feed pressure is overcome at supply pressure ratio equal to 2.09

and 4.31E-4 kg/s total mass flow rate (20.0 L/min). For supply pressures (or mass flow rates) lower than this, the rotor becomes stuck during run up or does not rotate at all.

Closure for Experimental Response of Rotor Supported on Three Lobe Bearings

The experimental coastdown response of the rotor supported on hybrid three lobe bearings gives valuable information about the bearings' static performance and dynamic stability characteristics.

Low feed pressure ratios are needed to statically lift the rotor off from the support bearings. Feed pressures ratios for rotor lift-off are between 1.27 and 1.37, ensuring a hydrostatic gas film. Critical speeds (natural frequencies) are determined from clearly defined peak responses at the right bearing. A peak response inversion at the left bearing (presumably due to the definition of the slow roll vector and/or the combined excitation of the conical and cylindrical modes) makes defining critical speeds and damping ratios difficult. Vibration levels and natural frequencies increase for increasing pressure ratios. Vibration levels appear to exceed minimum clearances, but waterfall plots evidence no bearing rubbing. Measured bearing transmitted forces (peak to peak) are approximately 34 N at the critical speed at high pressure ratios, and reduce to approximately 4 N at high speeds (upwards of 40,000 rpm).

The rotor response to two levels of calibrated imbalance masses show mixed results. The smaller imbalance mass provides additional balancing to the remnant imbalance of the rotor, while the larger imbalance mass leads to increased vibration amplitudes. Bearing transmitted forces are nearly doubled with the larger imbalance mass at high pressure ratios (equal to 5.08).

Damping ratios are estimated using the bandwidth and Q factor methods from the synchronous coastdown responses for increasing pressure ratios. The responses to remnant imbalance give values ranging from 12.6% to 7.2% depending on supply pressure, and appear to decrease with increasing supply pressure.

A linear relationship exists between threshold speed of instability and pressure ratio. Whirl frequency ratios decrease with increasing pressure ratio (WFR equal to 0.25 at pressure ratio equal to 5.08). The projected trendline shows whirl frequency ratio equal to 0.49 for the purely hydrodynamic film (pressure ratio equal to 1.0).

From the transient response, lift-off speeds and times are determined at the development of the rotor/bearing natural (fixed) frequency vibration component. Speeds when the rotor transitions from rolling up the bearing side to a gas film condition range from 1170 rpm to 2578 rpm depending on supply pressure. Lift-off times range from 1.470 seconds to 1.664 seconds. The minimum feed pressure needed to support the rotor for lift-off (rotation) corresponds to a pressure ratio equal to 2.22 (total mass flow rate equal to 4.31E-4 kg/s).

Overall, the three lobe bearings offer a simple design, considering cost and manufacturability, with repeatable performance. While the rotor supported on the three lobe bearings does eventually experience rotordynamic instability, the rotor is capable of much higher speeds than if supported on purely hydrodynamic gas bearings. An increase in supply pressure ratio allows for even higher speed stable operation, albeit with less damping ratio while crossing a critical speed region.

ROTORDYNAMIC ANALYSIS OF TEST ROTOR SUPPORTED ON THREE LOBE GAS BEARINGS

The rotordynamic analysis consists of modeling the test rotor with XLTRC^2 Analytical Software Suite [45], modeling the test bearings using a finite element program for solving the ideal gas Reynolds equation detailed by San Andrés [20], and performing a linear stability rotordynamic analysis to assess the stability performance characteristics of the rotor/bearing system. The finite element model of the ideal gas Reynolds equation determines the pressure profile and mass flow of the lubricant film, which is then used to define bearing force coefficients as a function of frequency ratio (the ratio of the excitation frequency to the operating speed). The stability analysis includes examination of the damped natural frequencies, stability map, threshold speeds, whirl frequency ratio at the instability threshold, and vibration modes. A synchronous rotor response prediction to imbalance shows the ability of the rotor to traverse critical speeds. Comparisons are made between predicted and experimental responses.

Predicted Bearing Performance

The inertialess and isoviscous flow within the lubricant film is described by the ideal gas Reynolds equation combining components due to shear and external pressurization. The flow due to the external pressurization is defined by the ratio of gas film and supply (or applied) pressure, as well as the geometry of the orifice. The pressure drop from the feed orifice to ambient conditions at the bearing edge occurs at the curtain area ($\pi\, d\, C$), as shown in Fig. 24. The feed orifice geometry (also shown in Fig. 24) identifies an inherent type restriction occurring at the curtain area to prevent the flow versus pressure time lag associated with pneumatic hammer instability.

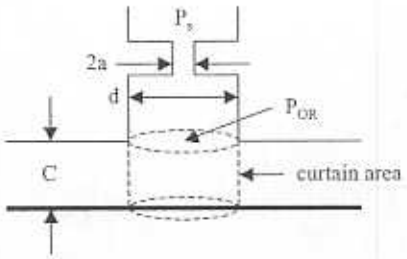

Fig. 24 Geometry of feed orifice in gas bearing

For dynamic analysis of the gas bearing film, the journal is assumed to execute small amplitude motions with frequency (ω) about an equilibrium position, determined by the improved static load. Corresponding perturbations of the film thickness and film pressure follow about the equilibrium position. Applying these perturbations to the ideal gas Reynolds equation defines the equilibrium and perturbed pressure fields within the lubricant film. The pressure fields determine the fluid film reaction forces in terms of impedance coefficients, which can be expressed as the stiffness and damping force coefficients. Note that the compressibility of the thin fluid film imposes a frequency dependence on the bearing force coefficients.

A model developed by Faria [17] and further described by San Andrés and Wilde [20], is based on finite elements and utilizes high order shape functions to prevent numerical instability at high bearing speed numbers[16]. Table 9 details the bearing geometry while Table 10 details the physical operating conditions of the rotor/bearing system.

---

[16] For the rotor supported on three lobe bearings, bearing speed numbers range from 4.86 to 48.6 in the speed region 10 krpm to 100 krpm. The bearing speed number is defined as: $\Lambda = \frac{6\,\mu\,\Omega}{P_a}\left(\frac{R}{C}\right)^2$.

Table 9 Geometry for analysis of gas bearing performance

Physical Properties	*Value*
Bearing Material	Aluminum
Bearing Diameter (mm)	29.5
Axial Bearing Length (mm)	30.0
Number of Lobes in Bearing Circumference	3
Lobe Length (degrees)	120
Nominal Clearance (μm)	66
Dimensionless Preload*	0.346
Lobe Offset	0.5
Feed Orifice Diameter (mm)	1.0
Number of Feed Orifices (sources)	3
Number of Nodes [θ, Z]	91, 11
Location of Source 1 [θ, Z]	[16, 3]
Location of Source 2 [θ, Z]	[46, 3]
Location of Source 3 [θ, Z]	[76, 3]

*Appendix B gives the definition for calculating preload.

Table 10 Operating conditions for analysis of gas bearing performance

Operating Condition	*Value*
Ambient Pressure	1.01E5
Temperature (K)	299.8
Viscosity (Pa-sec)	1.87E-5
Density at Ambient Pressure (kg/m^3)	1.224

The test rotor weighs 0.827 kg, so a static load equal to half the weight of the rotor is applied in the X direction to the bearing (F_x equal to 4.056 N, F_y equal to 0). Since bearing performance predictions are highly dependent on the curtain area pressure (as function of feed orifice diameter), an empirical adjustment is made to the source supply pressure accounting for the flow resistance through the feed orifice to determine the actual pressure (P_s) at the entrance of the feed orifice. The mass flow rate at the desired test supply pressure (determined from the curve of mass flow rate

versus supply pressure with the rotor installed in the bearings[17]) is matched to the mass flow rate on the curve without the rotor installed in the bearings. The corresponding pressure at the newly identified mass flow rate becomes the 'adjusted' supply pressure.

Referring to the nomenclature presented in Fig. 7, the model uses 91 circumferential nodes and 11 axial nodes to analyze half the bearing geometry (since the bearing is axially symmetric about the circumferential axis). The feed orifices are located at the nodes representing the appropriate physical location. The equilibrium and perturbed pressure fields are numerically iterated until a convergence tolerance limit of 10^{-5} is satisfied (with a maximum of 599 iterations). The program predicts the static and dynamic bearing force coefficients for a range of feed supply pressures and operating speeds.

Overall, the predictions show increasing orifice pressures and mass flow rates for increasing supply pressures. Force coefficients show a strong dependency on excitation frequency, although the dependence is most significant at frequency ratios larger than 1.0 (above the range of interest with respect to whirl frequency ratios experienced when the rotor/bearing system becomes unstable). Individual operating parameters, such as journal eccentricity and altitude angle, are examined below.

Journal Eccentricity and Altitude Angle

Fig. 25 displays the predicted journal eccentricity at low rotor speeds (effectively equal to zero rpm) as a function of nominal clearance[18]. The rotor actually rests at bottom of the bearings (eccentricity equal to the clearance) until hydrostatic feed is applied to lift and support the rotor on a gas film. As the hydrostatic feed is increased, the rotor approaches the centered position (zero eccentricity). X-direction eccentricity (direction of applied static load) is as large as 42 percent of the nominal

---

[17]Appendix D gives the curves of measured mass flow rates versus measured supply pressures, with and without the rotor installed.

[18] Due to the preload of the lobes, the minimum radial film thickness is 44 μm.

clearance for small pressure ratios (approximately equal to 1.34) and decreases to less than 5 percent for supply pressure ratios equal to 5.08. Predictions for the film pressure field in do not easily converge for pressure ratios equal to 1.27 and below[19].

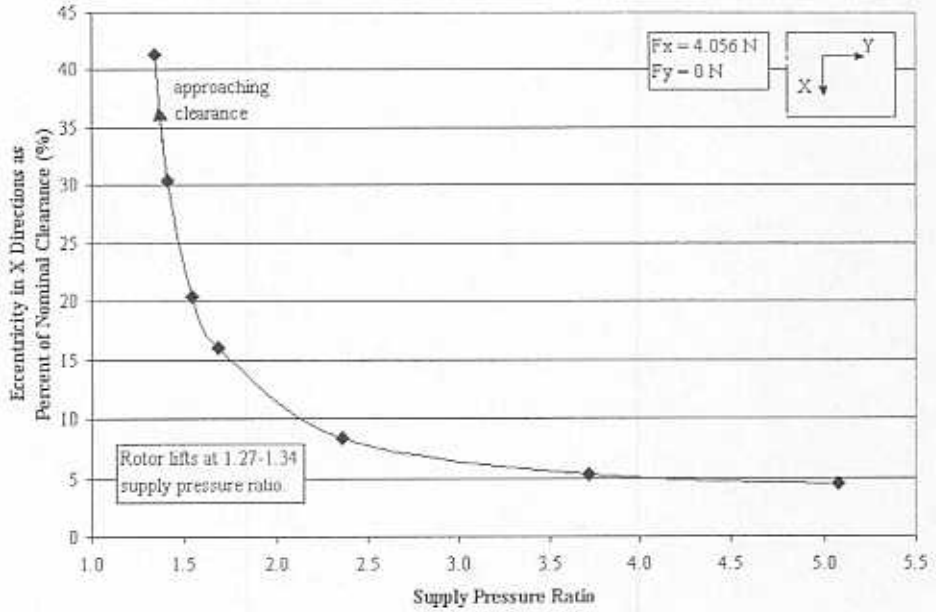

Fig. 25 Predicted static journal eccentricity as a percent of nominal clearance

Fig. 26 shows the predicted low-speed (effectively zero rpm) journal eccentricity in the *X* and *Y* directions (shown with respect to the nominal clearance) for increasing pressure ratios, indicating increasing rotor lift due to the hydrostatic feed and initial operation at the nearly centered position for higher supply pressures.

[19] Feed pressure for rotor lift off is previously identified as pressure ratios equal to 1.27-1.34.

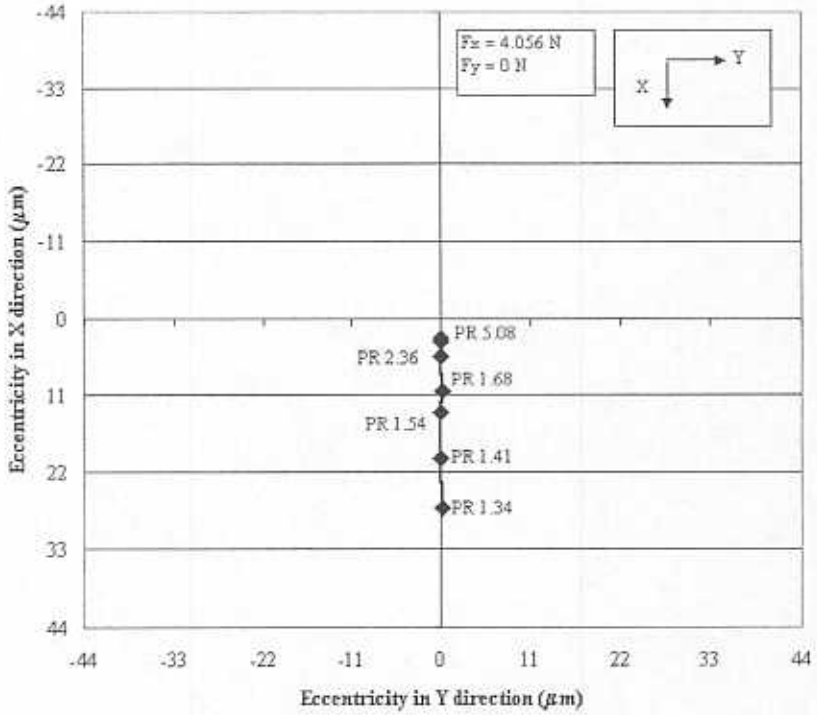

Fig. 26 Predicted static journal eccentricity for increasing pressure ratios (PR), minimum film thickness equal to 44 μm

The journal eccentricity, (*e*), and attitude angle, (φ), give useful information about the stability of the system. The attitude angle is defined as the angle between the direction of static load and the eccentricity vector. Fig. 27 depicts the predicted journal attitude angle for increasing supply pressure ratios. The attitude angle approaches 90 degrees at lower supply pressures, favoring hydrodynamic instability. At higher supply pressures, the attitude angle increases at a much slower rate, and therefore favors rotor/bearing stability.

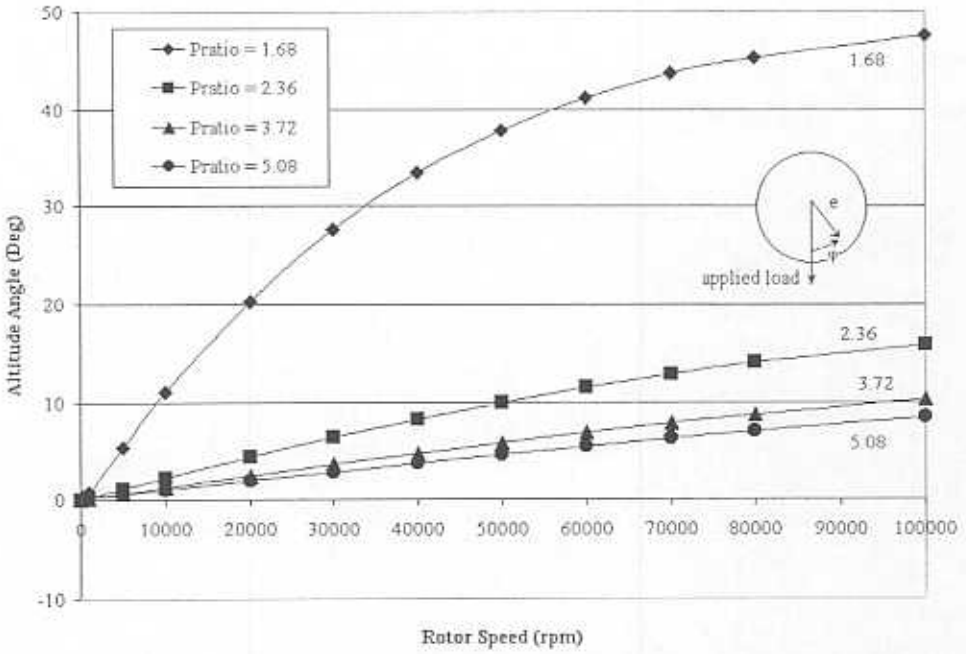

Fig. 27 Predicted journal attitude angle versus rotor speed for increasing pressure ratios

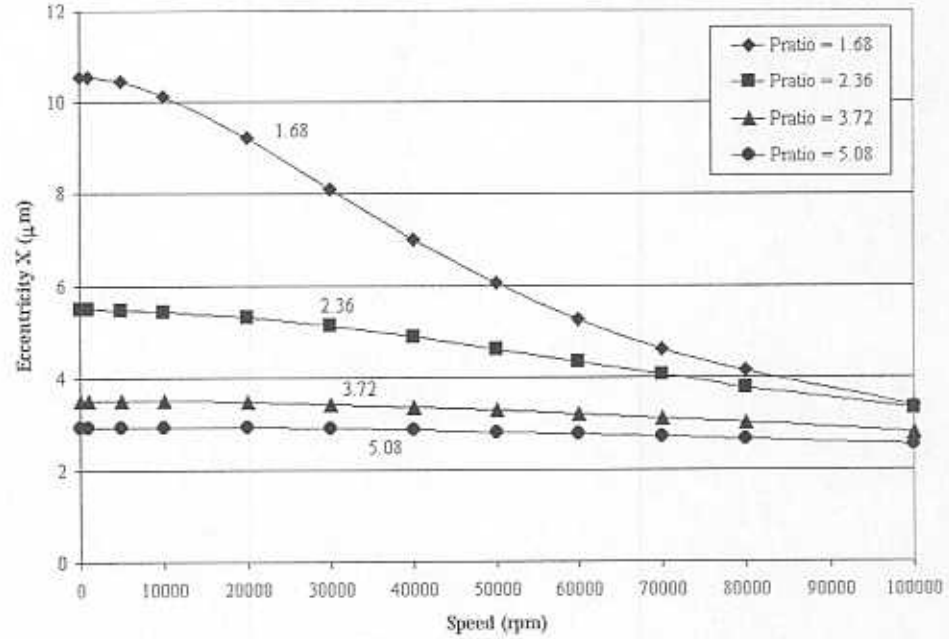

Fig. 28 Predicted journal eccentricity versus rotor speed for increasing pressure ratios

Fig. 28 shows the predicted journal eccentricity in the X direction for increasing supply pressure, with values decreasing towards the centered position for increasing speed. Journal eccentricity is nearly constant at higher supply pressure ratios (equal to 3.72 and above). The predicted rotor eccentricity matches the test response well. For example, the experimental response (taken from journal centerline plots) indicates the rotor operates at an eccentricity on the order of 5.0 μm to 2.5 μm depending on supply pressure and speed. Considering the nominal clearance of 66 μm, the eccentricity ranges from 5.28 μm at pressure ratio equal to 2.36 and low rotor speed to 2.64 μm at pressure ratio equal to 5.08 and high rotor speed.

Fig. 29 shows the predicted journal eccentricity and attitude angle for speeds up to 100,000 rpm. Note that journal eccentricities are much smaller (by a factor of 4-10 depending on supply pressure) than the minimum film thickness (44 μm). A reference to the rotor/bearing clearance is not included in Fig. 29 since eccentricity values are so small. The locus plot indicates that the lightly loaded, high-speed rotor approaches the centered position where the journal eccentricity vector is nearly orthogonal to the load vector. This is a situation that promotes rotordynamic instability.

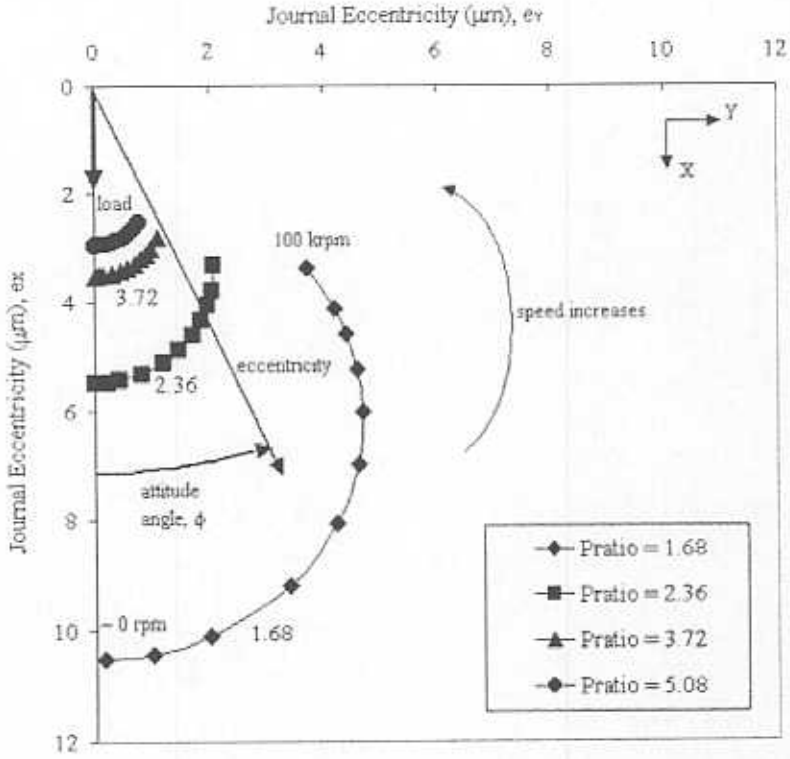

Fig. 29 Predicted loci of journal center for increasing supply pressures and rotor speeds

Predicted Bearing Force Coefficients

Fig. 30 through Fig. 37 give the predicted stiffness and damping (direct and cross-coupled) force coefficients as a function of frequency ratio (ratio of excitation frequency to journal operating frequency) at pressure ratio equal to 5.08 and three rotor speeds[20]. The figures indicate that the bearing force coefficients are not largely frequency dependent within the subsynchronous region (the frequency ratio region where the rotor/bearing system is expected to become unstable). At higher speeds the coefficients become more dependent on frequency, but this region is above the frequency ratio range causing instability in the bearings. For reference, Appendix H

---

[20] Low rotor speed is equal to 20,000 rpm, medium rotor speed equal to 40,000 rpm, and high rotor speed equal to 100,000 rpm.

contains a tabular list of the dimensional force coefficients at a pressure ratio equal to 5.08.

As shown in Fig. 30 and Fig. 31, the predicted direct stiffness force coefficients increase with increasing speed and increasing frequency ratio (FR). Values of K_{xx} approximately equal the values of K_{yy} for the entire frequency ratio range. The frequency dependence becomes apparent for frequency ratios ranging from 1.0-100, with values being nearly constant below FR equal to 1.0 (approximately 1.75E6 N/m). Magnitudes of direct stiffness force coefficients approach 4.3 MN/m at a FR equal to 100.

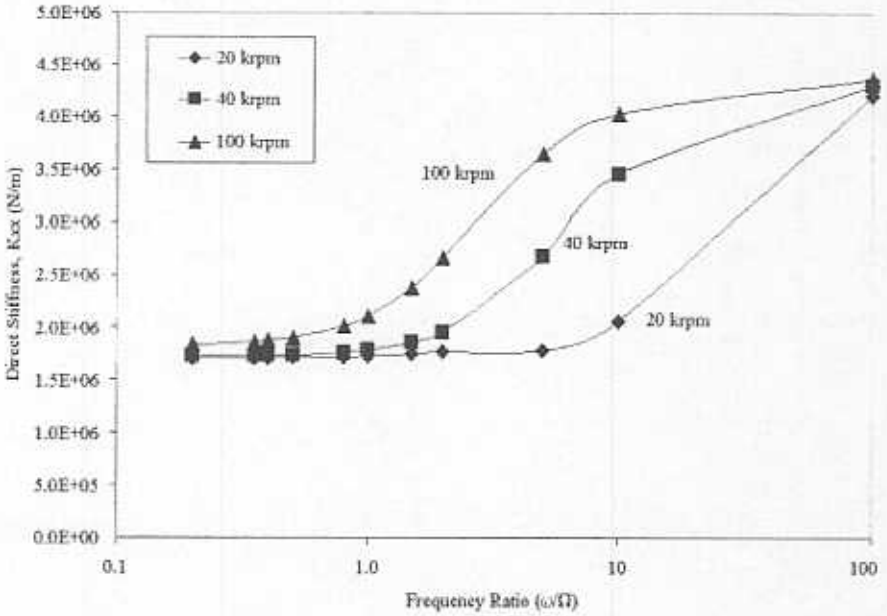

Fig. 30 Predicted three lobe bearing direct stiffness force coefficients (*Kxx*) at pressure ratio equal to 5.08 and three rotor speeds

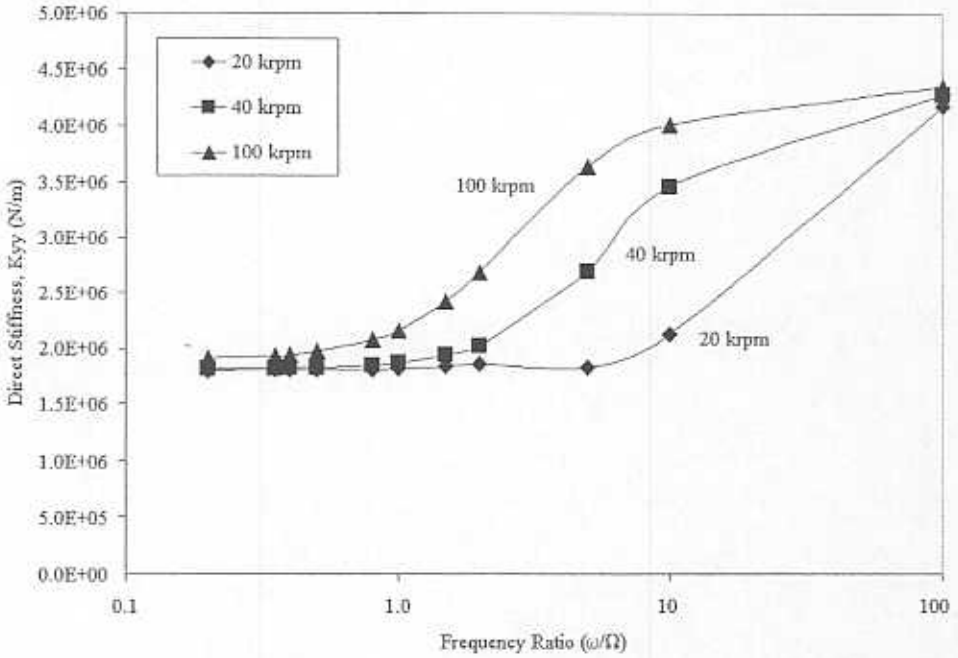

Fig. 31 Predicted three lobe bearing direct stiffness force coefficients (*Kyy*) at pressure ratio equal to 5.08 and three rotor speeds

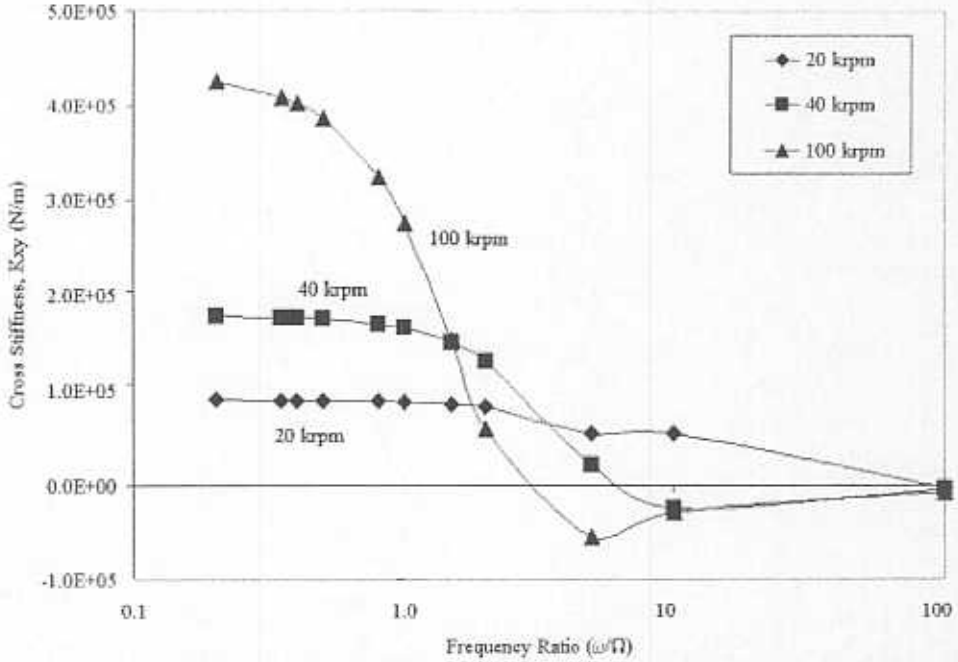

Fig. 32 Predicted three lobe bearing cross-coupled stiffness force coefficients (*Kxy*) at pressure ratio equal to 5.08 and three rotor speeds

The values of predicted cross-coupled stiffness force coefficients, shown in Fig. 32 and Fig. 33, are nearly constant at low frequency ratios for the low and medium speeds (magnitudes increasing with speed). At high rotor speed, the magnitudes decrease between FR equal to 1.0 and 10. Values of K_{xy} approximately equal the values of $-K_{yx}$ for the entire FR range. A significant decrease in magnitude occurs for FR ramping from 1.0-10, with the magnitudes decreasing more quickly for higher rotor speeds. Cross-coupled stiffness coefficients approach null values at FR equal to 100 for all rotor speeds. Large values of subsynchronous cross-coupled stiffness force coefficients encourage hydrodynamic instability.

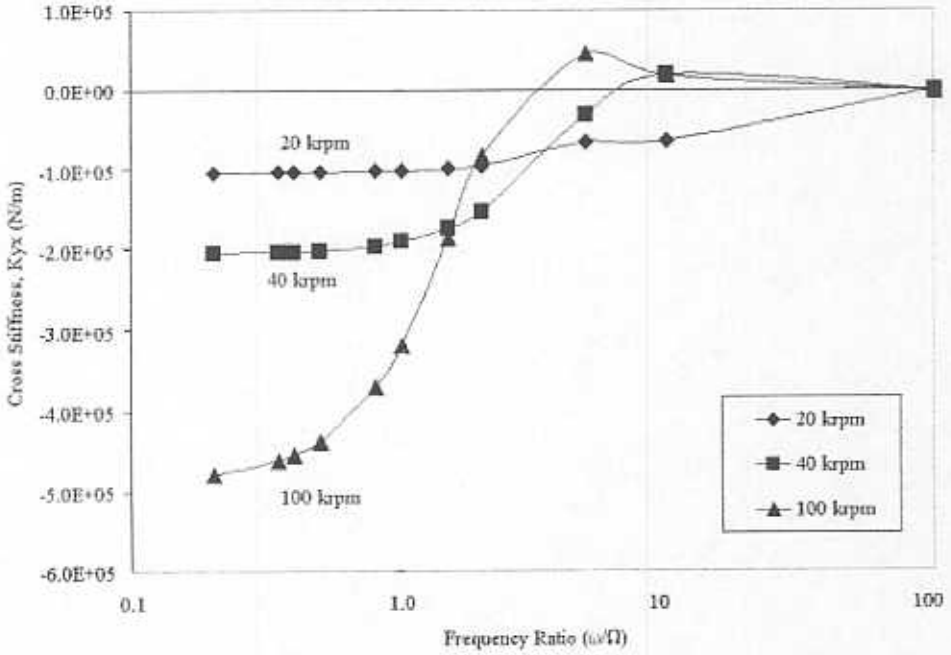

Fig. 33 Predicted three lobe bearing cross-coupled stiffness force coefficients (*Kyx*) at supply pressure ratio equal to 5.08 and three rotor speeds

Fig. 34 and Fig. 35 show magnitudes of predicted direct damping force coefficients, where values of C_{xx} approximately equal the values of C_{yy}. Direct damping at low and mid rotor speeds is nearly constant (around 90 Ns/m) for frequency ratios below 1.0, while the direct damping at high rotor speed decreases

slightly through the frequency range (from approximately 80 Ns/m to approximately 70 Ns/m). Magnitudes drop considerably in the range of FRs between 1.0 to 10, going to zero at FR equal to 100. Large values of direct damping force coefficients promote stable behavior.

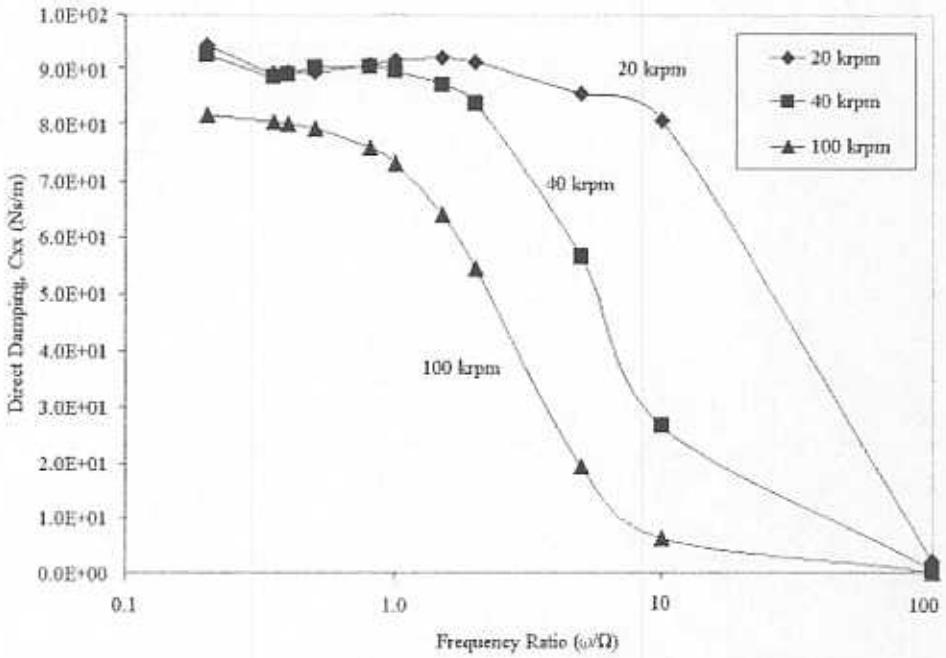

Fig. 34 Predicted three lobe bearing direct damping force coefficients (*Cxx*) at pressure ratio equal to 5.08 and three rotor speeds

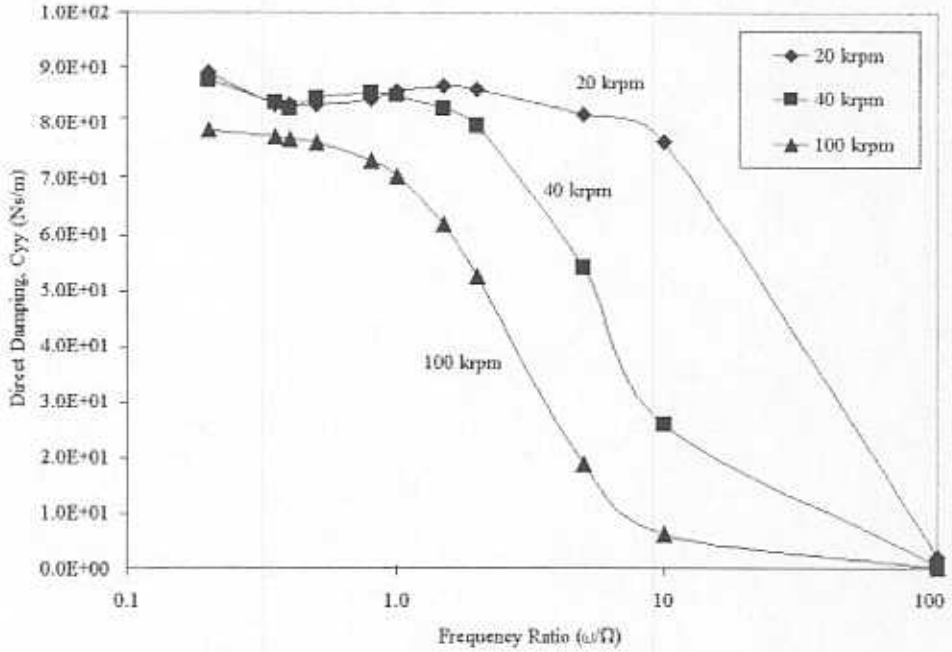

Fig. 35 Predicted three lobe bearing direct damping force coefficients (*Cyy*) at pressure ratio equal to 5.08 and three rotor speeds

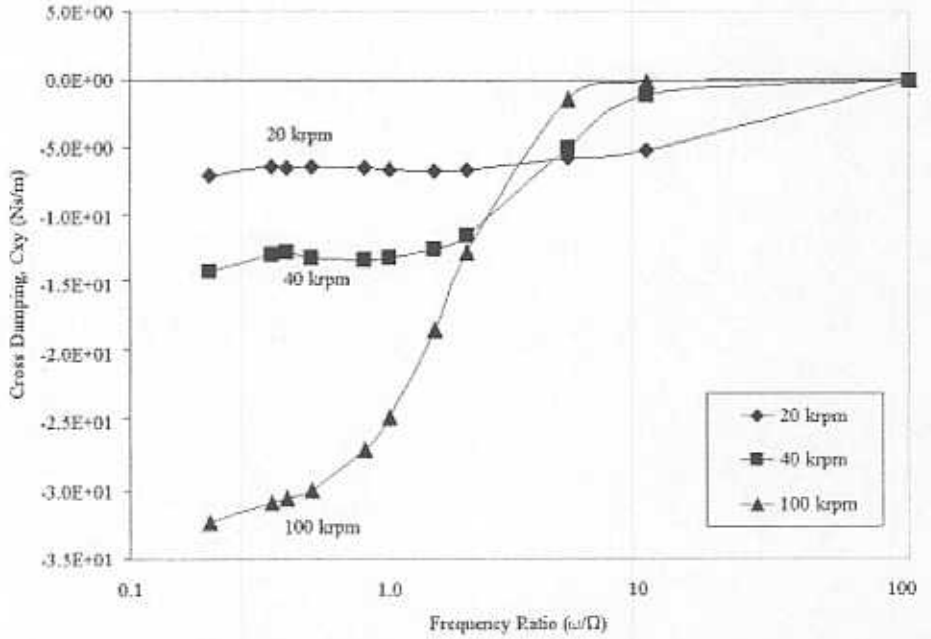

Fig. 36 Predicted three lobe bearing cross-coupled damping force coefficients (*Cxy*) at pressure ratio equal to 5.08 and three rotor speeds

Predicted cross-coupled damping force coefficients are given in Fig. 36 and Fig. 37 where magnitudes of C_{yx} approximately equal the values of $-C_{xy}$. Magnitudes increase with journal speed at low frequency ratios and remain nearly constant at low and medium rotor speeds. Values at large rotor speeds decrease at a faster rate for FRs between 1.0 and 10, with null magnitudes at FR equal to 100.

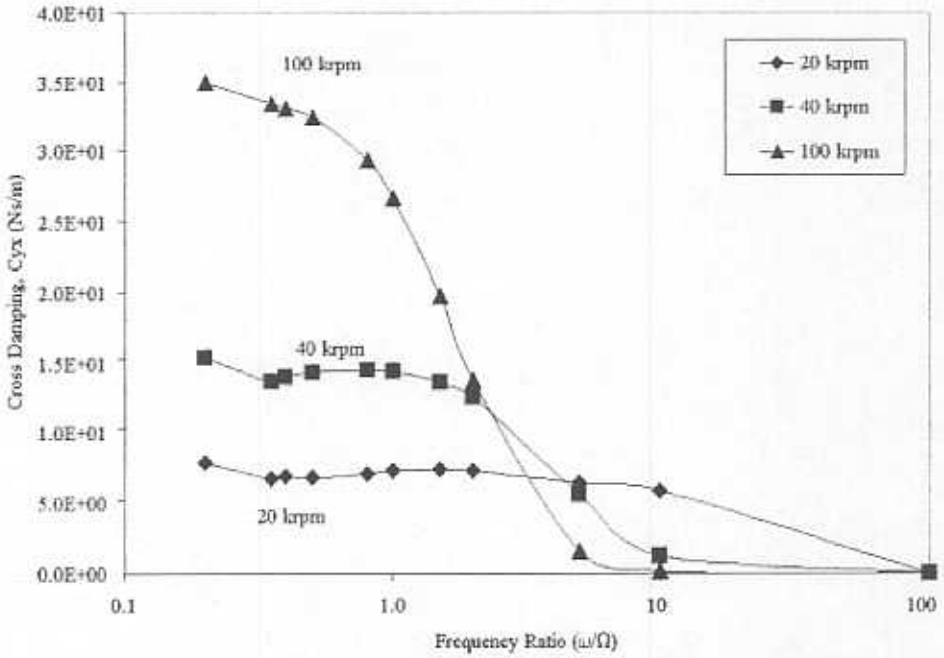

Fig. 37 Predicted three lobe bearing cross-coupled damping force coefficients (*Cyx*) at supply pressure ratio equal to 5.08 and three rotor speeds

For pressure ratio equal to 5.08, experimental results show the system becomes unstable around 80 krpm, which is explained by observing changes in the predicted force coefficients between 40 krpm and 100 krpm. The direct stiffness and cross-coupled damping increase, while the direct damping and cross-coupled stiffness decrease. For larger rotor speeds, the equivalent system stiffness[21] increases and the

---

[21] Equivalent system stiffness is defined as: $K_{x_{eq}} = K_{xx} + C_{xy}\omega$ and $K_{y_{eq}} = K_{yy} + C_{yx}\omega$. Equivalent system damping is defined as: $C_{x_{eq}} = C_{xx} + K_{xy}/\omega$ and $C_{y_{eq}} = C_{yy} + K_{yx}/\omega$.

equivalent system damping decreases, possibly leading to hydrodynamic whirl instability. Values of cross-coupled stiffness and damping components are of nearly equal magnitude having opposite sign, a telltale feature of destabilizing systems.

Predicted Rotor/Bearing System Performance

Modeling the rotor/bearing system using XLTRC^2 Software Suite predicts the response to imbalance, natural frequencies, and damping ratios, allowing further analysis of the response performance and stability characteristics (namely threshold speeds of instability and whirl frequency ratios). A rotor model, made up of elasto-massic stations, describes the test rotor. The bearings are applied at the bearing support locations by linking the synchronous (frequency ratio equal to 1.0) gas bearing force coefficients corresponding to a specific supply pressure.

Rotor Model: Free-free Mode Natural Frequencies and Shapes

Fig. 38 shows the multiple station model of the rotor. Physically, the motor is press-fit onto the inner shaft first, and then the outer sleeves are press-fit onto the ends of the shaft. In the journal model, a bi-layer single shaft represents the rotor where vertical lines divide the rotor into nineteen stations. Different shades indicate differently material properties. Stations 7-8 and 12-13 indicate small gaps between the outer sleeves and the motor (these gaps exist physically as well). The support bearings are added at the appropriate physical locations.

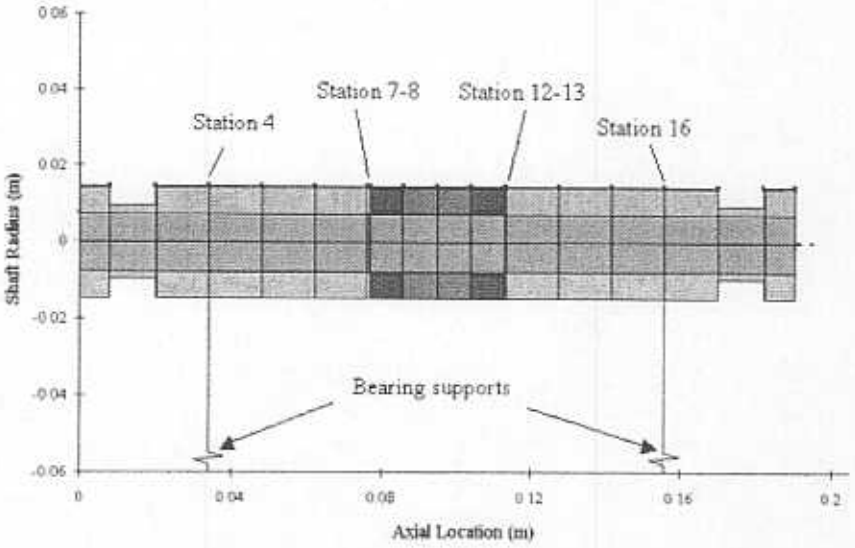

Fig. 38 Geometric model of the test rotor for analysis with XLTRC[2]

Adjusting the motor materials and spacing at the sleeves until the first and second free-free predicted modes shapes match the corresponding experimentally measured (by rap test[22]) mode shapes, displayed in Fig. 39 and Fig. 40, calibrates the model. The first mode shape (at 1820 Hz) indicates that the press fit motor stiffens the shaft at the center section of the rotor and that maximum deflection occurs at the rotor ends. The second mode shape (at 5900 Hz) confirms the motor stiffening effect with nearly constant slope within the region of the motor. The maximum bending occurs at the gaps between the motor and the press-fit sleeves

[22] The rap test consists of suspending the rotor, rapping the rotor with an impact hammer, and obtaining the amplitude of the transfer function measured between a stationary and a roaming accelerometer versus the rotor axial length.

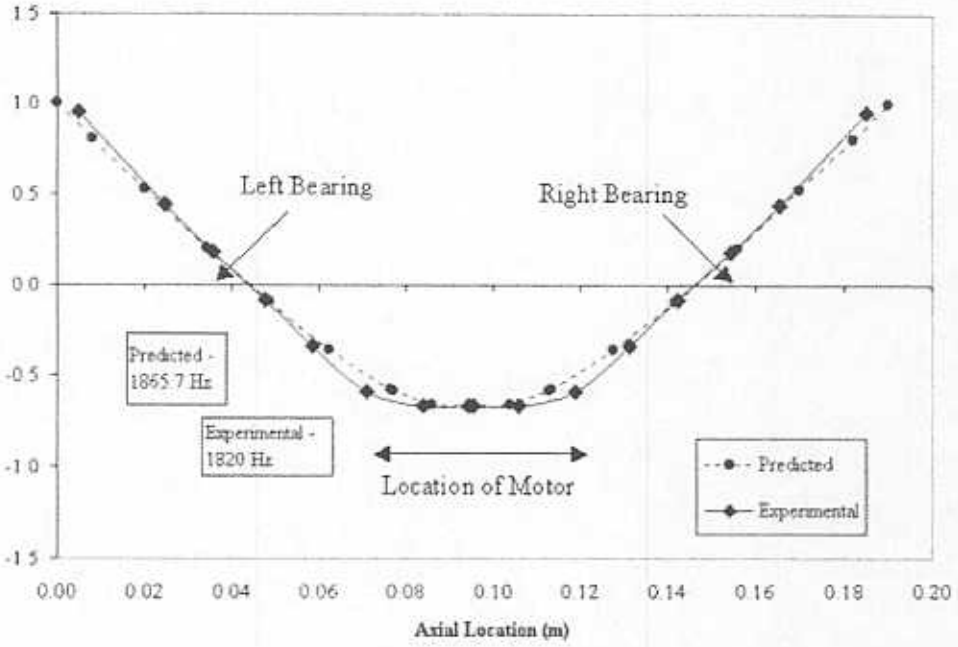

Fig. 39 Measured and predicted first free-free mode shape of the test rotor

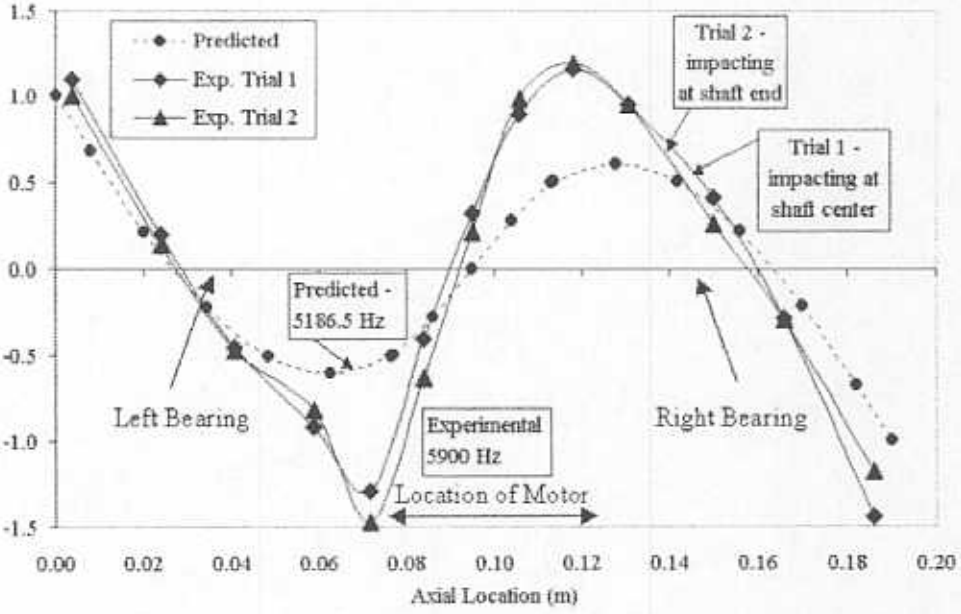

Fig. 40 Measured and predicted second free-free mode shape of the test rotor

Table 11 gives the experimental and predicted (using the XLTRC^2 rotor model) first and second natural frequencies of the test rotor. Appendix H contains the physical model for the test rotor.

Table 11 Free-free natural frequencies of test rotor

Free-free Natural Frequencies	*Measurement, rpm (Hz)*	*Predictions, rpm (Hz)*	*% Difference*
1st bending mode	109,200 (1820)	111,942 (1866)	2.4 %
2nd bending mode	354,000 (5900)	311,190 (5187)	13.8 %

Damped Eigenanalysis, Response to Imbalance, and Damping Ratios

An eigenanalysis delivers the rotor/bearing natural frequencies and damping ratios. In addition, the imbalance response of the rotor supported on the bearings (synchronous force coefficients) is predicted. Subsequent evaluation of the synchronous imbalance response eigenvalues evidences threshold speeds and whirl frequency ratios. Predicted results are compared to the experimental responses at similar supply pressure ratios. The analysis begins by evaluating the system performance with the rotor supported on synchronous bearing force coefficients.

Fig. 41 and Fig. 42 show the synchronous bearing force coefficients at a pressure ratio equal to 5.08[23]. At high rotor speeds, all stiffness force coefficients increase while the damping force coefficients decrease. Cross-coupled stiffness and damping force coefficients are of equal magnitude and opposite sign, with magnitudes lower than those of the direct force coefficients. These coefficient characteristics show destabilizing behavior and may eventually lead to rotordynamic instability.

[23] These are the same coefficients detailed in the "Predicted Bearing Force Coefficients" section as a function of operating rotor speed instead of frequency ratio.

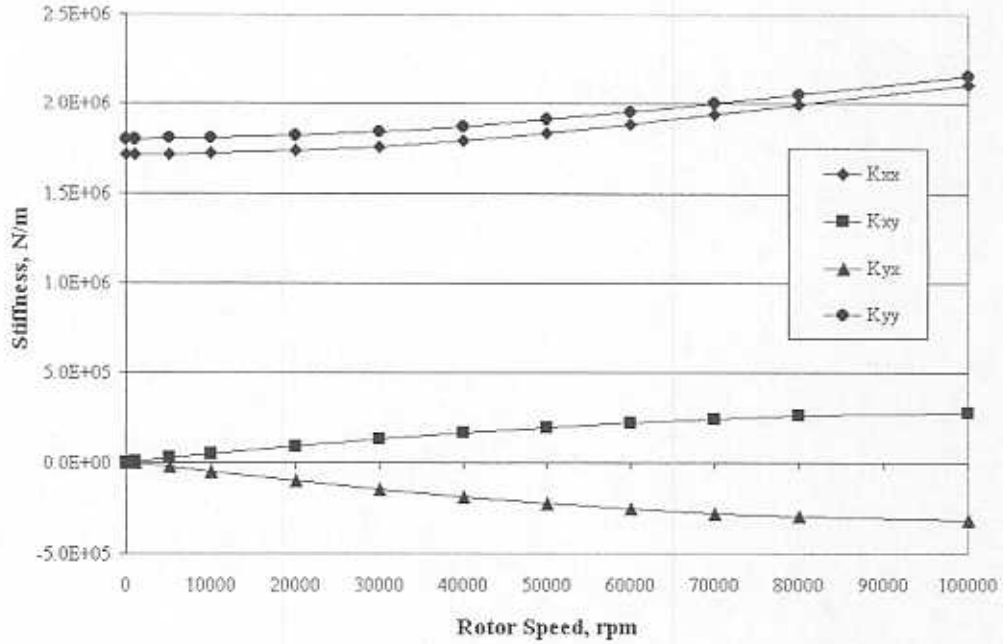

Fig. 41 Predicted synchronous three lobe bearing stiffness force coefficients at pressure ratio equal to 5.08

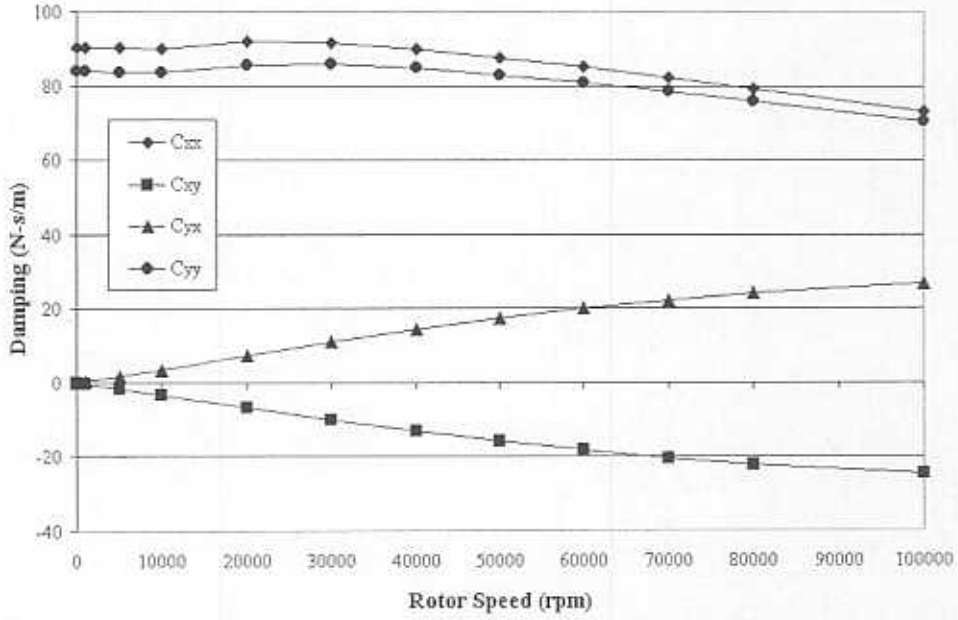

Fig. 42 Predicted synchronous three lobe bearing damping force coefficients at pressure ratio equal to 5.08

Fig. 43 depicts the predicted rotor imbalance response at the test rotor ends. The imbalance masses used for prediction (1.00E-3 kg-m) are on the same order of magnitude, and at the same physical location, as those applied experimentally (1.06E-3 kg-m for *U1* and 7.92E-4 kg-m for *U2*). Note that the predicted response is identical at the left and right support bearings since the rotor model and imbalance distribution are symmetric. Overall, the predicted response matches well with the experimental response at the location of the right bearing vertical eddy current sensor (refer to Fig. 11), although displacement amplitudes are increased due to larger imbalance in the rotor model. Experimental responses at other eddy current sensor locations differ from the predicted response due to uneven (non-symmetric) remnant imbalance.

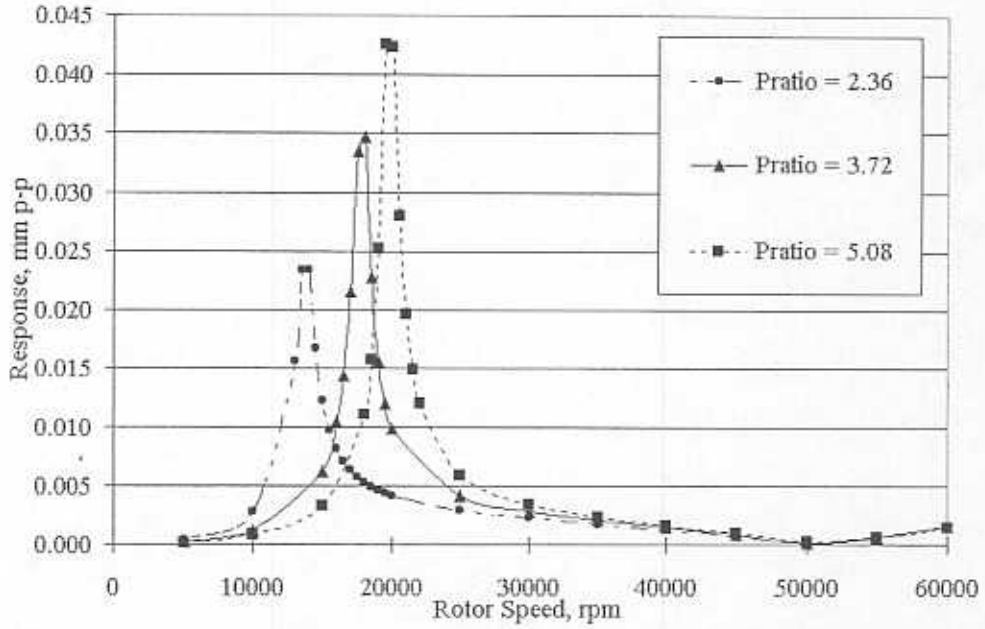

Fig. 43 Predicted imbalance response (peak to peak) for rotor supported on synchronous bearing force coefficients for increasing supply pressure ratios

The eigenanalysis is performed over a speed range of 5000-120,000 rpm with the forward conical and cylindrical modes becoming unstable (being forced by the forward motion of the rotor imbalance). Note that the predicted response to imbalance

is therefore only reasonable while the rotor/bearing system is in the stable condition, i.e. at speeds below the threshold of instability.

Eigenvalues are identified when the frequency of the predicted mode at a particular operating speed matches the frequency corresponding to the one from the supporting bearing coefficients. For example, with the rotor supported on the synchronous bearing force coefficients the eigenvalue is determined at the speed when the frequency of the mode matches the operating speed with a 1 to 1 ratio. Table 12 summarizes the predicted natural frequencies and damping ratios (identified as the real part of the eigenvalue) for the rotor supported on synchronous bearing force coefficients at pressure ratio equal to 5.08. Note that the natural frequencies of the conical and cylindrical modes are close in magnitude.

Table 12 Synchronous eigenvalues and damping ratios for rotor supported on synchronous bearing force coefficients at various pressure ratio

Pressure Ratio	*Conical Mode Natural Frequency (rpm)*	*Conical Mode Damping Ratio*	*Cylindrical Mode Natural Frequency (rpm)*	*Cylindrical Mode Damping Ratio*
5.08	19,680	0.027	21,381	0.029
3.72	17,813	0.035	19,378	0.038
2.36	13,675	0.047	14,862	0.049

Fig. 44 compares the predicted forward conical and cylindrical synchronous natural frequencies to the critical speeds determined from the experimental coast down remnant imbalance responses at the vertical sensor for each bearing. The figure shows excellent agreement and indicates a certain amount of gyroscopic influence (in the experimental response) since the experimental values increase slightly above the predicted values at higher supply pressures.

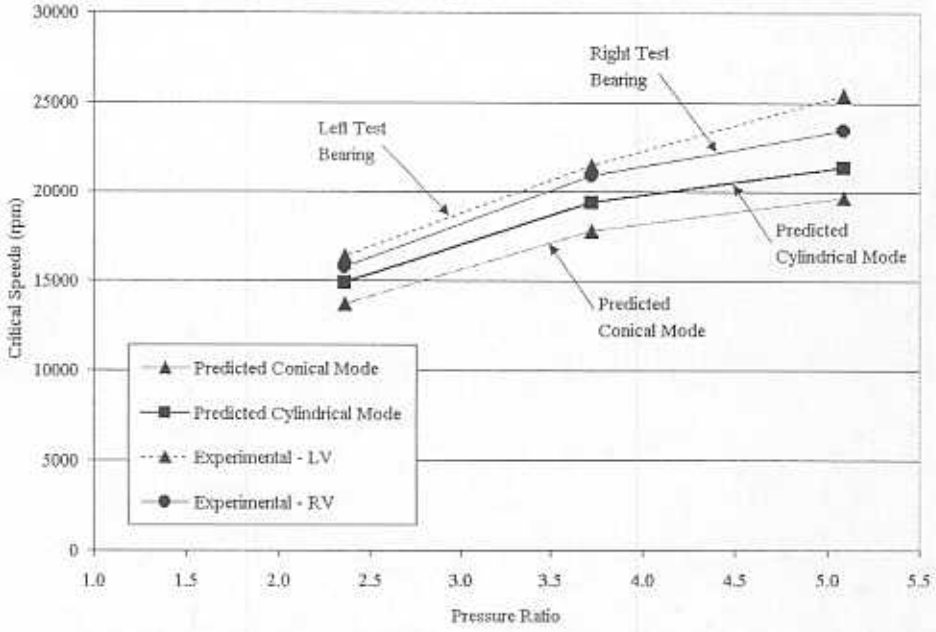

Fig. 44 Predicted critical speeds for imbalance response with rotor supported on synchronous bearing force coefficients and experimental critical speeds from remnant imbalance synchronous coastdown response (pressure ratio equal to 5.08)

Fig. 45 compares the predicted and experimental damping ratios. The predicted values are determined from the imbalance response with the rotor supported on synchronous bearing force coefficients at pressure ratio equal to 5.08. Experimental values are determined by the Q factor method from the synchronous rotor remnant imbalance response (pressure ratio equal to 5.08). The damping ratios from the predicted responses range between 2.7 percent and 4.9 percent, while damping ratios from the experimental responses range between 7.1 percent and 12.4 percent. Note that experimental imbalance levels are slightly lower than those used in the predictions. Even so, the damping ratios from the predicted responses are considerably lower than those from the experimental responses.

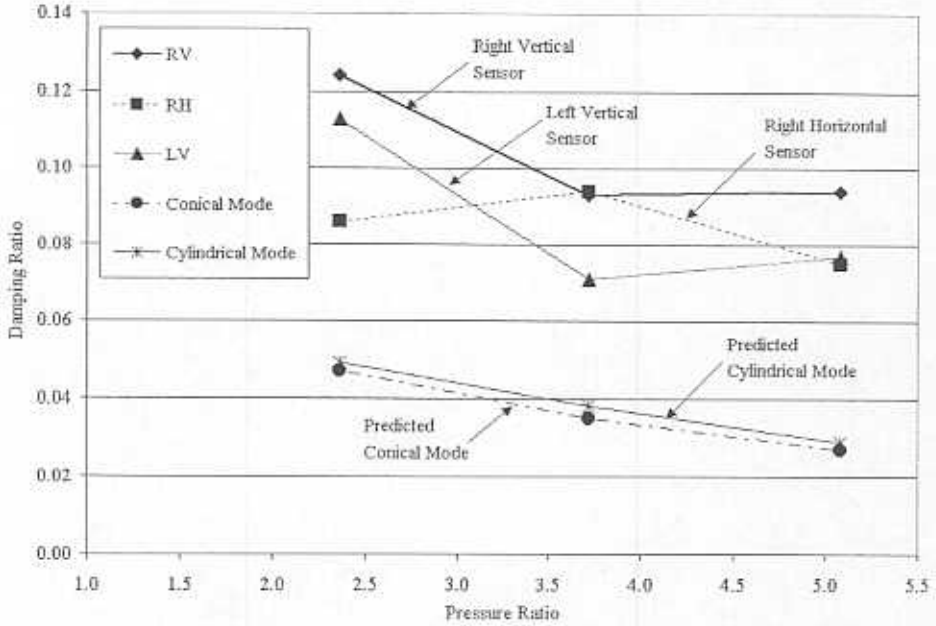

Fig. 45 Predicted conical and cylindrical mode damping ratios for imbalance response with rotor supported on synchronous bearing force coefficients and experimental damping ratios from synchronous remnant imbalance rotor response

Threshold Speeds of Instability

A rotor/bearing system mode becomes unstable when the corresponding damping ratio changes from a positive to negative value, going through zero at a given rotor speed. The whirl frequency ratio is determined as the ratio of this threshold frequency to operating speed. Once identifying the whirl frequency ratio at the threshold, the performance is further investigated using the predicted bearing force coefficients at that identified frequency ratio.

Returning to the example for the rotor supported on the synchronous force coefficients with pressure ratio equal to 5.08, the bearing becomes unstable as anticipated from the experimental results. The threshold speeds of instability for the forward conical and cylindrical modes occur at 42,000 rpm and 45,000 rpm, respectively. Dividing the frequency of the mode at the threshold by that identified rotor speed gives the whirl frequency ratio at the threshold.

The predicted whirl frequency is similar to the experimental results, but the threshold speed is much lower, therefore giving significantly higher whirl frequency ratios than the experimental findings. For convenience, Table 13 highlights the experimentally determined threshold speeds, whirl frequencies, and whirl frequency ratios for varying pressure ratios.

Table 13 Experimental threshold speeds, whirl frequencies, and whirl frequency ratios from the synchronous remnant imbalance rotor response supported on three lobe bearings

Supply Pressure Ratio	Threshold Speed (rpm)	Whirl Frequency (rpm)	Whirl Frequency Ratio
5.08	85,184	21,600	0.25
3.72	54,960	19,440	0.35
2.36	37,200	13,680	0.4

Table 14 gives the predicted synchronous threshold speeds, whirl frequencies, and whirl frequency ratios for the three supply pressure ratios[24]. The predicted whirl frequency ratios fall between 0.41 and 0.49 for all supply pressures. Therefore, the performance of the rotor supported on 0.4X frequency ratio bearing force coefficients was investigated further (at all three supply pressures). Table 15 gives the 0.4X subsynchronous threshold speeds, whirl frequencies, and whirl frequency ratios.

---

[24] The bearing force coefficients were originally evaluated for eight frequency ratios at each supply pressure ratio (0.2, 0.35, 0.4, 0.5, 0.8, 1.0, 1.5, and 2.0). Force coefficients evaluated at these frequency ratios were used during subsequent subsynchronous force coefficient investigation since the frequency dependence is not strong within the subsynchronous frequency range of interest.

Table 14 Predicted instability from rotor imbalance response with synchronous (1X) bearing force coefficients at increasing pressure ratios

Supply Pressure Ratio	Forward Conical			Forward Cylindrical		
	Threshold Speed (rpm)	Whirl Frequency (rpm)	Whirl Frequency Ratio	Threshold Speed (rpm)	Whirl Frequency (rpm)	Whirl Frequency Ratio
2.36	28,460	14,010	0.49	30,770	15,020	0.49
3.72	45,000	18,410	0.41	47,500	19,610	0.41
5.08	42,000	19,950	0.48	45,000	21,350	0.47

Table 15 Predicted instability from rotor imbalance response with 0.4X subsynchronous bearing force coefficients at increasing pressure ratios

Supply Pressure Ratio	Forward Conical			Forward Cylindrical		
	Threshold Speed (rpm)	Whirl Frequency (rpm)	Whirl Frequency Ratio	Threshold Speed (rpm)	Whirl Frequency (rpm)	Whirl Frequency Ratio
2.36	26,760	13,660	0.51	28,610	14,610	0.51
3.72	34,440	17,710	0.51	37,220	18,960	0.51
5.08	38,570	19,640	0.51	40,710	21,030	0.52

The identified whirl frequency ratios with the rotor supported on 0.4X subsynchronous bearing coefficients are 0.51-0.52 (much higher than found experimentally). Again, the threshold speeds are much lower than experimental results leading to higher threshold whirl frequency ratios.

Predictions of damped eigenvalues were also performed with the rotor supported on 0.2X bearing force coefficients for pressure ratio equal to 5.08 (0.2X is closer to the experimental WFR 0.25). Threshold WFRs are found to be 0.5X. Table 16 summarizes the analysis at pressure ratio equal to 5.08 indicating nearly identical predicted performance for synchronous and subsynchronous bearing coefficients.

Table 16 Predicted rotor imbalance response with various frequency ratio bearing force coefficients at pressure ratio equal to 5.08

Frequency Ratio	Forward Conical			Forward Cylindrical		
	Threshold Speed (rpm)	Whirl Frequency (rpm)	Whirl Frequency Ratio	Threshold Speed (rpm)	Whirl Frequency (rpm)	Whirl Frequency Ratio
1.0X	42,000	19,950	0.475	45,000	21,350	0.474
0.4X	38,570	19,640	0.509	40,710	21,030	0.517
0.2X	39,290	19,580	0.498	42,140	20,940	0.497

Closure for Rotordynamic Response Predictions

An empirical adjustment made to the supply pressure into the bearing model accounts for the flow resistance through the feed orifices. The ideal gas Reynolds equation is solved used finite elements to predict pressure fields in the gas bearing film. Bearing static performance parameters and dynamic force coefficients are forwarded from the predicted pressure fields. Journal eccentricities match well with experimental results.

After calibration of the rotor model free-free modes and linking the predicted synchronous bearing coefficients at the appropriate rotor locations, the rotor bearing system performance is predicted. A damped eigenanalysis predicts the synchronous natural frequencies, which correspond well with experimental critical speeds. The predictions indicate that rotor excitation due to imbalance is a combination of the conical and cylindrical modes, since these two modes have natural frequencies quite close in magnitude. The predicted response to imbalance displays similar behavior as some of the experimentally measured coastdown responses. On the other hand, the model predicts much lower threshold speeds of instability than measured, and therefore predicted whirl frequency ratios tend to be higher than the experimental values. Predicted damping ratios are also lower than the damping ratios determined from

experimental response. The damping ratio is directly related to system damping and indirectly related to the system natural frequency (a function of system stiffness and mass). Since the rotor mass and critical speeds are predicted well, this leads to poorly predicted overall system damping, low threshold speeds of instability, and high whirl frequency ratios.

For this particular hybrid gas bearing configuration, predicted bearing force coefficients show a strong dependence on frequency ratio at supersynchronous frequency excitation. Iterations to predict threshold whirl frequency ratios are not greatly affected by the frequency ratio of the supporting bearing force coefficients or by supply pressure ratio.

EXPERIMENTAL DYNAMIC PERFORMANCE OF ROTOR SUPPORTED ON OTHER BEARING CONFIGURATIONS

In addition to the tests with three lobe bearings, experimental responses of several other bearing geometries have been collected. Geometries include a hybrid pressure dam three-lobe bearing (the original and one design modification) and one type of hybrid tilting pad bearing. Analysis of coastdown responses, critical speeds, threshold speeds of instability, overall damping ratios, and feed pressures for rotor lift-off defines the performance of each bearing configuration.

Three-Lobe Pressure Dam Hybrid Bearing

Appendix C contains the complete description of the original and the modified pressure dam bearing geometries. The anti-vibration blocks (as detailed in Appendix C) are at both ends of the test chamber for the tests with the modified pressure dam bearings only.

Coast Down Tests to Calibrated Imbalance: Rotor Supported on Original Pressure Dam Bearings

Coastdown tests to capture the response to calibrated imbalance masses were conducted in a similar fashion to the tests conducted with the rotor supported on three lobe bearings. Tests include the response to remnant imbalance, and two calibrated imbalances, *U1* and *U2*, where *U1>U2*. Unfortunately, the original pressure dam bearings evidenced significant pneumatic hammer when hydrostatically supported (showing a dependence on pressure ratio), making it almost impossible to characterize any other performance criterion of the rotor/bearing system.

The hammer occurred during coast down tests, evidenced by fixed supersynchronous and/or subsynchronous frequency vibration. The waterfall plot in Fig. 46 shows one typical example of the pneumatic instability for pressure ratio equal to 3.04. A fixed frequency component appears at 385 Hz and small amplitudes at two

times this (770 Hz). The fixed frequency component at 385 Hz is larger in magnitude than the synchronous components and contributes to significantly large levels of direct vibration, leading to bearing rubbing at high speeds. If vibration levels would permit running to higher speeds, sudden whirl and/or whip would occur when the rotor synchronous speed matches the fixed frequency at 385 Hz, indicating a natural frequency of the system.

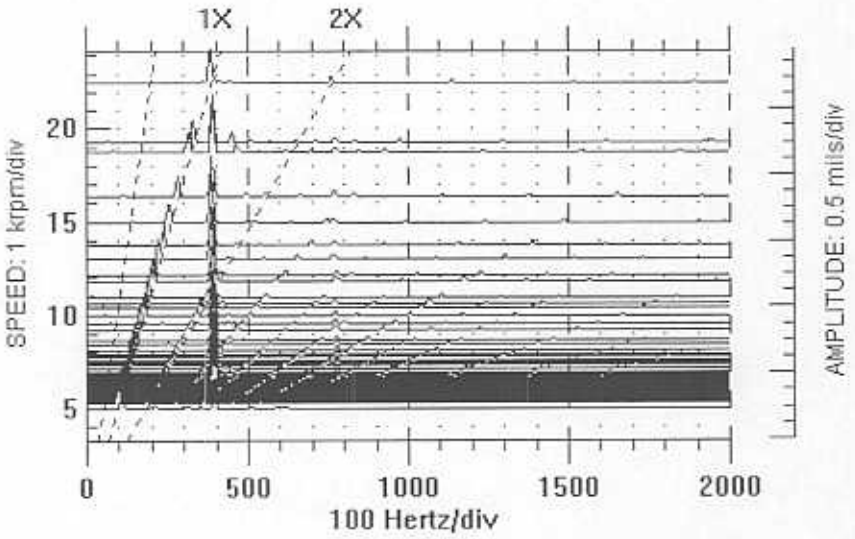

Fig. 46 Waterfall plot of imbalance *U1* response (coastdown) at left vertical eddy current sensor with rotor supported on original pressure dam bearings at pressure ratio equal to 3.04

Another example of pneumatic hammer is given in Fig. 47 (pressure ratio equal to 2.36) where the onset speed of the fixed-frequency hammer instability (340 Hz) is at 11,500 rpm. Fig. 48 shows the corresponding Bode plot where direct vibration levels jump at the onset of the hammer instability. It is also observed that the onset speed of instability is slightly lower for the coastdown than for the run up since the run up onset speed is 13,500 rpm.

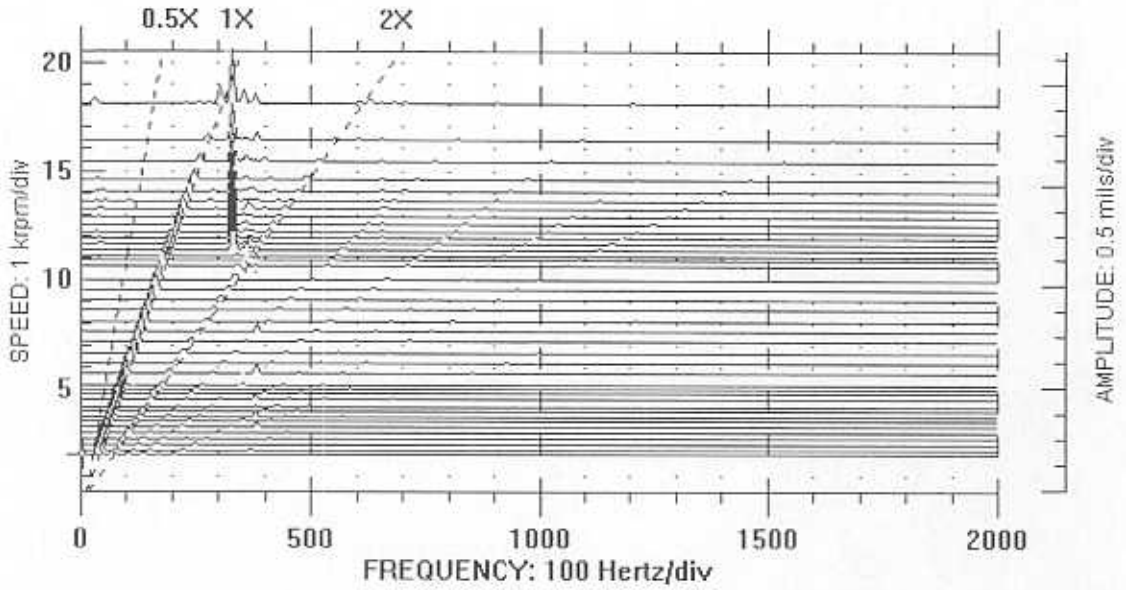

Fig. 47 Pneumatic hammer instability with original pressure dam bearings (*U1* coastdown response, left vertical eddy current sensor, pressure ratio equal to 2.36)

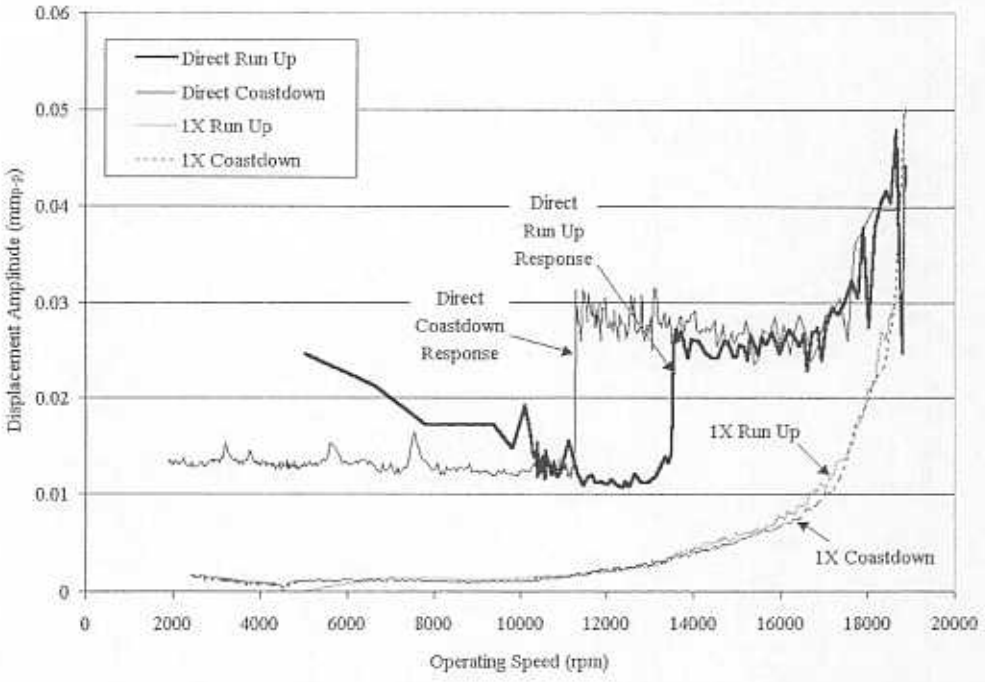

Fig. 48 Bode plot of the waterfall in Fig. 47 (*U1* peak to peak response, left vertical sensor with pressure ratio equal to 2.36)

In general, the original pressure dam bearings experienced increasing frequencies of pneumatic hammer instability for increasing supply pressure ratio. The onset speeds of instability show a 'threshold pressure ratio' below which system effective damping contains (presumably) the pneumatic hammer so that the system experiences only hydrodynamic instability. At pressure ratios above the 'threshold', pneumatic hammer sets in at a supersynchronous frequency. Fig. 49 shows the onset frequency (the speed at which either subsynchronous or supersynchronous instability begins) and the frequency of the destabilizing vibration component. Note the 'threshold pressure ratio' approximately equals 1.62. Also notice that onset frequency decreases and the frequency of pneumatic hammer increases for increasing pressure ratio, such that at very high supply pressure ratios, the system may experience pneumatic hammer at low operating speeds. In fact, one test showed the rotor to experience pneumatic instability even when rotating at very low speeds (around 0-33 Hz) due to the supply pressure alone (motor was not on)[25].

[25] The rotor self-excited at what happened to be the 5th harmonic of the rotor motion.

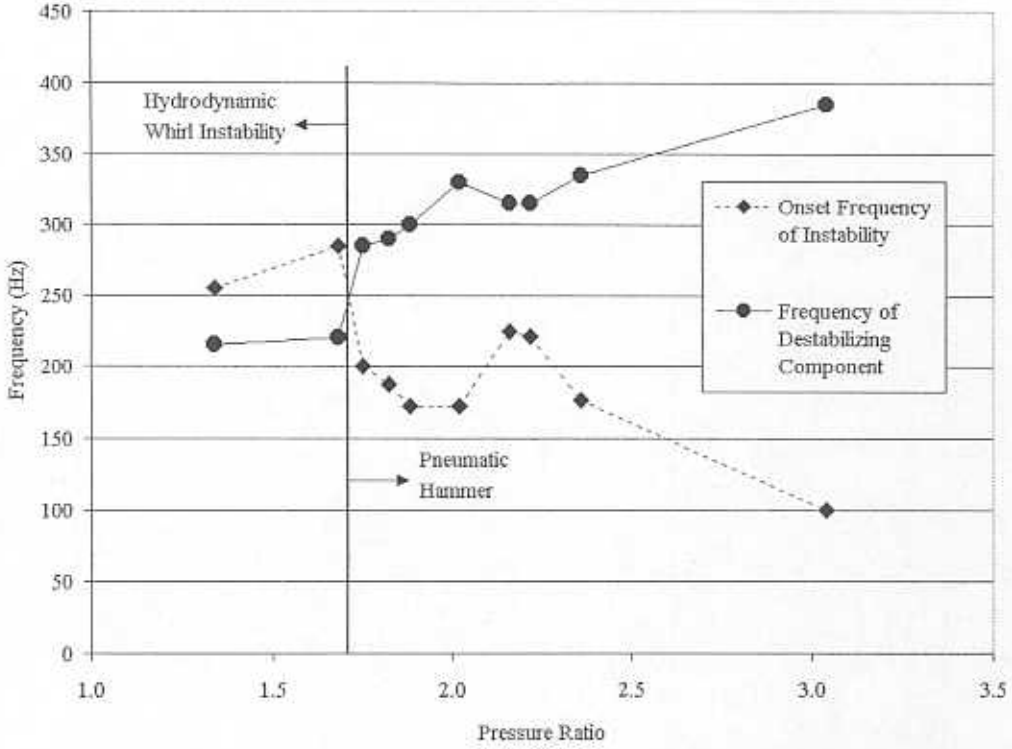

Fig. 49 Instability and onset frequencies for rotor supported on the original pressure dam bearings at increasing pressure ratios

Table 17 lists the onset speeds, frequencies of the instability at onset, and whirl frequency ratios versus supply pressure ratio. The onset speed identifies when hydrodynamic whirl instability (subsynchronous) or pneumatic hammer (supersynchronous) first begins indicating whirl frequency ratios less than one and greater than one for each respective instability.

Table 17 Pneumatic hammer instability characteristics from coast down responses with rotor supported on (original) pressure dam bearings

Supply Pressure Ratio	*[A] Onset Speed of Rotor Instability (Hz)*	*[B] Frequency of Instability at Onset (Hz)*	*Whirl Frequency Ratio = [B]/[A]*
1.34	255	215	0.84
1.68	285	220	0.77
1.75	200	285	1.43
1.82	188	290	1.55
1.88	173	300	1.73
2.02	173	330	1.90
2.16	225	315	1.40
2.22	221	315	1.43
2.36	177	335	1.90
3.04	100	385	3.85

Fig. 50 shows an example where hydrodynamic whirl instability sets in when the synchronous speed reaches 12,600 rpm (210 Hz), with the whirl frequency dropping to 175 Hz shortly after onset. Although not shown here, the corresponding bode plot indicates the critical speed at 12,300 rpm (205 Hz).

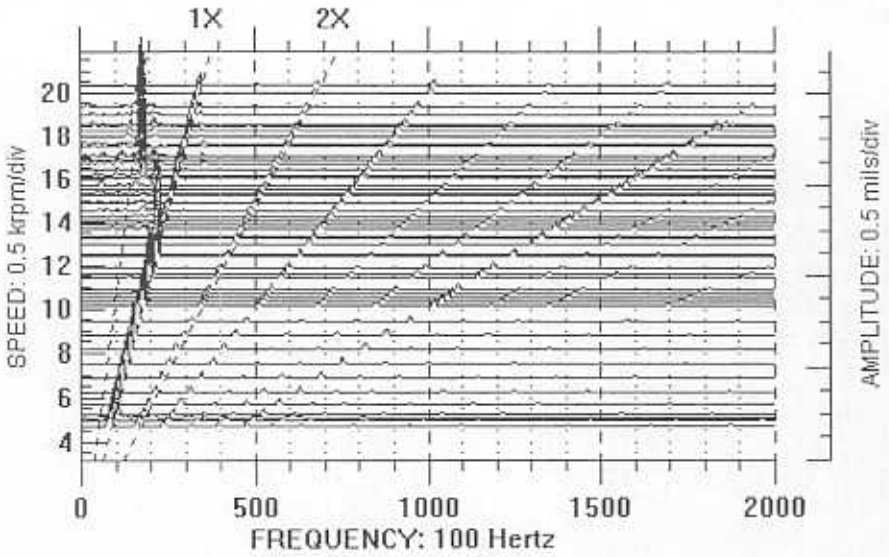

Fig. 50 Waterfall plot of coastdown response to remnant imbalance at right vertical eddy current sensor with rotor supported on (original) pressure dam bearings at pressure ratio equal to 1.38

Coast Down Tests: Rotor Supported on Modified Pressure Dam Bearings[26]

The main objective of testing the rotor supported on the modified pressure dam bearings is to determine if the orifice redesign and the addition of the relief grooves (described in Appendix C) eliminated the pneumatic hammer instability. Therefore, several coast down tests were performed at various supply pressures (response to remnant imbalance only). It should be noted that the system requires much higher supply pressures to support the rotor on the modified bearings than the supply pressures needed to support the rotor on the original pressure dam bearings. In fact, for coastdown tests with supply pressure ratio equal to or less than 5.08, the supply pressure was initially raised (to a pressure ratio between 3.72 and 5.08) in order to support the rotor on run ups. Once the rotor reaches the top speed for the coastdown test, the supply pressure ratio was lowered to the desired test supply pressure. If the

[26] Tests with calibrated imbalance masses were not performed with the rotor supported on the modified bearings.

supply pressure was not initially raised to higher supply pressures, the rotor was not able to spin at all. This indicates that much of the support at lift off comes from the hydrostatic film rather than the immediate generation of a hydrodynamic film. This lack of sufficient hydrostatic support is due to the large side leakage at the grooves machined at the leading edge of the pressure dams.

Fig. 51 shows a sample coast down response, giving the direct and synchronous response at the right bearing (vertical and horizontal eddy current sensors) for supply pressure ratio equal to 5.08. The direct responses show considerable non-synchronous vibration at higher speeds (above the critical speed) beginning at the threshold speed of instability (16,490 rpm with whirl frequency ratio equal to 0.5). The non-synchronous components are due to hydrodynamic whirl instability alone since *no evidence of pneumatic hammer is observed with the modified bearings.*

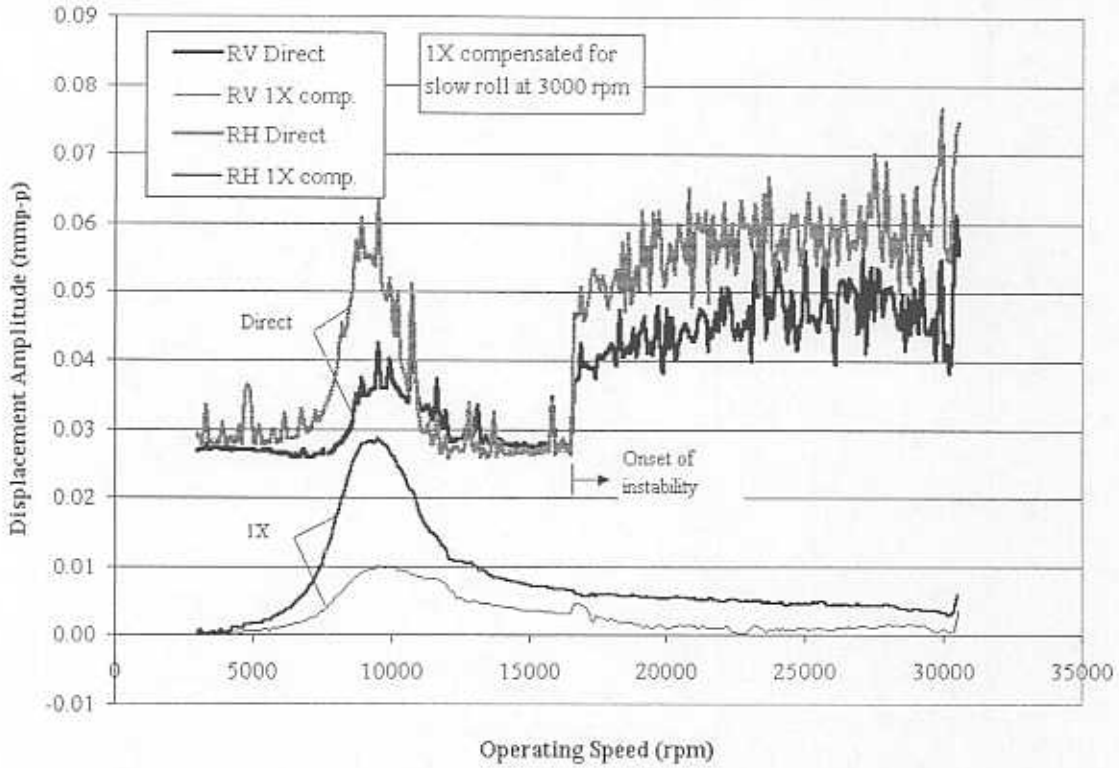

Fig. 51 Response (peak to peak) at right (modified) pressure dam bearing with pressure ratio equal to 5.08

The waterfall plot of the coastdown response for the right vertical sensor at supply pressure ratio equal to 5.08 (Fig. 52) shows a locked-frequency instability with whirl frequency ratios ranging from 0.5 at the threshold speed (17,160 rpm) to 0.36 at the highest recorded speed (28,500 rpm). Since the whirl frequency is fixed, the whirl frequency ratio becomes smaller with increasing rotor speed. The spectra indicate that the whirl frequency becomes the dominant frequency, meaning that the amplitude of vibration for the whirl frequency is larger than the amplitude of synchronous frequency (a characteristic of 'half-whirl').

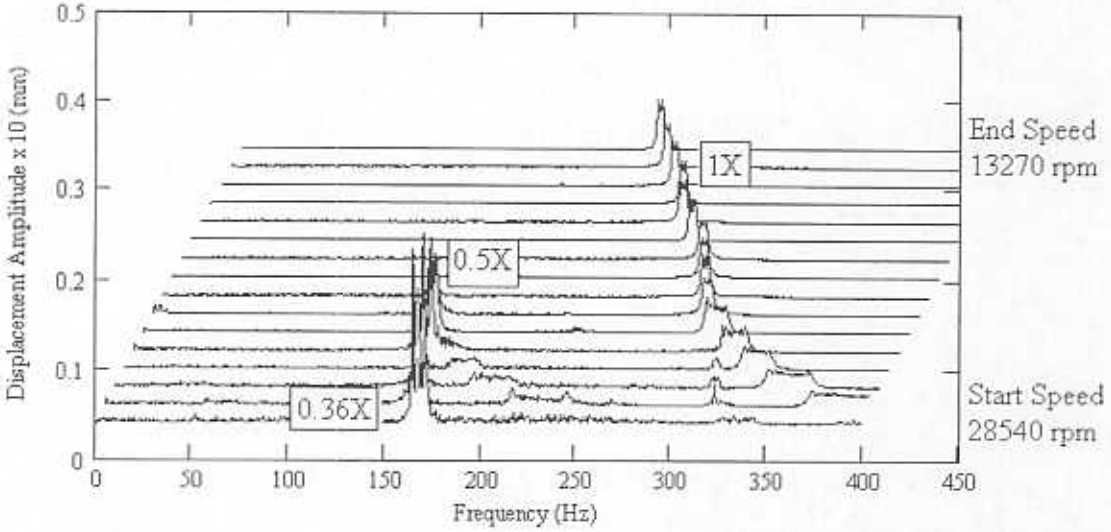

Fig. 52 Waterfall coastdown response at the right vertical eddy current sensor of the rotor supported on the modified pressure dam bearings with pressure ratio equal to 5.08

Table 18 summarizes the whirl frequency ratios at the threshold speeds of instability for both the left and right modified pressure dam bearings. The WFR of the modified pressure dam bearings are always 0.5 at the threshold speed, indicating hydrodynamic whirl instability at an operating speed two times the natural frequency.

Table 18 Critical speeds, threshold speeds, whirl frequencies, and whirl frequency ratios for rotor supported on the modified pressure dam bearings

Supply Pressure Ratio	*Critical Speed (rpm)*	*Threshold Speed (rpm)*	*Whirl Frequency (rpm)*	*Whirl Frequency Ratio*
2.36	-	15,000	7500	0.5
3.38	-	14,400	7200	0.5
3.72	8900	15,600	7800	0.5
5.08	9800	16,800	8400	0.5

The critical speeds are considerably lower with the modified pressure dam bearings than with the original pressure dam bearings. This is expected since the lower direct stiffnesses of the modified pressure dams (with relief grooves) are not able to provide a similar load carrying capacity to that of the original pressure dam bearing.

Damping ratios through the critical speeds are considerably higher (than with the response of the rotor supported on the three lobe bearings) such that critical speeds are not always discernable at low supply pressures. System damping is large enough that evaluation of damping ratios with the bandwidth and/or Q factor methods does not satisfy the criterion that the damping ratio be less than 10 percent.

For the original bearings, the existence of pneumatic hammer instability is also evidenced when reviewing the bearing transmitted loads. The load transmitted to the original pressure dam bearings is on the order of 9-35 N through the critical speed and up to 111 N when unstable at supply pressure ratio equal to 3.04[27]. The bearing transmitted loads through the critical speed for the rotor supported on the modified pressure dam bearings are between 3.5-5.0 N for increasing supply pressures, and up to 3.6 N when unstable at higher supply pressures, shown in Fig. 53.

---

[27] Due to the pneumatic hammer instability, this is the highest supply pressure ratio maintained during experiments with the rotor supported on the original pressure dam bearings.

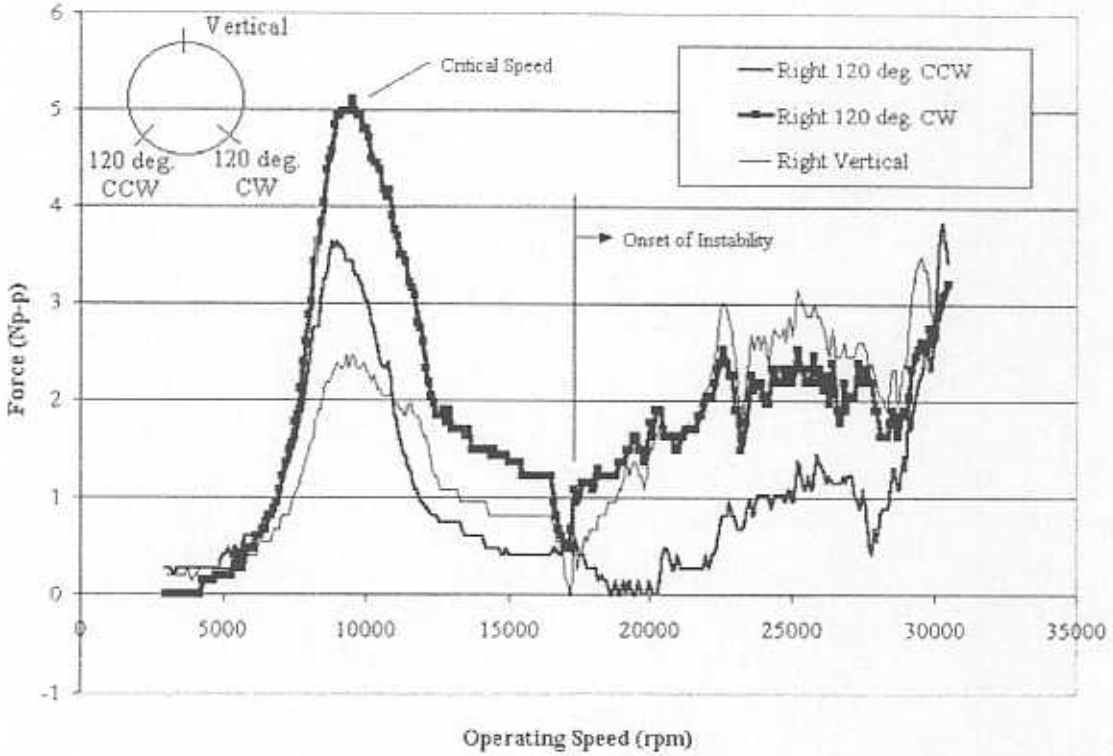

Fig. 53 Bearing transmitted (peak to peak) loads from coast down response of rotor supported on modified pressure dam bearings at pressure ratio equal to 5.08. Insert shows physical location of load cells.

Closure for the Rotor Supported on the Original and Modified Pressure Dam Bearings

The original pressure dam bearings having orifices feeding directly into the pressure dams are prone to exhibit pneumatic hammer over a range of speeds and sufficiently high supply pressures. The findings follow similar results as those reported by Lund [32] and Stowell [39], establishing a distinct pattern for the onset of pneumatic hammer instability with hammer occurring even at nearly zero speed. The pneumatic hammer is characterized by fixed frequency vibration components occurring at supersynchronous frequencies. The frequency of the pneumatic hammer instability component increases with supply pressure. Large levels of supply pressure seemingly

increase the hammer tendency. For the geometry of this test bearing, a lower supply pressure tends to reduce the flow-versus-pressure time lag within the feed orifices and therefore reduce the tendency of the hammer instability. At low supply pressures, distinct hydrodynamic instabilities are observed.

A redesign of the feed orifice completely eliminates pneumatic hammer: by decreasing the number of orifices from six to three, decreasing the diameter of the orifices by 50 percent, moving the orifices from the beginning of the dams to the lands between the adjacent dams, and adding relief grooves to the leading edge of the pressure dams. The relief grooves allow the entrapped air volume to escape eliminating the flow-versus-pressure time lag in the dams. Whirl frequency ratios for the modified bearings range from 0.5 to 0.36 for increasing supply pressure (the whirl frequency is fixed at the natural frequency of the bearing) and are always 0.5 at the threshold speed.

Overall, the rotor supported on the modified pressure dam bearings offers considerable damping through the critical speeds (larger than offered when supported on the three lobe bearings). The critical speeds and natural frequencies of the original pressure dam bearings increase with supply pressure. Since the modified pressure dam bearings continually allow gas to escape from the machined pressure dams, the rotor supported on these bearings has considerably lower critical speeds and natural frequencies, which are nearly constant for increasing pressure ratios. The rotor supported on the modified pressure dam bearings exhibits significantly lower bearing transmitted forces, especially when unstable at higher supply pressures.

HyPad® Tilting Pad Hybrid Bearing

Several tests with the rotor supported on HyPad® tilting pad bearings were conducted, investigating the overall rotor/bearing performance and the effect of clearance on critical speeds, damping ratios, and threshold speeds of instability. Measurements with set radial clearances equal to 0.10 mm and 0.05 mm on the

HyPad® bearing installed at one side of the rotor were measured with a three lobe bearing installed at the other end of the rotor[28]. Measurements with a set bearing clearance equal to 0.02 mm on the HyPad® bearing were measured with an additional HyPad® bearing installed instead of the three lobe bearing. The geometry of this additional HyPad® bearing was developed as an initial prototype and is therefore not identical to the bearing for which results are reported here [36]. Note that the influence of the auxiliary bearing performance (namely the three lobe bearing) may affect the performance of the HyPad® test bearing by increasing vibration levels and reducing threshold speeds.

Coastdown Responses[29]

Fig. 54 shows the rotor coast down response (remnant imbalance) for the rotor supported on the HyPad® bearing with set radial clearance equal to 0.01 mm (the largest test clearance). Since the rotor is supported with the HyPad® bearing and the auxiliary three lobe bearing, the response at the rotor end being supported by the HyPad® tilting pad bearing displays additional vibration levels (a second set of amplitude peaks) due to the influence of the three lobe bearing. The HyPad® bearing evidences lower critical speeds with lower damping ratios than is evidenced from the three lobe bearing.

---

[28] Only one HyPad® bearing was available at the time of testing, and so the three lobe bearing served as an auxiliary support bearing.

[29] Note that tests are not performed at all the same supply pressure ratios for the various bearing clearances.

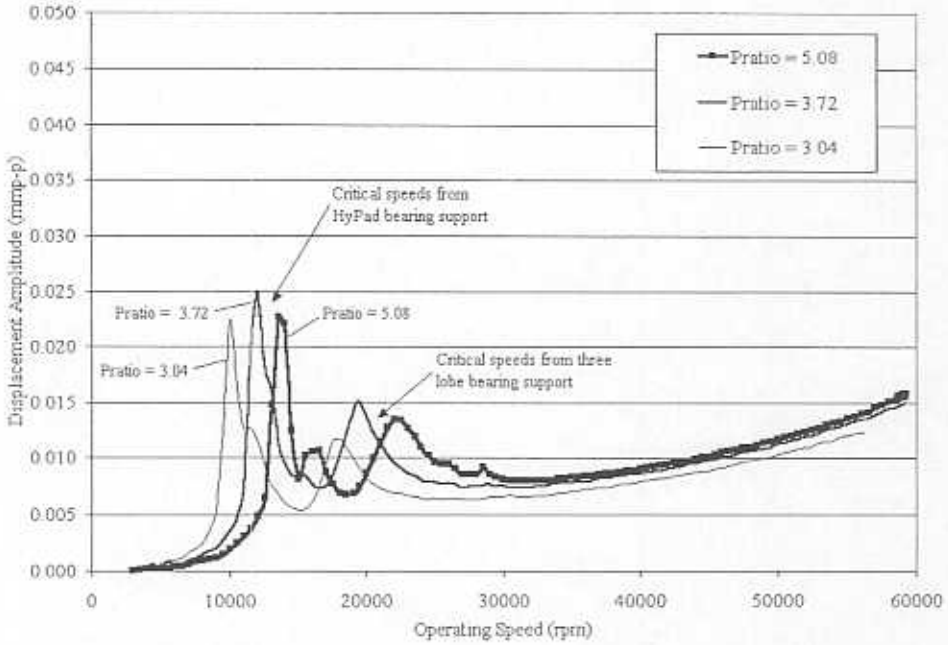

Fig. 54 Synchronous remnant imbalance response at vertical eddy current sensor of rotor supported on HyPad® tilting pad bearing with set radial clearance equal to 0.10 mm

The critical speeds at the HyPad® and at the three lobe bearings overlap for the response with HyPad® set radial clearance equal to 0.05 mm, shown in Fig. 55 by broader peaks for supply pressure ratios equal to 5.08 and 3.72. The critical speed for supply pressure ratio equal to 2.36 occurs simultaneously with the critical speed at the three lobe bearing, and the peak is therefore not as broad or large (in magnitude) as the peaks at the other two supply pressure ratios. The increase in critical speeds (as compared to the rotor response with bearing set clearance equal to 0.10 mm) indicates a stiffening effect for decreasing clearance.

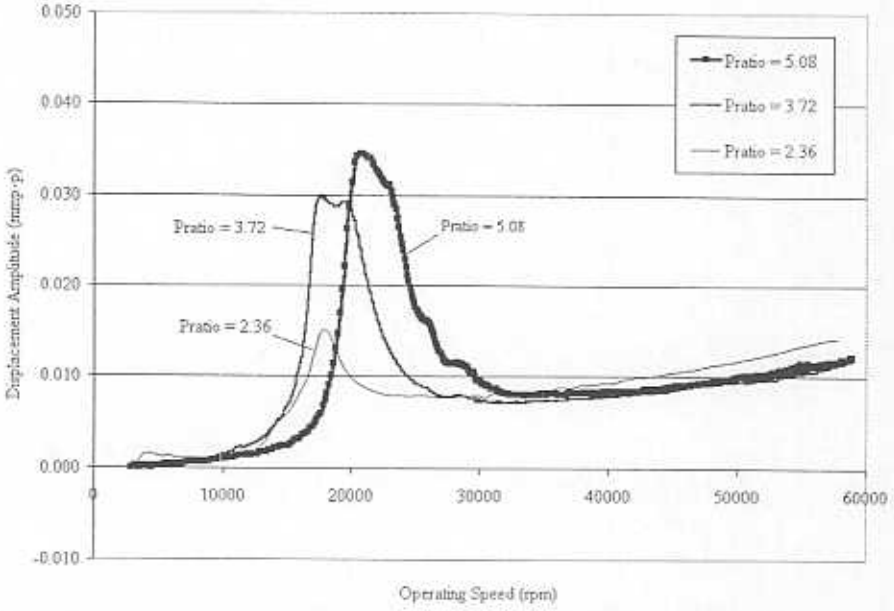

Fig. 55 Synchronous remnant imbalance response at vertical eddy current sensor of rotor supported on HyPad® tilting pad bearing with set radial clearance equal to 0.05 mm

Fig. 56 displays the response of the rotor supported on the HyPad® bearing with set radial clearance equal to 0.02 mm (with the prototype HyPad® auxiliary bearing). While the critical speeds fall between the critical speeds observed with set radial clearances equal to 0.10 mm and 0.05 mm, peak response amplitudes for all clearance settings increase with decreasing clearance.

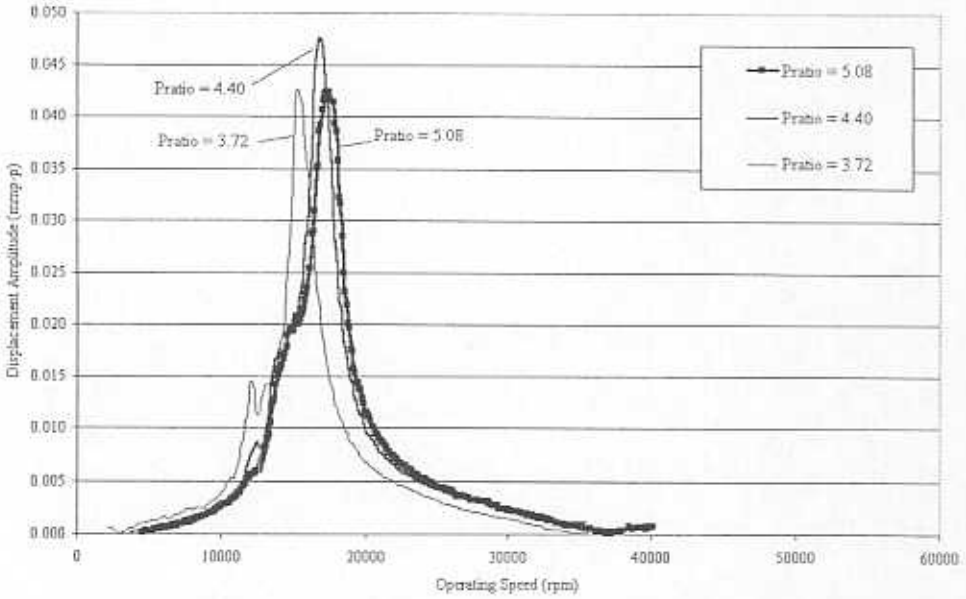

Fig. 56 Synchronous remnant imbalance response at vertical eddy current sensor of rotor supported on HyPad® tilting pad bearing with radial set clearance equal to 0.02 mm

Damping Ratios

Table 19 summarizes the damping ratios identified from the amplitudes of synchronous response for the rotor supported at the HyPad® tilting pad bearing. The values of damping ratio increase from the rotor response with bearing set radial clearance of 0.10 mm to the rotor response with bearing set radial clearance equal to 0.05 mm. Conversely, damping ratios decrease from the rotor response with bearing set radial clearance of 0.05 mm to the rotor response with bearing set radial clearance equal to 0.02 mm. Since the damping ratios are determined using the bandwidth and Q factor methods, this inconsistent behavior is explained by the influence of the response of the rotor supported at the auxiliary bearing on the response at the HyPad® bearing. The bandwidth of the peak rotor response with bearing set radial clearance equal to 0.05 mm is actually widened by the overlapping critical speeds observed from the response of the rotor at the auxiliary bearing. Therefore, the method falsely identifies a wider bandwidth response indicating larger damping ratios. The peak rotor responses with bearing set radial clearances equal to 0.10 mm and 0.02 mm give a better

indication of damping ratio trends since the influence of the critical speeds from the rotor response at the auxiliary bearing fall outside the speed range where the damping ratios are evaluated. The damping ratios for these two clearances (0.10 mm and 0.02 mm) appear to decrease with decreasing clearance, although the trend is not strong. Since critical speeds increase for the responses with these bearing set clearances, the damping ratios likely decrease due to an increase in system stiffness rather than a decrease in overall system damping. Appendix F contains the amplitudes and identified speeds for estimation of damping ratios.

Table 19 Damping ratios for rotor supported by HyPad® tilting pad bearing

Radial Set Clearance	*Supply Pressure Ratio*	*Critical Speed (rpm)*	*Damping Ratio (Bandwidth Method)*	*Damping Ratio (Q factor Method)*
0.10 mm	5.08	13,500	0.046	0.046
	3.72	12,000	0.064	0.063
	3.04	9990	0.050	0.050
0.05 mm	5.08	20,680	0.108	0.113
	3.72	17,470	0.114	0.123
	2.36	17,920	0.080	0.082
0.02 mm	5.08	17,270	0.053	0.053
	4.40	16,790	0.049	0.050
	3.72	15,170	0.045	0.046

Threshold Speeds

In general, tilting pad bearings prevent whirl instability by eliminating the cross-coupled force coefficients. Therefore, one would not expect the rotor supported on the HyPad® tilting pad bearings to exhibit whirl instability. This is the case with the rotor supported on the HyPad® bearing and the auxiliary prototype HyPad®

bearings. The rotordynamic performance gives stable behavior to speeds approaching the limit of the test rig (90,000 rpm). But this is not the case for the rotor supported on the HyPad® tilting pad bearing and the auxiliary three lobe bearing (again showing the influence of the auxiliary bearing on system performance). Table 20 summarizes the whirl instabilities found with the rotor supported on the HyPad® bearing and the (auxiliary) three lobe bearing[30]. The threshold speeds decrease with decreasing operating clearance, supporting the claim that damping ratios decrease with decreasing operating clearances. When determining the maximum speed capability of the rotor supported on the HyPad® bearings, supply feed pressure was completely cut off (rotor at high speeds). Although increased friction caused increased heat generation, a purely hydrodynamic film continually supported the rotor.

Table 20 Threshold speeds, whirl frequencies, and whirl frequency ratios for rotor supported on HyPad® tilting pad bearing and three lobe auxiliary bearing

Set Radial Clearance on HyPad®	*Supply Pressure Ratio*	*Threshold Speed (rpm)*	*Whirl Frequency at Threshold (rpm)*	*Whirl Frequency Ratio*
0.10 mm	5.08	88,000	24,060	0.273
	3.72	78,000	20,940	0.268
	2.36	57,000	18,660	0.327
0.05 mm	5.08	60,000	N/A	N/A
	3.72	57,600	N/A	N/A
	2.36	56,000	19,380	0.346

[30] The supply pressure ratio was significantly increased at the three lobe bearing in order to prevent the rotor from becoming unstable at too low rotor speed due to the three lobe bearing support.

Closure for the Rotor Supported on the HyPad® Tilting Pad Bearing

Overall, the performance of the rotor supported on the HyPad® tilting pad bearing depends highly on its set bearing clearance, as well as the auxiliary support bearing. The bearing operates with low levels of damping ratio, sometimes leading to rubs through the critical speeds. The rotor operates free of subsynchronous whirl instabilities (when the prototype HyPad® auxiliary bearing replaces the three lobe bearing) to very high speeds. The test rig capability (rather than HyPad® bearing performance) limits high speed operation. High levels of vibration leading to considerable pad wear and heating due to rotor/pad rub.

Comparison of Natural Frequencies, Threshold Speeds, and Feed Pressures for Rotor Lift-Off with Rotor Supported on Three Types of Bearings

There are clear advantages and disadvantages to the rotordynamic performance of the rotor supported on each of three types of hybrid gas-lubricated bearings: three lobe bearings, (modified) pressure dam bearings, and HyPad® tilting pad bearings.

Fig. 57 shows that the rotor supported on three lobe bearings achieves consistently higher critical speeds, although certain HyPad® bearing set clearances also offer high critical speeds. The rotor supported on the modified pressure dam bearings has the lowest critical speeds. More importantly, amplitudes of vibration through the critical speed determine whether the system will be able to safely pass through the critical speed, and continue to increase operating speed. Amplitude levels (during stable regions) are largest with the rotor supported on the three lobe bearings and lowest for the rotor supported on the modified pressure dam bearings.

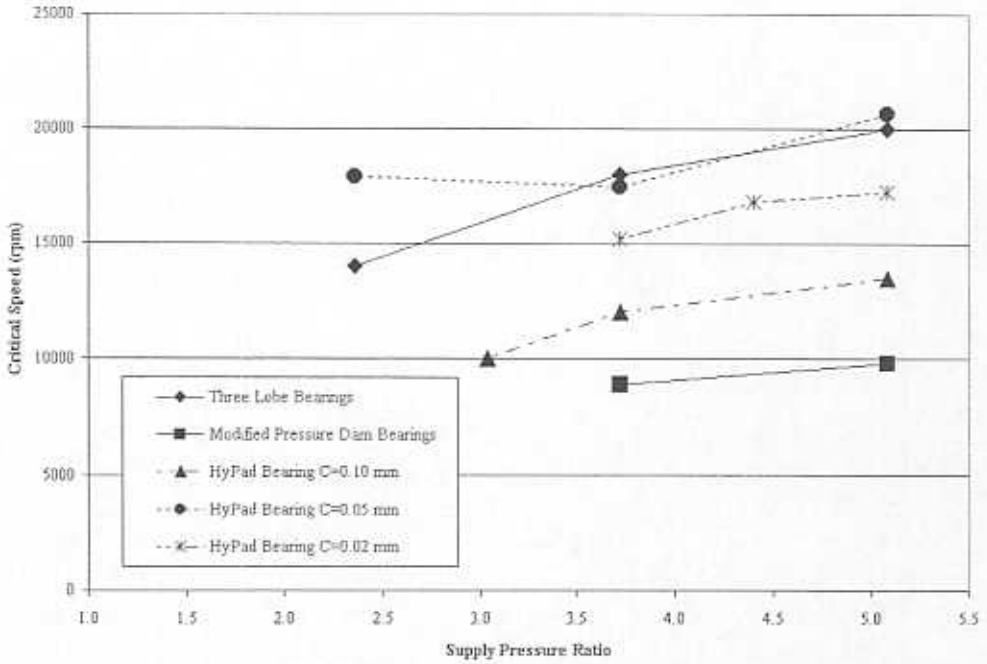

Fig. 57 Critical speeds (natural frequencies) for rotor supported on three types of bearings

Fig. 58 shows the estimated damping ratios for the rotor supported on the three lobe bearings and the HyPad® tilting pad bearings. The response with the rotor supported on the pressure dam bearings is not actually included in the figure since damping ratio levels were larger than the allowable level for evaluation using the Q factor method. The three lobe and HyPad® bearings provide acceptable levels of damping ratio. The damping ratios exhibited by the rotor supported on the HyPad® tilting pad bearings vary considerably with the bearing set clearance.

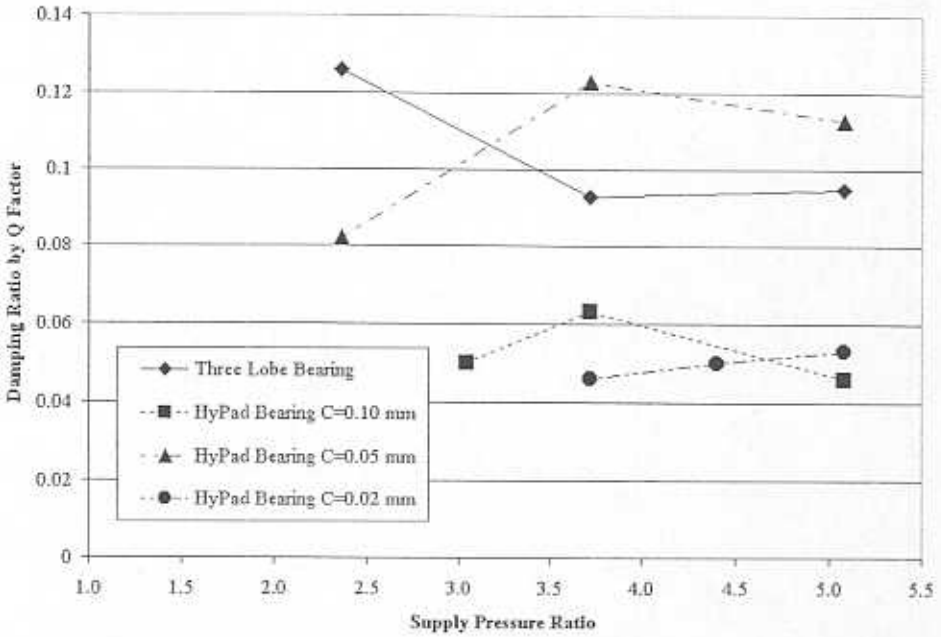

Fig. 58 Damping ratio estimated by Q factor method from coastdown response to remnant rotor imbalance for rotor supported on three types of bearings (damping ratios can not be estimated from the rotor response when supported on the modified pressure dam bearings, but are presumably the largest of the rotor supported on the bearing types)

Fig. 59 compares the performance of the bearing types with respect to threshold speeds of instability. The rotor supported on three lobe bearings allows for increasing threshold speeds at the expense of high supply pressures. The rotor supported on (modified) pressure dam bearings experiences very low threshold speeds (dependent on the pressure dam design) and runs the risk of pneumatic hammer instability if the orifices are not designed and positioned properly. The HyPad® tilting pad bearings offer support absent of whirl instability, which is offset by little damping causing high amplitudes of vibration through critical speeds, pad rub and wear, and increased heat due to friction.

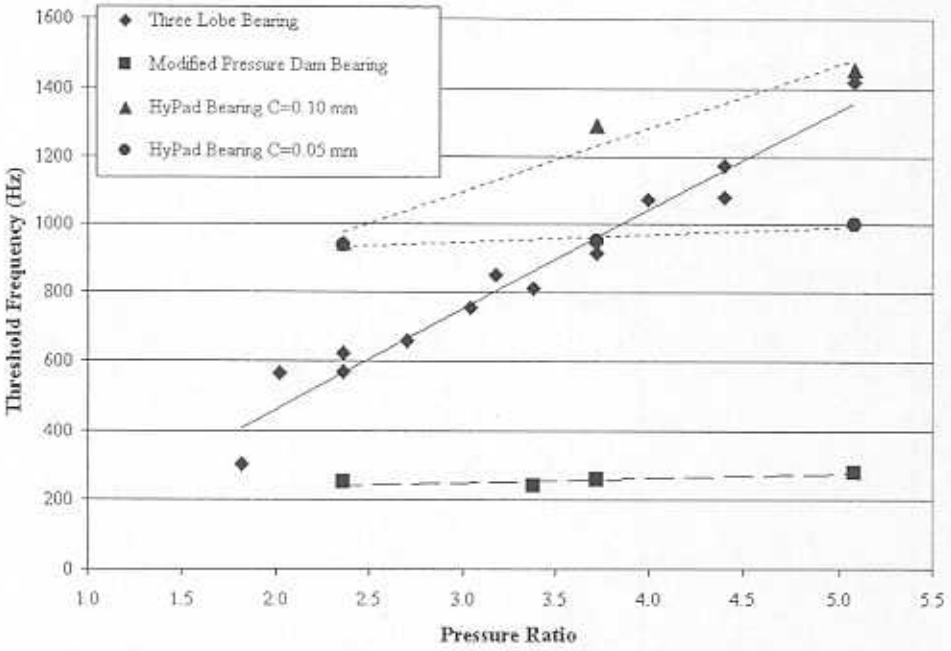

Fig. 59 Threshold frequencies for rotor supported on three types of bearings

Feed pressure ratios required for rotor lift varying greatly depending on the bearing type. Fig. 60 shows that the HyPad® bearings require the largest supply pressure ratios to lift the rotor. Lubricant feed pressure continually leaks from the sides of the tilting pads such that the feed from the single orifice on the bottom pad must lift the rotor. Similarly, the pressure dam bearings leak significant amounts of gas through the relief grooves and therefore also require large feed pressure ratios for rotor lift. The three lobe bearings require the lowest feed pressure ratios for rotor lift. Lower feed pressure ratios allow for smaller, less complex, and lighter weight support systems, and therefore the three lobe bearings offer the most feasible design when considering feed pressure ratios for rotor lift.

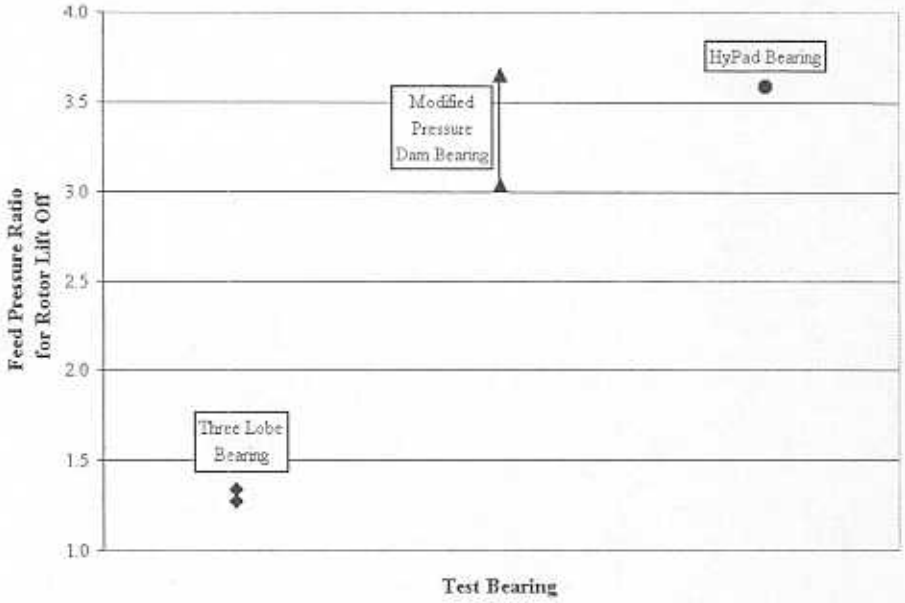

Fig. 60 Feed pressure for rotor lift-off with rotor supported on three types of bearings

Closure for the Performance of the Rotor Supported on Three Types of Hybrid Bearings

The dynamic responses of the rotor supported on three types of bearings offer various advantages and disadvantages. From the results presented, no single rotor/bearing system displays the best overall performance. The rotor supported on the HyPad® bearings eliminates whirl instability and allows for high-speed operation. The rotor supported on the modified pressure dam bearings offers larger levels of damping ratio, but experiences significantly lower natural frequencies and threshold speeds to instability. Improper orifice and dam design may also induce pneumatic hammer instability. The rotor supported on the three lobe bearings requires significantly less feed pressure ratios to lift the rotor, and critical and threshold speeds which increase with increasing pressure supplies. These bearings offer the simplest design considering cost and manufacturability.

SURFACE CONDITION AND LOW-FRICTION COATING

Throughout testing with the rotor supported on three lobe bearings, an effort was made to identify wear patterns and damage to the rotor and/or test bearings associated with transient or continued operation. Note that characterization of the overall experimental performance reported herein sometimes requires the user to test the 'limits of the system' where, occasionally, the system crashes or fails. On most of these occasions, the very conservative protection of the driving motor (1 amp fuses) prevents the system from serious and permanent damaging failure. On several occasions, the rotor coasts down very quickly (due to lack of gas-lubricant film), or the motor gets caught by friction/overheating in the motor armature and suddenly stops the journal from rotating. Other system characteristics have also shown to affect the rubbing and wear performance such as bearing misalignment and supply pressure.

In general, wear and bearing rub was not a concern during continuous (constant speed) operation. The rotor was usually able to gradually coastdown, eventually coming to a complete stop or rotating at low speeds due to the support of the hydrostatic supply pressure, i.e. serious bearing or rotor wear is not considered problematic in these instances. Coastdown tests (coasting down from around 60,000 rpm) would normally take 2 to 15 minutes depending on the magnitude of supply pressure (higher pressures taking longer to decelerate the rotor).

Industrial applications of gas-lubricated bearings have begun to realize the benefit of coating bearing or journal surfaces that come into solid contact with low-friction solid lubricants. To this end, the effect on system performance of a low-friction coating (applied to the test rotor) is investigated.

Wear Patterns

The only established wear patterns have been experienced during the above-mentioned occasions of sudden and violent system failure. With the rotor supported on the three lobe bearings, small amounts of material transfer occur causing aluminum to 'inertia or micro weld' onto the test rotor. After these instances, sanding the rotor with

a fine grit paper removes the transferred material. In random occasions, dirt or other unknown particles have caused minor wear grooves on the test rotor and bearings. Wear patterns on the three lobe bearings are not significant and usually indicate a certain amount of bearing misalignment[31].

Permalon Low-Friction Coating

After performing transient response experiments with the uncoated shaft, a commercially available low-friction coating was applied to the test rotor at room temperature. Permalon 327 is a thermoplastic resin-bonded Teflon based lubricant coating with reported static friction coefficient of 0.06-0.09. Table 21 details the material composition. Aguirrezabala [46] details the entire process of applying and measuring the dry film lubricant. Transient testing was repeated with the coated rotor. Note that applied coating radial thickness is equal to 0.020 mm such that the nominal bearing clearance is reduced from 66 μm to 44 μm. Note also that the reduction in clearance may lead to other effects in system performance (as seen with the rotor supported on the HyPad® tilting pad bearings). In general, the coating adhered well to the rotor surface and did not wear significantly during transient response testing.

Table 21 Permalon 327 physical properties

Physical Properties	
Lubricant	PTFE
Binder	Thermoplastic Resin
Color	Translucent
Static Coefficient of Friction	0.06-0.09
Service Temperature	338.7 K
Intermittent Temperature	388.7 K
Film Thickness	0.005 – 0.0025 mm

[31] As intended with the pad design of the HyPad® bearings, small amounts of Graphalloy material are worn from the pads at start and stop, and may even aid performance by providing a solid particle lubricant film on the test rotor. In fact, small amounts of carbon material have transferred to the rotor, filling pre-existing wear grooves or polishing other surface finish imperfections.

Liftoff and Touchdown Characteristics and Speeds

Transient response tests with the coated rotor were conducted in a similar fashion as the transient response tests conducted with the uncoated rotor (previously described in the "Transient Response" section)[32]. Table 22 details the lift-off speeds and times for increasing supply pressures with the coated rotor supported on three lobe bearings.

Table 22 Lift-off characteristics with coated rotor supported on three lobe bearings

Supply Pressure Ratio	*Lift-off Speed (rpm)*	*Lift-off Time (sec)*
2.09	703.2	0.960
2.22	1404	0.832
2.36	1875	0.896
3.72	2110	0.832
5.08	2344	1.024

Fig. 61 shows slight differences in rotor lift off speed when comparing the transient response of the coated and the uncoated rotor. For most pressure ratios, the coated rotor lifts at a lower speed than the uncoated rotor. The minimum supply pressure ratio required to support the coated rotor for startup equals 2.09 (mass flow rate equal to 3.21E-4 kg/s), which is also slightly lower than with the uncoated rotor (pressure ratio equal to 2.22 and mass flow rate equal to 4.31E-4 kg/s).

---

[32] Appendix I contains a sample transient response with the coated rotor supported on three lobe bearings at pressure ratio equal to 3.72.

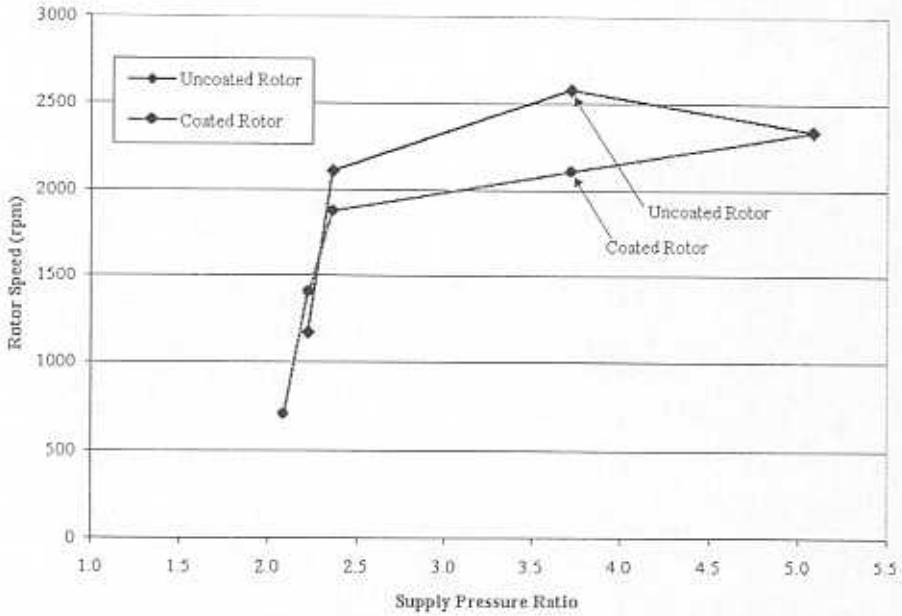

Fig. 61 Rotor speed at lift-off for coated and uncoated shaft at increasing supply pressure ratios

Fig. 62 shows more noticeable differences in the lift-off time when comparing the transient response with the coated and uncoated rotors. The coated rotor lifts off in nearly half the time that the uncoated rotor needs to lift-off, for all supply pressure ratios tested. This is a significant finding, since the rotor is in semi-rigid contact with the bearing until lifting-off. The low-friction coating reduces the amount of semi-rigid contact at start up, therefore reducing bearing rub and wear, and allows for start up at slightly lower supply pressure ratios.

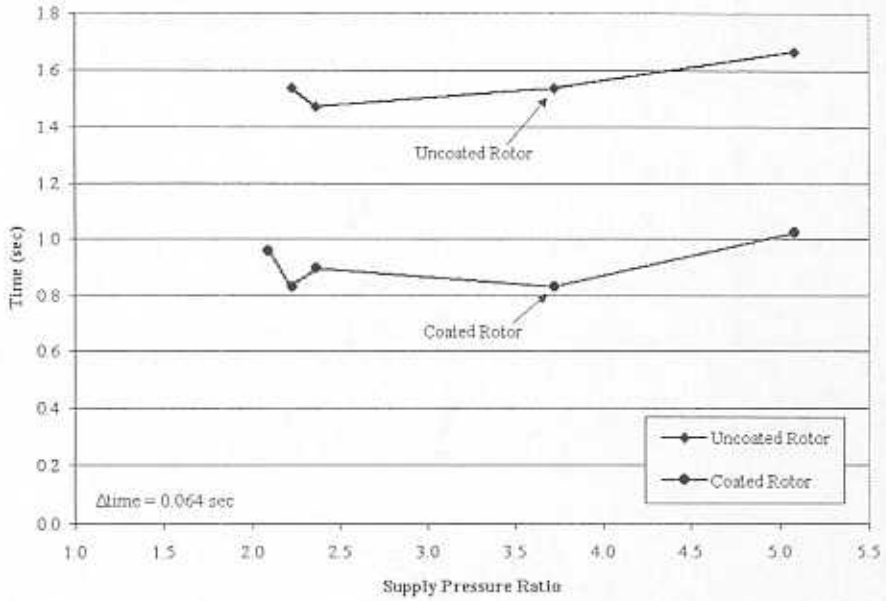

Fig. 62 Time for rotor lift-off with coated and uncoated shaft at increasing pressure ratios

Note that touchdown speeds are not addressed in the table or figures above since the uncoated and coated rotors did not regularly coast to a stop. Usually, the supply pressure needs to be completely shut off before the rotor speed goes to zero and solid contact between the rotor and bearings occurs. On coastdowns with continued hydrostatic feed, the pressure supply assists the inertia of the rotor to overcome the relatively small friction between the rotor and bearing such that rotation is maintained. With the journal rotating, the rotor/bearing system is able to continually generate a hydrodynamic film.

Wear Rates

Through out the test series of the uncoated rotor and three lobe bearings, the rotor/bearing wear was not significant enough to warrant wear rate measurements. As expected from the test design, pairing a softer bearing material with a harder shaft material, observable wear occurred on the bearing surfaces rather than on the rotor surface. After the entire test series with the coated rotor and the three lobe bearings, measurements of the shaft diameter at the bearing locations indicate that approximately

half the coating thickness was worn away over the course of the testing. Only one significant wear track was observed on the coated surface at each bearing location, and are attributed to pre-existing wear patterns on the bearings from prior testing with the uncoated rotor. Measurements with vernier calipers at these wear track locations indicate that the entire thickness of the coating was worn away. Initial coating asperities wore away within the first few transient tests, leaving the overall surface of the coated rotor very smooth at the end of the test series.

Closure for Surface Condition and Low-Friction Coating

As expected, the test bearings exhibited more wear than the test shaft. Most damage to the rotor and/or bearings was experienced during sudden failures associated with forcing the rotor/bearing system to perform in extreme conditions. Wear rates are not significant enough to quantify with the measurement tools available. A profilometer would allow for more significant measurements providing additional insight into the rotor/bearing wear.

A low-friction PTFE based coating applied to the rotor allows for lower rotor lift-off times, thereby reducing the period of semi-rigid contact (wear) between the rotor and bearings. The coating also allows for slightly lower supply pressure (mass flow rates) for rotor lift off, making the hybrid design more feasibly for turbomachinery applications.

Touchdown characteristics were not obtained for either the uncoated or coated shafts since the rotor did not usually stop rotating during a normal coastdown response test (where the supply pressure is maintained throughout the entire test). The touchdown response with gradual supply pressure decrease (simulating actual turbomachinery applications where the hydrostatic feed may be bled from the process gas of the turbomachine itself) should be investigated to determine the affect of the low-friction coating on touchdown speeds.

CONCLUSIONS

An experimental investigation of a test rotor supported on three types of hybrid gas bearings shows clear advantages and disadvantages of rotor static and dynamic performance when supported on each bearing type. Performance at various pressure ratios is investigated by comparing feed pressure for rotor lift off, critical speeds and damping ratios, threshold speeds of instability, and whirl frequency ratios.

The rotor supported on three lobe bearings offers stable operation to threshold speeds increasing linearly with supply pressure. The rotor, when supported on this type of bearing, requires the least amount of supply pressure for lift off and critical speeds are relatively high. Rotor responses to calibrated imbalance masses give mixed results depending on the magnitude of the imbalance mass. Large imbalance increases vibration levels that approach measured clearances and lead to significantly higher bearing transmitted loads. Transient responses in rotor run up tests identify rotor speeds and times when rotor/bearing rolling transitions to rotor rotation with development of a gas film. A low-friction coating applied to the test rotor proves beneficial by reducing the time to lift, thereby decreasing the amount of semi-rigid contact with the three lobe support bearings.

Pneumatic hammer instability is experienced with the rotor supported on pressure dam bearings. A clear relationship between supply pressure ratio and hammer onset is established. A threshold feed pressure ratio identifies when the instability shifts from hydrodynamic type to pneumatic hammer type. An orifice redesign consisting of reducing the number of feed sources, reducing feed source diameter, and modifying the feed source location, completely eliminates pneumatic hammer instability. While threshold speeds of instability (due to hydrodynamic instability) remain very low with the redesigned bearing, the rotor supported on pressure dam bearings proves to have the largest amount of damping ratio and lowest vibration levels, although it cannot operate to high speeds.

The rotor supported on HyPad® bearings, novel tilting pad bearings, allows operation to speeds limited only by the test rig drive motor capability (around 90,000

rpm) and is absent of hydrodynamic instability. Vibration magnitudes are high through critical speeds leading to considerable pad rub, wear, and heat generation.

Numerical predictions of rotor/bearing performance are produced using a finite element based model to solve the ideal gas Reynolds equation. Predicted bearing force coefficients are shown to be dependent on excitation frequency, although the dependence is weak in the range of frequency ratios where the rotor/bearing system becomes unstable. Although natural frequencies match well with experimental results, predicted synchronous responses give lower damping ratios, leading to low threshold speeds, and whirl frequency ratios ~ 0.5, as in plain cylindrical bearings.

REFERENCES

[1] Gross, W.A., "A Review of Developments in Externally Pressurized Gas Bearing Technology Since 1959," *Journal of Lubrication Technology*, Vol. 91, (1), 1969, pp. 161-165.

[2] Barnett, M.A., and Silver, A., "Application of Air Bearings to High-Speed Turbomachinery," paper #700720, *proceedings of the Combined National Farm, Construction & Industrial Machinery and Powerplant Meetings, SAE*, September 1970.

[3] Chen, H.M., Howarth, R., Geren, B., et al., "Application of Foil Bearings to Helium Turbocompressor," *proceedings of the 30th Turbomachinery Symposium*, Houston, TX, September 2001, pp. 103-114.

[4] Garner, D.R., Lee, C.S., and Martin, F.A., "Stability of Profile Bore Bearings: Influence of Bearing Type Selection," *Tribology International*, Vol. 13, (5), 1980, pp. 204-210.

[5] Fuller, D.D., "A Review of the State-of-the-Art for the Design of Self-Acting Gas-Lubricated Bearings," *Journal of Lubrication Technology*, Vol. 91, (1), 1969, pp. 1-16.

[6] Shapiro, W., "Steady-State and Dynamic Analyses of Gas-Lubricated Hybrid Journal Bearings," *Journal of Lubrication Technology*, Vol. 91, No. 1, 1969, pp. 171-180.

[7] Piekos, E.S., and Breuer, K.S., "Pseudospectral Orbit Simulation of Nonideal gas-Lubricated Journal Bearings for Microfabricated Turbomachines," *ASME Journal of Tribology*, Vol. 121, (3)., 1999, pp. 604-609.

[8] Piekos, E.S., "Numerical Simulation of Gas-Lubricated Journal Bearings for Microfabricated Machines," *Doctoral Thesis*, Massachusetts Institute of Technology, February 2000.

[9] Fréchette, L.G., Nagle, S.F., et al., "An Electrostatic Induction Micromotor Supported on Gas-Lubricated Bearings," *proceedings of the IEEE 4th International Micro Electro Mechanical Systems Conference, MEMS 2001,* Interlaken, Switzerland, January 2001.

[10] San Andrés, L., and Vance, J., "Feasibility Study on Alternative Oil-Less Bearing Technologies for Automotive Turbochargers," *Final Research Progress Report,* Texas A&M University, College Station, TX, August 2001.

[11] Elrod, H.G. Jr., and Malanoski, S.B., "Theory and Design Data for Continuous-Film, Self-Acting Journal Bearings of Finite Length," Report I-A 2049-13, *Franklin Institute Laboratories for Research and Development,* 1960.

[12] Raimondi, A.A., "A Numerical Solution for the Gas-Lubricated Full Journal Bearing of Finite Length," ASLE Paper No 60 LC-14, *ASLE Transactions*, Vol. 4, 1961, pp. 131-155.

[13] Castelli, V., Elrod H.G., "Solution of the Stability Problem for 360 Deg Self-Acting, Gas-Lubricated Bearings," *Journal of Basic Engineering*, Series D, Vol. 87, (1), 1965, pp. 199-212.

[14] Castelli, V., and Vohr, J.H., "Performance Characteristics of Herringbone-Grooved Journal Bearings Operating at High Eccentricity Ratios with Misalignment,"

Paper No. 14, *Proceedings Gas Bearing Symposium*, University of Southampton, Apr. 1967.

[15] Elrod, H.G. Jr., McCabe, J.T., and Chu, T.Y., "Determination of Gas-Bearing Stability Response to a Step-Jump," *ASME Journal of Lubrication Technology*, Vol. 89, (9), 1967, pp. 493-498.

[16] Czolczynski, K., "How to Obtain Stiffness and Damping Coefficients of Gas Bearings," *Wear*, Vol. 201, (1-2), 1996, pp. 265-275.

[17] Faria, M.T.C., "Finite Element Method of High Speed Grooved Gas Bearings, Ph.D. Dissertation," Texas A&M University, College Station, TX, June 1999.

[18] Faria, M.T.C., and San Andrés, L., "On the Numerical Modeling of High-Speed Hydrodynamic Gas Bearings," *ASME Journal of Tribology*, Vol. 122, (1), 2000, pp. 124-130.

[19] Faria, M.T.C., "An Efficient Finite Element Procedure for Analysis of High-Speed Spiral Groove Gas Face Seals," *ASME Journal of Tribology*, Vol. 123, (1), 2001, pp. 205-210.

[20] San Andrés, L. and Wilde, D., "Finite Element Analysis of Gas Bearings for Oil-Free Turbomachinery," *Revue Européenne des Eléments Finis*, Vol. 10, (6-7), 2001, pp.769-790.

[21] Lund, J.W., "Calculation of Stiffness and Damping Properties of Gas Bearings," *ASME Journal of Lubrication Technology*, Vol. 90, (4), 1968, pp. 793-803.

[22] Archibald, F.R., and Hamrock, B.J., "The Rayleigh Step Bearing Applied to a Gas-Lubricated Journal of Finite Length," *ASME Journal of Lubrication Technology*, Vol. 89, (1), 1967, pp. 38-46.

[23] Malanoski, S.B., "The Rayleigh Step Bearing Applied to a Gas-Lubricated Journal of Finite Length," *ASME Journal of Lubrication Technology*, Vol. 90, (3), 1968, pp. 520-521.

[24] Hamrock, B.J., "Rayleigh Step Journal Bearing: Part 1 Compressible Fluid," *ASME Journal of Lubrication Technology*, Vol. 90, (1), 1968, pp. 271-280.

[25] Castelli, V., and Pirvics, J., "Review of Numerical Methods in Gas Bearing Film Analysis," *ASME Journal of Lubrication Technology*, Vol. 90, (4), 1968, pp. 777-792.

[26] Constantinescu, V.N., and Galetuse, S., "Pressure Drop Due to Inertia Forces in Step Bearings," *ASME Journal of Lubrication Technology*, Vol. 98, (1), 1976, pp. 167-174.

[27] Nicholas, J.C., "Pressure Dam Bearing Design for Optimum Turbomachinery Stability," *Hydrocarbon Processing*, Vol. 62, (4), 1983, pp. 91-97.

[28] Gunter, E.J., Jr., Castelli, V., and Fuller, D.D., "Theoretical and Experimental Investigation of Gas-Lubricated, Pivoted-Pad Journal Bearings," *ASLE Transactions*, Vol. 6, (4), 1963, pp. 346-357.

[29] Castelli, V., Stevenson, C.H., and Gunter, E.J., Jr., "Steady-State Characteristics of Gas-Lubricated, Self-Acting, Partial-Arc Journal Bearings of Finite Width," *ASLE Transactions*, Vol. 7, (2), 1964, pp. 153-167.

[30] Gunter, E.J., Hinkle, J.G., and Fuller, D.D., "The Effects of Speed, Load, and Film Thickness on the Performance of Gas-Lubricated, Tilting-Pad Journal Bearings," *ASLE Transactions*, Vol. 7, (4), 1964, pp. 353-365.

[31] Shapiro, W., "Steady-State and Dynamic Analyses of Gas-Lubricated Hybrid Journal Bearings," *Journal of Lubrication Technology*, Vol. 91, (1), 1969, pp. 171-180.

[32] Lund, J.W., "The Hydrostatic Gas Journal Bearing with Journal Rotation and Vibration," *Journal of Basic Engineering*, Trans. ASME, Series D., Vol. 86, (2), 1964, pp. 328-336.

[33] Lund, J.W., "A Theoretical Analysis of Whirl Instability and Pneumatic Hammer for a Rigid Rotor in Pressurized Gas Journal Bearings," *ASME Journal of Lubrication Technology*, Vol. 89, (2), pp. 154-166.

[34] Zhang, R.Q., and Chang, H.S., "A New Type of Hydrostatic/Hydrodynamic Gas Journal Bearing and its Optimization for Maximum Stability," *Tribology Transactions*, Vol. 38, (3), 1995, pp. 589-594.

[35] Jing, G., Zhang, P., and Hu, Z.Y., "On Fundamental Characteristics of a Hybrid Gas-Lubricated Journal Bearing with Surface-Restriction Compensation," *Tribology Transactions*, Vol. 40, (3), 1997, pp. 528-536.

[36] Greenhill, L.M., and Lease, V.J., "Hydrostatic Pivoted Pad Bearings for Oil-Free Turbomachinery," paper #3005, *proceedings of the 2001 ISCORMA Conference*, Lake Tahoe, CA, Oct. 2001.

[37] Majumder, M.C., and Majumdar, B.C., "Theoretical Analysis of Pneumatic Instability of Externally Pressurized Porous Gas Journal Bearings Considering Velocity Slip," *ASME Journal of Tribology*, Vol. 110, (4), 1988, pp. 730-733.

[38] Sun, D.C., "Stability of Gas-Lubricated, Externally Pressurized Porous Journal Bearings," *ASME Journal of Lubrication Technology*, Vol. 97, (3), 1975, pp. 494-505.

[39] Stowell, T.B., "Pneumatic Hammer in a Gas Lubricated Externally Pressurized Annular Thrust Bearing," *ASME Journal of Lubrication Technology*, Vol. 91, (4), 1971, pp. 498-503.

[40] Mehta, N.P., "Static and Dynamic Characteristics of Orthogonally-Displaced Pressure Dam Bearings," *Tribology Transactions*, Vol. 36, (2), pp. 201-206.

[41] Díaz, S., and San Andrés, L., "High Speed Test Rig for Identification of Gas Journal Bearing Performance: Design, Constraints, and Fabrications," *Report TRC-RD-1-99 The Turbomachinery Laboratory*, Texas A&M University, College Station, TX, May 1999.

[42] Días, S., "Waterfall.VI," *internal document*, Rotordynamics Laboratory Texas A&M University, College Station, TX, 2001.

[43] San Andrés, L., "Mcad WFall LABVIEW analysis.mcd," *personal communication,* Rotordynamics Laboratory Texas A&M University, College Station, TX, 2001.

[44] Díaz, S., "CCO-SFD.VI," *internal document*, Rotordynamics Laboratory Texas A&M University, College Station, TX, 2001.

[44] XLTRC/XLTRC^2 Analytical Software Suite, The Turbomachinery Laboratory, Texas A&M University, College Station, TX, 2001.

[45] Aguirrezabala, J., "Low Friction Coating Investigation for Rotor Supported on Three Lobe Hybrid Gas Bearing," *Undergraduate Thesis*, Texas A&M University, College Station, TX, May, 2002.

APPENDIX A: CLEARANCE MEASUREMENTS FOR ROTOR SUPPORTED ON THREE LOBE BEARINGS

Two methods aid to measure the clearance of the three lobe bearings. First, by manually rotating the shaft and observing the 'clearance orbit' using the oscilloscopes displaying the motion of the shaft (the sensors and scope method). Secondly, by using a three-legged bore gauge (± 0.001 mm [± 0.00005 in]) to measure the bore diameter and subtracting the shaft diameter. The sensors and scope method is performed by manually rotating the shaft around the bearing clearance and tracing the orbit on the oscilloscope display. The uncertainty and repeatability are quite poor with the scope method since considerable human error is involved and the applied force may invoke some depression of the o-rings that seal the bearing within the bearing housing, thereby increasing the actual clearance during the measurement. Fig. A1 contains the mapped clearance of the rotor supported on the three lobe bearings by the sensors and oscilloscope method. Each division shown is equal to 25.4 μm (1 mil) in both directions.

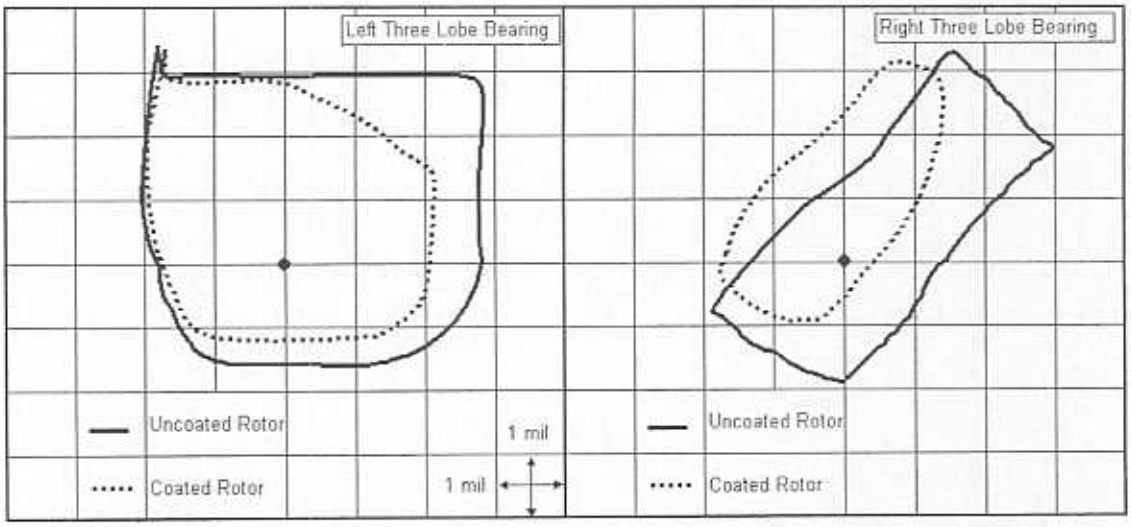

Fig. A1 Mapped three lobe bearing clearances after testing with uncoated rotor and before testing with coated rotor[33]

[33] Refer to the Surface Condition section for full details concerning the coated rotor.

The bore gauge method uses a three-legged bore gauge (legs are 120° apart) to measure the inner diameter of the bearing at the location of maximum and minimum clearance (at the apex of the lobes and at the midpoint of the lobes). Subtracting the shaft diameter determines the clearance.

The testing series with the rotor supported on three lobe bearings is as follows: 1) coast down response with uncoated rotor, 2) transient response at low speeds with uncoated rotor, and 3) transient response at low speeds with coated rotor. Table A1 gives a summary of the clearance measurements from both methods at various points during the testing series. The first two lines show 15-38 μm wear due to the coastdown response experiments. Comparing values given in lines 2 and 5 shows the increase in shaft diameter (decrease in clearance) due to the rotor coating. The shaft coating thickness by the sensors and scope method is between 0-43 μm. Lines 3 and 6 give the nominal clearances for experiments with the uncoated and coated rotor, respectively. Line 8 gives the nominal clearance after transient testing with the coated rotor, showing no additional bearing wear (considering uncertainty). The measured maximum clearance (at the orifices) and the measured minimum clearance (at 60 degrees from the orifices) determine the preload. Dividing the preload by the nominal clearance gives the nondimensional preload, lines 4, 7, and 9. Appendix B contains the preload definition.

Table A1 Clearance and preload measurements for rotor supported on three lobe bearings

Dimension	*Left Bearing*	*Right Bearing*
1. Diametral - Using sensors and scope *before* testing with uncoated rotor on three lobe bearings	102 μm in horizontal direction 102 μm in vertical direction ± 2.54 μm	102 μm in horizontal direction 102 μm in vertical direction ± 2.54 μm
2. Diametral - Using sensors and scope *after* coast down testing and *before* transient testing with uncoated rotor	127 μm in horizontal direction 102 μm in vertical direction ± 2.54 μm	117 μm in horizontal direction 140 μm in vertical direction ± 2.54 μm

Table A1 Continued

Dimension	*Left Bearing*	*Right Bearing*
3. Nominal Radial [Diametral] Clearance measured with Bore Gauge *before* coast down testing with uncoated rotor	66 ± 1.27 μm [132 μm]	65 ± 1.27 μm [130 μm]
4. Nondimensional Preload measured with Bore Gauge *before* coastdown testing with uncoated rotor	0.346 ± 0.012	0.316 ± 0.012
5. Diametral - Using sensors and scope *after* transient testing of uncoated rotor and *before* testing with coated rotor	91 μm in horizontal direction 102 μm in vertical direction ± 2.54 μm	81 μm in horizontal direction 97 μm in vertical direction ± 2.54 μm
Shaft Coating Thickness:	0-35 μm	35-43 μm
6. Nominal Radial [Diametral] Clearance measured with Bore Gauge *before* transient testing with coated rotor	44 ± 1.27 μm [88 μm]	45 ± 1.27 μm [90 μm]
7. Nondimensional Preload measured with Bore Gauge *before* transient testing with coated rotor	0.514 ± 0.032	0.461 ± 0.032
8. Nominal Radial [Diametral] Clearance measured with Bore gauge *after* transient testing with coated rotor	46 ± 1.27 μm [92 μm]	44 ± 1.27 μm [88 μm]
9. Nondimensional Preload measured with Bore Gauge *after* transient testing with coated rotor	0.494 ± 0.032	0.514 ± 0.032

APPENDIX B: THREE LOBE BEARING PRELOAD CALCULATIONS

Equation [B1] describes the minimum clearance and Equation [B2] describes the maximum clearance, where the nominal clearance (C) and preload (r) are unknown and the minimum (at θ) and maximum clearances (at θ_p) are measured.

$$C_{min} = C - r \qquad \text{[B1]}$$

$$C_{max} = C - r\cos(\theta_p - \theta)$$

$$0 \le \theta \le 120^\circ \qquad \text{[B2]}$$

$$\theta_p = 60^\circ$$

Equation [B3] and Equation [B4] determine the dimensional and nondimensional preloads, respectively.

$$r = \frac{C_{min} - C_{max}}{(-1 + \cos(\theta_p - \theta))} \qquad \text{[B3]}$$

$$\bar{r} = \frac{r}{C} \qquad \text{[B4]}$$

APPENDIX C: DESCRIPTION OF PRESSURE DAM AND HYPAD BEARINGS

Hybrid Three-lobe Pressure Dam Bearing

Nicholas [27] presents design guidelines for pressure dam bearings to deter the onset of oil whirl instability. Nicholas found that the bearing clearance directly influences the stability characteristics of plain cylindrical journal bearings, where a tighter the clearance exhibits a higher instability threshold speed. Therefore, the use of pressure dams may be a viable method of eliminating instabilities apparent in the performance of air-lubricated bearings.

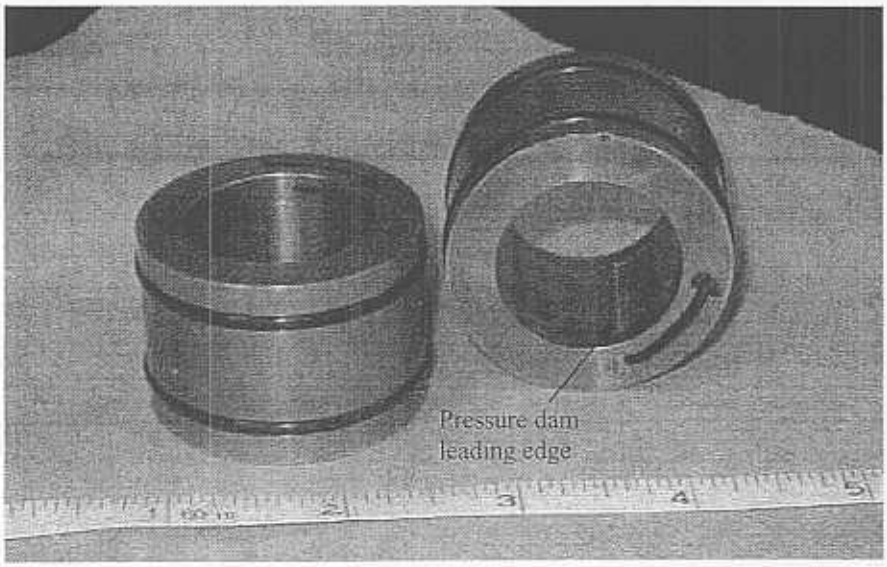

Fig. C1 Pressure dam bearings with six feed holes

The test bearings (Fig. C1) are made of bronze and originally machined as three-lobed cylindrical bearings with air feed holes at the apex of the lobes (identical to the aluminum three lobe bearings). Pressure dams were designed using the guidelines [27] for a typical oil-lubricated pressure dam bearing, and are summarized below.

1) The optimum range of clearance ratio is $K = 3.0$ to 6.0 ($K = H_D / C_L$, the ratio of the clearance in the dam to the clearance in the land).
2) The pressure dams should extend about 75% of the arc length of a pad.

3) The milling process for the pressure dam provides a surface finish that promotes turbulence. No additional machining is required. The surface finish of the pocket region is also of secondary importance since the side lands hold the flow and pressure.
4) The step should not be made sharp since fluid inertia effects tend to decrease load capacity.
5) Pocket axial lengths should be 65 to 70% of the total axial bearing length.

The bronze bearings were sent to Bearings Plus in Houston, Texas for machining. Specifications for the pressure dams (original bearings[34]) are as follows: a dam starts at each location of air feed hole pair and has a pocket depth of 0.127 +/- 0.005 mm (K=1.9 for a nominal clearance of 66 um), an angular extent of 80 degrees, and an axial length of 21.01 +/- 0.13 mm. The dam edges are rounded to the edge of the cutting tool with no additional machining of the pockets. Table C1 gives the dimensions of the bearing. Fig. C2 shows a schematic view of the original bearing. An unwrapped view, starting from vertical and in the direction of θ is shown in Fig. C3. The specified clearance ratio for manufacture is actually less than the optimum value suggested [27] since gas bearings are known to require smaller clearances to provide the needed load capacity due to the compressibility of the gas film [32]. In addition, the designers wished to minimize the dam volume since externally pressurized gas bearings are also prone to pneumatic instability, which develops from large volumes of trapped air [33].

[34] The orifice design of the pressure dam bearings was later modified.

Table C1 Pressure dam bearing geometric characteristics

Parameter	*Original Bearing*	*Modified Bearing*
Length (mm)	30	30
Diameter (mm)	29.5	29.5
Nominal Clearance (μm)	66	66
Orifice Diameter (mm)	1.0	0.5
Number of Orifices	6	3
Orifice Location	At start of dam	In land between dams
Dam Depth (μm)	127	127
Dam Angular Extent (degrees)	80	80
Dam Axial Length (mm)	21.01	21.01
K (clearance ratio)	1.9	1.9
Relief groove width (mm)	-	0.5
Relief groove depth (mm)	-	127

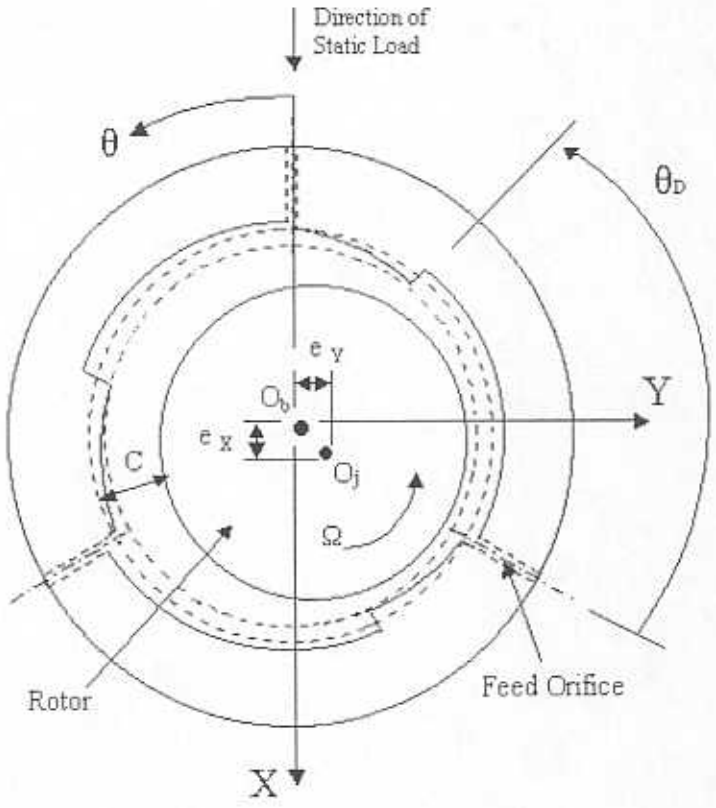

Fig. C2 Schematic view of the original pressure dam bearing

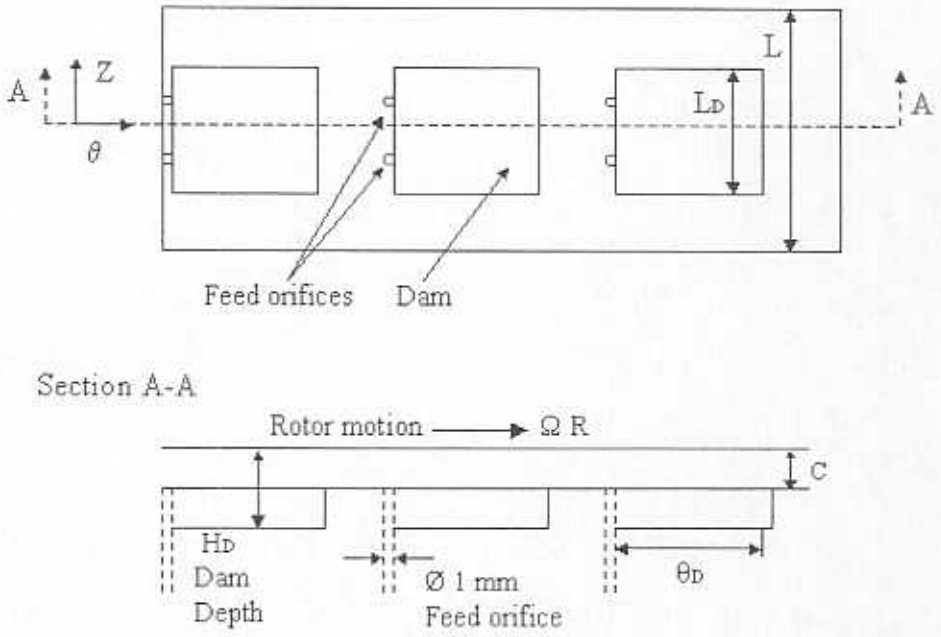

Fig. C3 Unwrapped schematic view of the original pressure dam bearing

The location, number, and diameter of the orifices were modified after initial testing showed the onset of pneumatic hammer[35]. The feedholes located at the beginning of the pressure dams were filled with JB Weld and a new, single orifice with diameter of 0.5 mm was machined in each land halfway between the adjacent pressure dams. Axial relief grooves at the leading edge of the pressure dams were also manually etched using a rifler file to prevent the trapped volume of air within the pressure dam from developing the flow-versus-pressure time lag associated with pneumatic hammer.

---

[35] The results with the rotor supported on pressure dam bearings are thus referred to as the *original* pressure dam bearings (having a total of six feed orifices feeding into the machined dams) and the *modified* pressure dam bearings (having a total of three feed orifices feeding into the lands between the machined dams).

Final specifications for the pressure dams are as follows: a dam starts at each location of air feed hole and has a clearance ratio K=1.75 with a pocket depth of 0.127 mm +/- 0.005 mm (0.005 +/- 0.0002 inch), an angular extent of 80 degrees, and an axial length is 21.01 mm +/- 0.13 mm (0.827 +/- 0.005 inch). The dam edges are rounded to the edge of the cutting tool and no additional machining of the pockets surface was performed. The dimensions of modified bearing are included in Table C1. Fig. C4 and Fig. C5 display the modified pressure dam bearing.

For experiments with the hybrid pressure dam bearings, the test bearings are in the load between pad position such that one orifice feedhole was positioned at the bottom vertical location (under the test rotor when at rest) and the other two feedholes were positioned 60 degrees from the top vertical position.

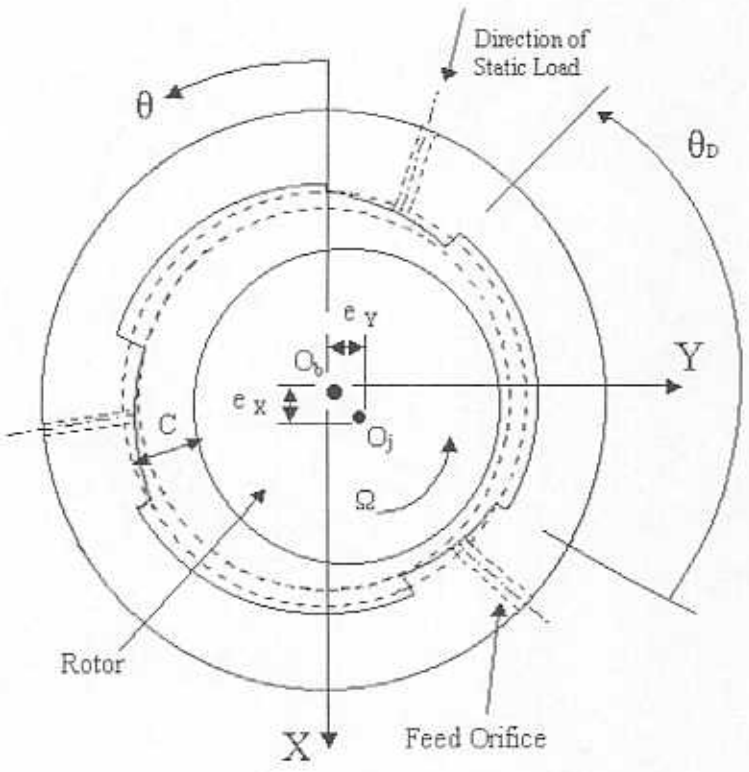

Fig. C4 Schematic view of modified pressure dam bearing

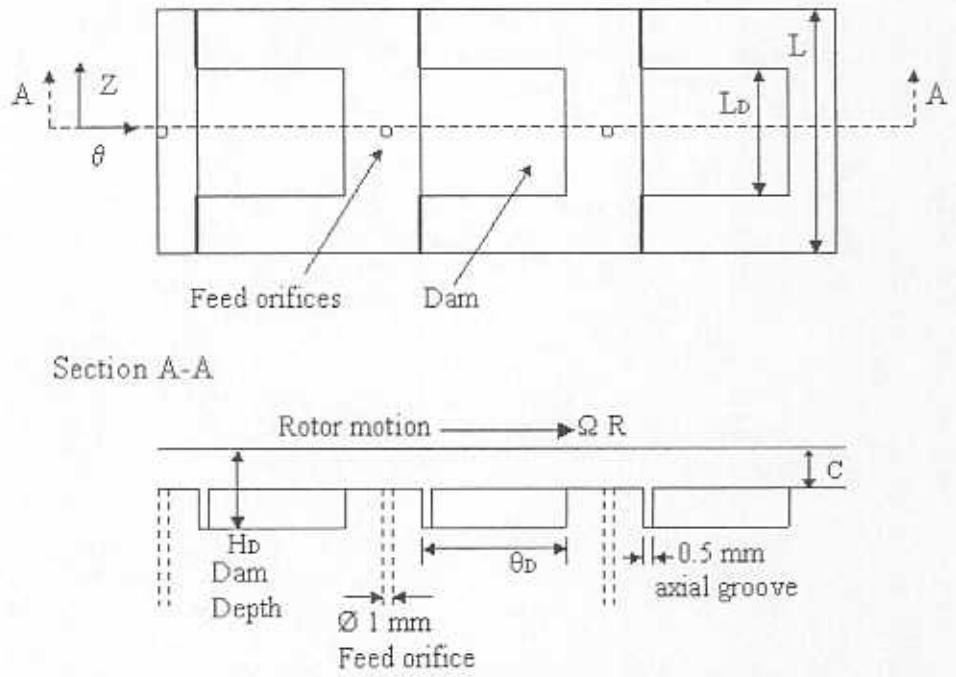

Fig. C5 Unwrapped schematic view of the modified pressure dam bearing

It was discovered during the installation of the modified pressure dam bearings that the outside ends of the test chamber actually deflected when applying supply pressure to the bearings. The downward motion of the rotor seen in the oscilloscopes displaying the eddy current sensor signals and the movement measured by a displacement gage monitoring the top of the rigid mount of the eddy current sensors and the test rig ends, indicated the deflection. Wood blocks placed between the test rig base and ends fit the curvature of the test rig ends. Shims positioned between the test rig base and the wood blocks minimized the displacement due to the application of the supply pressure to less than 12.7 μm on both sides. *The anti-vibration blocks were not in place during testing with the three lobe bearings since the blocks caused increased bearing wear with the modified pressure dam bearings.*

Table C2 lists the measured clearances and nondimensional preloads at various stages throughout experiments with the rotor supported on the original and the modified pressure dam bearings.

Table C2 Clearance and preload measurements for the pressure dam bearings

Dimension	*Left Bearing*	*Right Bearing*
1. Diametral - Using sensors and scope after testing of original pressure dam bearing*	152 μm in horizontal direction 132 μm in vertical direction	147 μm in horizontal direction 0.10 μm in vertical direction
2. Diametral - Using sensors and scope before testing of modified pressure dam bearing**	152-203 μm in both directions	152-203 μm in both directions
3. Diametral - Using sensors and scope *before* testing of modified pressure dam bearing *with anti-deflection blocks installed*	127 μm in horizontal direction 64 μm in vertical direction	127 μm in horizontal direction 76 μm in vertical direction
4. Diametral - Using sensors and scope *after* testing of modified pressure dam bearing *with anti-deflection blocks installed*	178 μm in horizontal direction 178 μm in vertical direction	152 μm in horizontal direction 127 μm in vertical direction
5. Nominal Clearance measured with Bore Gauge (+/- 1.27E-3 mm) after both sets of testing	169 μm	154 μm
6. Nondimensional Preload measured with Bore Gauge after both sets of testing	0.476	0.467

*Shaft placed in both bearings (measured with both bearings installed)

**Shaft placed in one bearing (measured with only one bearing installed)

HyPad® Tilting Pad Hybrid Bearing

DynaTech Engineering, Inc. designed and manufactured the HyPad® tilting pad hybrid test bearings, shown in Fig. C6. The prototype bearing consists of three Graphalloy pads (L= 25.4 mm, R'=14.351 mm, arc length ~ 65 degrees, preload 0.6) with socket-pivot supports that allow for a variable clearance. External pressurization is fed through the socket-pivot support by way of a feeding tube to the back of the pad,

and then through orifice feed holes to the bearing film. A piezoelectric load cell is installed at the top alignment bolt for each bearing[36].

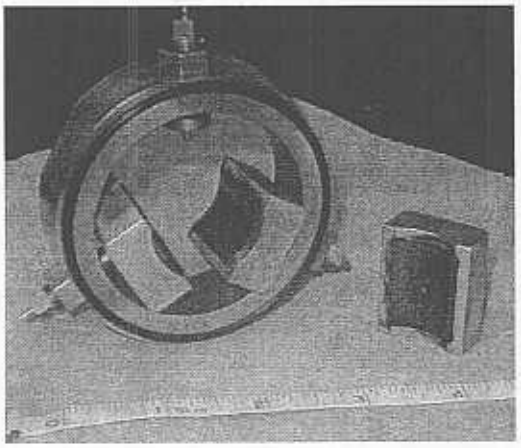

Fig. C6 HyPad ® tilting pad bearing

The pads of the HyPad bearing contain a single feed orifice at their middle plane (0.8 mm in diameter) and a steel tube (2.41 mm in diameter) connecting the pads to the pressurized chamber. The HyPad® bearings were installed such that the rotor is supported at the center of the bearing pad (LOP). It should be noted that while the rigid tubes tend to 'stick' to the tilting pads, the tubes are not secured within the pivoting pads. Care was taken to not disrupt this connection or to push the tubes back into the pivot supports upon installation within the test chamber and of the shaft.

A clearance setting tool, consisting of a finished bronze cylinder with diameter of 28.52 mm (+/- 0.005 mm), is placed within the tilting pads. Incrementally tightening the pads within the bearing housing effectively sets the clearance of the bearing. Subtracting the diameter of the shaft, 28.48 mm (+/- 0.005 mm), indicates a radial clearance of 0.02 mm (0.079 mils) with an uncertainty of 17.7%. With the pads tight, the clearance setting tool can be rotated within the pads by hand (although considerable effort is required) and is then carefully removed from the pads.

---

[36] The larger size of the bearing housing prevented installation of three load cell transducers.

APPENDIX D: MEASURED MASS FLOW RATES FOR ROTOR SUPPORTED ON THREE LOBE BEARINGS

Fig. D1 (with the rotor in place) and Fig. D2 (without the rotor in place) give the recorded mass flow rate at zero rpm for the rotor supported on the three lobe bearings, respectively. The measured mass flow rate is the total mass flow rate (sum of mass flow rate through all orifices). Note that the measurable flow range of the flow meters (0-100 stL/min for the left bearing and 0-50 stL/min for the right bearing) limits the number of data points in some cases. The flowmeter saturation levels (for the total mass flow rate) are given in Table D1. The uncertainty of the meters is 1.5% of full scale and (0.16E-6 kg/s for the 0-100 stL/min meter and +/-8.1E-6 kg/s for the 0-50 stL/min meter).

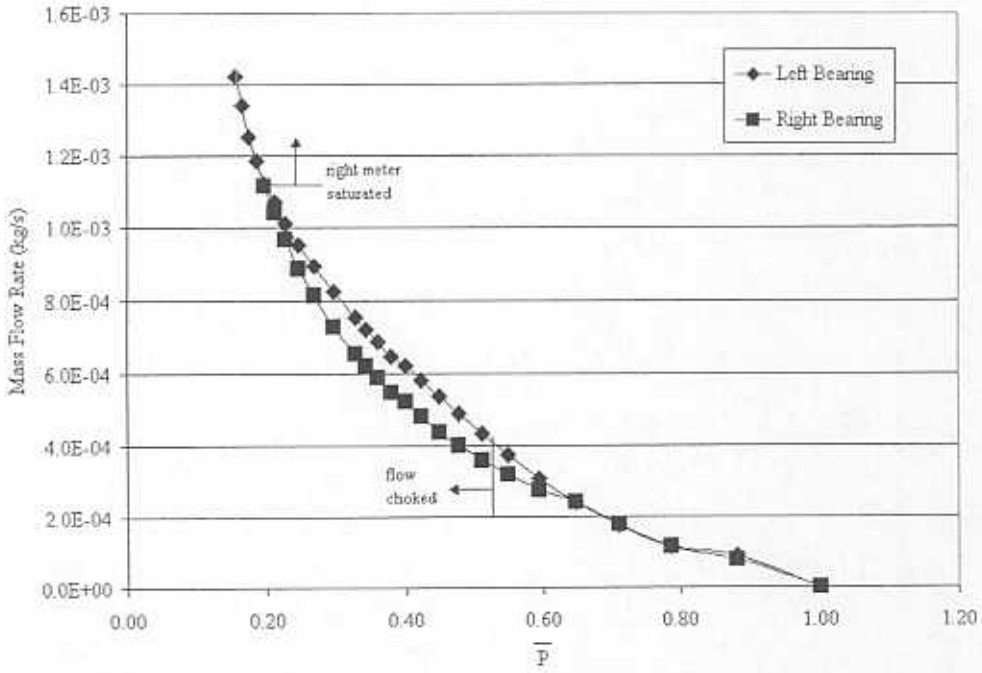

Fig. D1 Measured mass flow rate for three lobe bearing with rotor in place

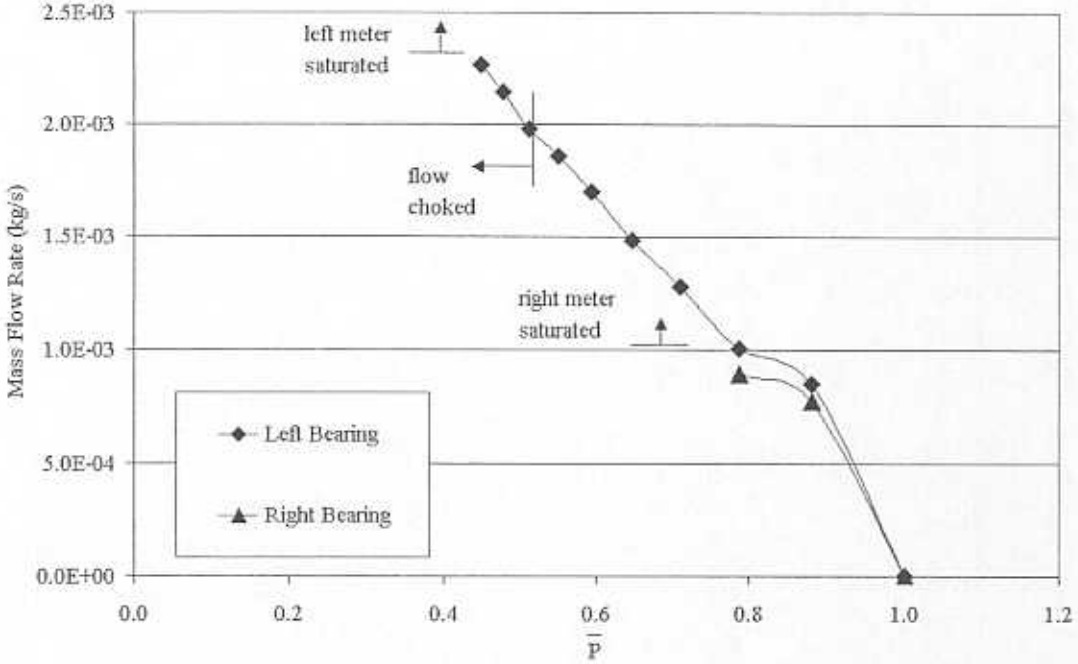

Fig. D2 Measure mass flow rate for three lobe bearing without rotor in place

Table D1 Saturation levels of mass flowmeters for three lobe bearings

Bearing Type	*Saturation Level at Left (kg/s)*	*Saturation Level at Right (kg/s)*
Three lobe, with rotor in place	0.0024	0.0011
Three lobe, without rotor in place	Meter does not saturate	0.0011

Making the empirical adjustment to determine the actual source supply pressure accounting for the flow resistance through the feed orifice for analysis of the gas bearing film consists of the follow steps (Table D2 gives several examples):

1. Choose desired test supply pressure.
2. Determine the mass flow rate for this supply pressure using the curve fitting the mass flow rate measurements in Fig. D1.

3. Take this mass flow rate to Fig. D2 and find the corresponding pressure ratio, i.e. adjusted supply pressure at the entrance to the feed orifice.

Table D2 Empirical adjustment to source supply pressure for analysis of gas bearing film

Desired Test Supply Pressure (MPa)	$\overline{P}$ with motor installed (curve fit from Fig. D1)	Mass Flow Rate with Rotor Installed (kg/s)	$\overline{P}$ without rotor installed (curve fit from Fig. D2)	Adjusted Feed Orifice Supply Pressure (MPa)
0.136	0.75	-6.24E-4	0.97	0.132
0.170	0.60	-2.98E-4	1.01	0.172
0.239	0.42	4.31E-5	1.00	0.239
0.308	0.33	2.80E-4	0.97	0.300
0.377	0.27	4.78E-4	0.94	0.353
0.446	0.23	6.48E-4	0.90	0.402
0.515	0.20	8.04E-4	0.86	0.445

APPENDIX E: CRITICAL SPEED RESPONSE INVERSION OF ROTOR SUPPORTED ON THREE LOBE BEARINGS

The remnant imbalance rotor response at the left vertical sensor with pressure ratios equal to 5.08 and 3.72, and the responses to calibrated imbalance masses at the left horizontal sensor are not included in Table 6 showing the damping ratios. For these test conditions, an inversion of the rotor response occurs at the critical speed, therefore making the determination of the damping ratio exceedingly difficult. As an example of this behavior, Fig. E1 displays the remnant imbalance response at the left vertical sensor for three supply pressure ratios where the response with pressure ratio equal to 2.36 does not show the critical speed response inversion.

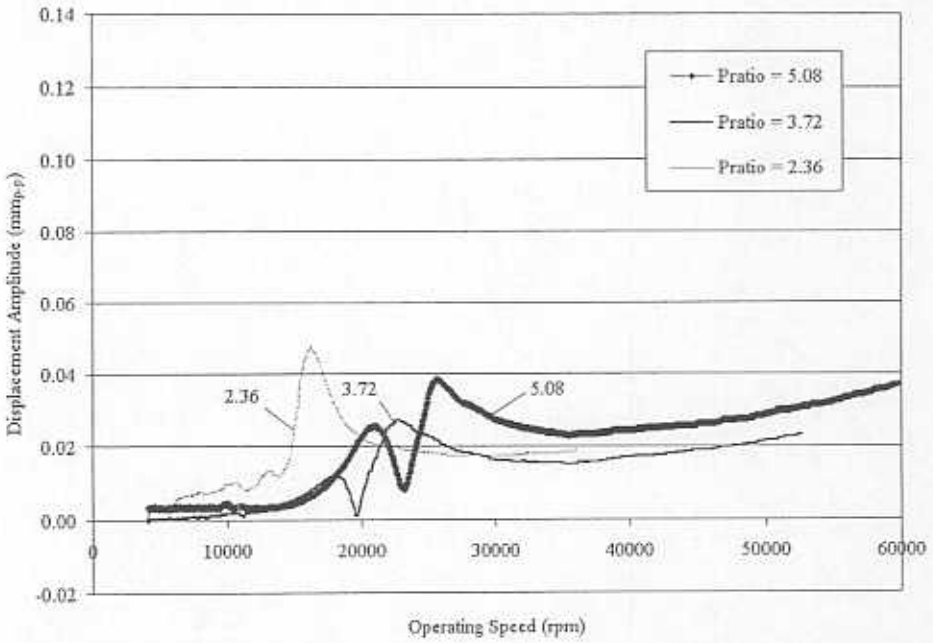

Fig. E1 Coastdown response at the left horizontal eddy current sensor to remnant imbalance of rotor supported on three lobe bearings

This behavior (an inversion of the response peak at the critical speed) may be explained by several possible reasons. If the response does not indicate a constant vector at low speeds (where the slow roll vector is normally identified) the slow roll

vector can not be correctly identified and should not be subtracted from the rest of the vector samples. If incorrectly identified, the slow roll vector greatly affects the overall response when subtracted from the rest of the vector samples. The rotor model and predicted damped eigenanalysis (as explained in the "Predicted System Performance" section) indicate that the cylindrical and conical modes are excited at nearly the same speeds. The synchronous response could be a combination of the two modes, thereby exhibiting an inversion at the critical speed.

APPENDIX F: BANDWIDTH AND Q FACTOR DAMPING RATIOS FOR ROTOR SUPPORTED ON THREE TYPES OF BEARINGS

The amplitudes of displacement and identified speeds used in the calculation of damping ratios for the rotor supported on three lobe bearings are given in Table F1.

Amplitudes, and therefore damping ratios, from the response of the rotor supported on pressure dam bearings are not included, or calculated, since the response peaks at the critical speeds are too broad for the bandwidth or Q factor methods. This is an indication that the pressure dam bearings offer higher damping ratios than either the three lobe bearings or the HyPad® tilting pad bearings.

Table F1 Amplitudes of displacements and identified speeds for damping ratio calculations using the bandwidth and Q factor methods with rotor supported on three lobe bearings

Sensor	*Imbalance Condition*	*Supply Pressure Ratio*	*Maximum Displacement* (mm_{p-p})	*0.707 times Maximum Displacement* (mm_{p-p})	*Natural Frequency,* N_n, *(rpm)*	N_1 *(rpm)*	N_2 *(rpm)*
RV	Remnant	5.08	0.090	0.064	23,500	21,340	25,790
		3.72	0.085	0.060	20,900	19,100	23,000
		2.36	0.062	0.044	15,700	13,950	17,900
	U1	5.08	0.116	0.082	22,790	21,240	24,740
	U2	5.08	0.068	0.048	22,240	20,940	23,440
RH	Remnant	5.08	0.062	0.044	24,950	22,550	26,200
		3.72	0.064	0.045	20,400	19,350	23,340
		2.36	0.087	0.062	15,350	14,375	17,090
	U1	5.08	0.077	0.055	22,540	21,390	25,040
	U2	5.08	0.033	0.024	22,390	20,740	23,390
LV	Remnant	5.08	0.042	0.030	25,490	23,390	27,290
		3.72	0.041	0.029	21,500	20,400	23,500
		2.36	0.030	0.021	16,340	15,590	19,550
	U1	5.08	-	-	-	-	-
	U2	5.08	-	-	-	-	-
LH	Remnant	5.08	-	-	-	-	-
		3.72	-	-	-	-	-
		2.36	0.047	0.033	16,100	15,325	17,790
	U1	5.08	0.081	0.057	22,490	20,140	26,925
	U2	5.08	0.069	0.048	22,050	19,200	28,300

The amplitudes of displacement and identified speeds used in the calculation of damping ratios for the rotor supported on HyPad® tilting pad bearings are given in Table F2.

Table F2 Amplitudes of displacements and identified speeds (at the right vertical eddy current sensor) for damping ratio calculations using the bandwidth and Q factor methods with rotor supported on HyPad® tilting pad bearings for three clearances

Radial Clearance Condition	*Supply Pressure Ratio*	*Maximum Displacement* (mm_{p-p})	*0.707 times Maximum Displacement* (mm_{p-p})	*Natural Frequency,* N_n, *(rpm)*	N_1 *(rpm)*	N_2 *(rpm)*
0.10 mm	5.08	0.023	0.016	13,500	13,000	14,250
	3.72	0.025	0.018	12,000	11,000	12,500
	3.04	0.022	0.016	9990	9490	10,490
0.05 mm	5.08	0.035	0.024	20,680	19,460	24,150
	3.72	0.030	0.021	17,470	16,750	21,060
	2.36	0.015	0.011	17,920	16,770	19,710
0.02 mm	5.08	0.042	0.030	17,270	16,400	18,240
	4.40	0.048	0.034	16,790	16,070	17,740
	3.72	0.042	0.030	15,170	14,860	16,260

APPENDIX G: THRESHOLD AND WHIRL FREQUENCIES FOR ROTOR SUPPORTED ON THREE LOBE BEARINGS

The threshold and whirl frequencies reported in Fig. 20 and Fig. 21 are detailed in Table G1.

Table G1 Measured threshold frequencies, whirl frequencies, and whirl frequency ratios on run up of rotor supported on three lobe bearings (remnant imbalance)

Supply Pressure Ratio	*Threshold Frequency (Hz)*	*Whirl Frequency (Hz)*	*Natural Frequency (Hz)*	*Whirl Frequency Ratio (WFR)*
1.82	300	148	-	0.49
2.02	564	232	-	0.41
2.36	620	228	261	0.40
2.36	567	236	-	0.38
2.70	656	268	-	0.41
3.04	752	292	-	0.39
3.18	849	290	-	0.34
3.38	812	308	-	0.38
3.72	916	324	348	0.35
3.99	1072	330	-	0.31
4.40	1080	350	-	0.32
4.40	1173	340	-	0.29
5.08	1420	360	392	0.25

APPENDIX H: BEARING COEFFICIENTS AND ROTOR MODEL PROPERTIES

Table H1 lists the predicted direct and cross-coupled bearing force coefficients at pressure ratio 5.08 for three operating speeds. These coefficients are analytically linked to the rotor model described in Table H2. Rotor model material properties are given in Table H3.

Table H1 Bearing force coefficients calculated with finite element model. Supply pressure ratios are adjusted in the model to account for flow resistance through the orifices.

Pressure Ratio 5.08 at Rotor Speed 20000 rpm								
Freq Ratio	Kxx (N/m)	Kxy (N/m)	Kyx (N/m)	Kyy (N/m)	Cxx (Ns/m)	Cxy (Ns/m)	Cyx (Ns/m)	Cyy (Ns/m)
0.20	1.72E+06	8.97E+04	-1.03E+05	1.80E+06	94.4	-7.1	7.8	89.0
0.35	1.72E+06	8.95E+04	-1.02E+05	1.81E+06	89.5	-6.4	6.7	83.1
0.40	1.72E+06	8.94E+04	-1.02E+05	1.81E+06	89.7	-6.4	6.8	83.2
0.50	1.72E+06	8.92E+04	-1.02E+05	1.81E+06	89.6	-6.4	6.8	83.1
0.80	1.73E+06	8.87E+04	-1.01E+05	1.81E+06	91.1	-6.5	7.0	84.1
1.00	1.73E+06	8.81E+04	-1.01E+05	1.82E+06	91.9	-6.6	7.2	85.7
1.50	1.75E+06	8.59E+04	-9.82E+04	1.84E+06	92.2	-6.7	7.3	86.6
2.00	1.78E+06	8.30E+04	-9.50E+04	1.86E+06	91.4	-6.6	7.3	86.0
5.00	1.79E+06	5.49E+04	-6.46E+04	1.83E+06	85.9	-5.7	6.4	81.5
10.0	2.06E+06	5.45E+04	-6.36E+04	2.12E+06	80.9	-5.2	5.8	76.7
100	4.21E+06	-2.73E+03	7.60E+02	4.19E+06	2.0	0.0	0.0	2.0
Pressure Ratio 5.08 at Rotor Speed 40000 rpm								
Freq Ratio	Kxx (N/m)	Kxy (N/m)	Kyx (N/m)	Kyy (N/m)	Cxx (Ns/m)	Cxy (Ns/m)	Cyx (Ns/m)	Cyy (Ns/m)
0.20	1.74E+06	1.78E+05	-2.03E+05	1.82E+06	92.7	-14.0	15.4	87.6
0.35	1.74E+06	1.77E+05	-2.02E+05	1.82E+06	88.9	-12.8	13.7	83.5
0.40	1.74E+06	1.77E+05	-2.01E+05	1.83E+06	89.3	-12.7	14.0	82.5
0.50	1.75E+06	1.75E+05	-2.00E+05	1.83E+06	90.4	-13.0	14.3	84.4
0.80	1.77E+06	1.70E+05	-1.94E+05	1.85E+06	90.6	-13.2	14.5	85.3
1.00	1.79E+06	1.65E+05	-1.89E+05	1.87E+06	89.9	-13.1	14.4	84.8
1.50	1.87E+06	1.50E+05	-1.72E+05	1.94E+06	87.4	-12.4	13.6	82.6
2.00	1.96E+06	1.31E+05	-1.51E+05	2.02E+06	83.9	-11.4	12.5	79.5
5.00	2.67E+06	2.21E+04	-3.05E+04	2.70E+06	56.6	-5.0	5.5	54.0
10.0	3.46E+06	-2.39E+04	1.97E+04	3.46E+06	26.7	-1.1	1.2	25.8
100	4.30E+06	-3.53E+03	-5.73E+02	4.29E+06	0.6	0.0	0.0	0.6
Pressure Ratio 5.08 at Rotor Speed 100000 rpm								
Freq Ratio	Kxx (N/m)	Kxy (N/m)	Kyx (N/m)	Kyy (N/m)	Cxx (Ns/m)	Cxy (Ns/m)	Cyx (Ns/m)	Cyy (Ns/m)
0.20	1.85E+06	4.25E+05	-4.78E+05	1.91E+06	81.8	-32.3	35.0	78.7
0.35	1.88E+06	4.09E+05	-4.61E+05	1.93E+06	80.7	-30.9	33.4	77.4
0.40	1.89E+06	4.02E+05	-4.53E+05	1.94E+06	80.3	-30.6	33.1	77.0
0.50	1.91E+06	3.86E+05	-4.36E+05	1.97E+06	79.5	-30.0	32.4	76.4
0.80	2.02E+06	3.24E+05	-3.69E+05	2.07E+06	76.1	-27.1	29.3	73.2
1.00	2.11E+06	2.76E+05	-3.16E+05	2.16E+06	73.1	-24.6	26.7	70.3
1.50	2.38E+06	1.53E+05	-1.84E+05	2.42E+06	64.1	-18.3	19.8	61.8
2.00	2.66E+06	5.94E+04	-8.28E+04	2.69E+06	54.4	-12.6	13.8	52.5
5.00	3.65E+06	-5.54E+04	4.58E+04	3.64E+06	19.2	-1.4	1.6	18.7
10.0	4.03E+06	-2.83E+04	1.83E+04	4.02E+06	6.3	-0.1	0.2	6.2
100	4.37E+06	-6.88E+03	-3.12E+03	4.36E+06	0.1	0.0	0.0	0.1

Table H2 Rotor Model Physical Properties

Rotor Model: Multiple Shafts, Elements, Sub-Elements and Layers.									
Shaft	Element	Sub-Element	Layer	Length	Left		Right		Material
					OD	ID	OD	ID	
#	#	#	#	(m)	(m)	(m)	(m)	(m)	#
1	1	1	1	0.0080	0.015	0.000	0.015	0.000	1
1	1	1	2	0.0080	0.029	0.015	0.029	0.015	2
1	2	1	1	0.0120	0.015	0.000	0.015	0.000	1
1	2	1	2	0.0120	0.019	0.015	0.019	0.015	2
1	3	1	1	0.0141	0.015	0.000	0.015	0.000	1
1	3	1	2	0.0141	0.029	0.015	0.029	0.015	2
1	4	1	1	0.0141	0.015	0.000	0.015	0.000	1
1	4	1	2	0.0141	0.029	0.015	0.029	0.015	2
1	5	1	1	0.0141	0.015	0.000	0.015	0.000	1
1	5	1	2	0.0141	0.029	0.015	0.029	0.015	2
1	6	1	1	0.0141	0.015	0.000	0.015	0.000	1
1	6	1	2	0.0141	0.029	0.015	0.029	0.015	2
1	7	1	1	0.0006	0.015	0.000	0.015	0.000	1
1	8	1	1	0.0090	0.015	0.000	0.015	0.000	1
1	8	1	2	0.0090	0.029	0.016	0.029	0.016	3
1	9	1	1	0.0090	0.015	0.000	0.015	0.000	1
1	9	1	2	0.0090	0.029	0.015	0.029	0.015	4
1	10	1	1	0.0090	0.015	0.000	0.015	0.000	1
1	10	1	2	0.0090	0.029	0.015	0.029	0.015	4
1	11	1	1	0.0090	0.015	0.000	0.015	0.000	1
1	11	1	2	0.0090	0.029	0.016	0.029	0.016	3
1	12	1	1	0.0006	0.015	0.000	0.015	0.000	1
1	13	1	1	0.0141	0.015	0.000	0.015	0.000	1
1	13	1	2	0.0141	0.029	0.015	0.029	0.015	2
1	14	1	1	0.0141	0.015	0.000	0.015	0.000	1
1	14	1	2	0.0141	0.029	0.015	0.029	0.015	2
1	15	1	1	0.0141	0.015	0.000	0.015	0.000	1
1	15	1	2	0.0141	0.029	0.015	0.029	0.015	2
1	16	1	1	0.0141	0.015	0.000	0.015	0.000	1
1	16	1	2	0.0141	0.029	0.015	0.029	0.015	2
1	17	1	1	0.0120	0.015	0.000	0.015	0.000	1
1	17	1	2	0.0120	0.019	0.015	0.019	0.015	2
1	18	1	1	0.0080	0.015	0.000	0.015	0.000	1
1	18	1	2	0.0080	0.029	0.015	0.029	0.015	2

Table H3 Rotor Model Material Properties

Material Properties			
Material	Density ρ	Elastic Modulus E	Shear Modulus G
#	(kg/m^3)	(N/m^2)	(N/m^2)
1	7833	206.8E+9	82.7E+9
2	7833	62.1E+9	24.8E+9
3	3200	10.3E+9	4.0E+9
4	3200	31.0E+9	12.4E+9

APPENDIX I: TRANSIENT RESPONSE OF COATED ROTOR SUPPORTED ON THREE LOBE BEARINGS

Fig. I2 shows the transient displacement and transmitted load response of the coated rotor supported on three lobe bearings. Note that the rotor lift off occurs sooner (in time) than with the uncoated rotor.

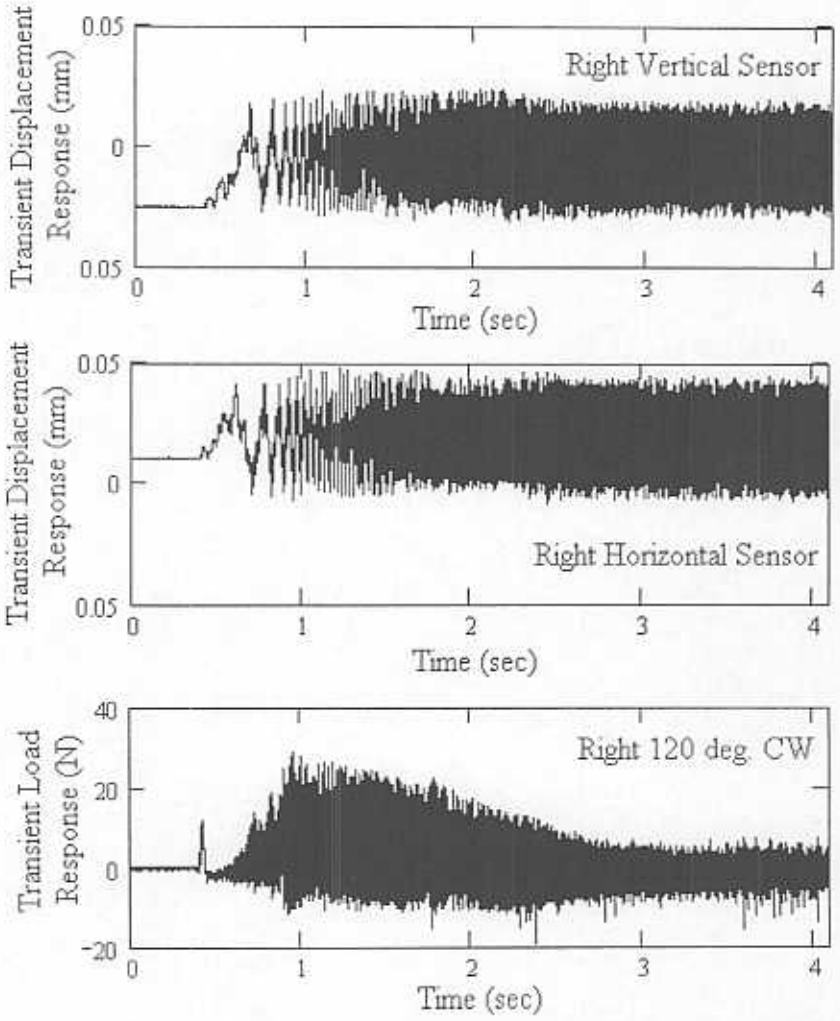

Fig. I1 Transient displacement and load response of coated rotor supported on three lobe bearings at pressure ratio equal to 5.08

Fig. I2 displays the corresponding waterfall contour plot, indicating the rotor/bearing natural frequency at lift-off. Assuming the same amplitude threshold (assigning bright green colors to high levels of displacement amplitude), vibration levels are consistently lower with the coated rotor than with the uncoated rotor.

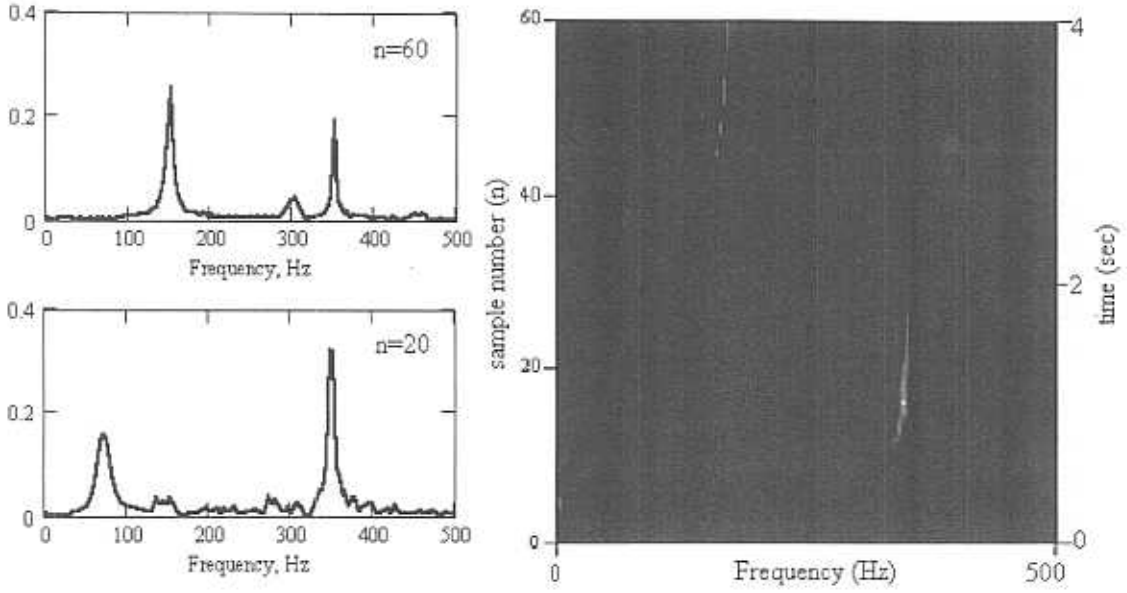

Fig. I2 Contour plot of transient waterfall displacement response for coated rotor supported on three lobe bearing at pressure ratio equal to 3.72. Spectral lines are given for sample 20 (1.5 seconds) and 60 (.04 seconds). At sample 60: 1X = 172 Hz (10,320 rpm).